To the Graduate Council:

I am submitting herewith a thesis written by Edward Gordon Schaub entitled "Critical Assessments of Finite Element CFD Methodology for 2-D Room Air Motion Simulation". I have examined the final copy of this thesis for form and content and recommend that it be accepted in partial fulfillment of the requirements for the degree of Master of Science, with a major in Engineering Science.

A. J. Baker, Major Professor

We have read this thesis and recommend its acceptance:

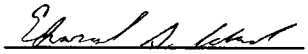
Accepted for the Council:

Associate Vice Chancellor
and Dean of The Graduate School

STATEMENT OF PERMISSION TO USE

In presenting this thesis in partial fulfillment of the requirements for a Master's degree at The University of Tennesse, Knoxville, I agree that the Library shall make it available to borrowers under rules of the Library. Brief quotations from this thesis are allowable without special permission, provided that accurate acknowledgment of the source is made.

Permission for extensive quotation from or reproduction of this thesis may be granted by my major professor, or in his absence, by the Head of Interlibrary Services when, in the opinion of either, the proposed use of the material is for scholarly purposes. Any copying or use of the material in this thesis for financial gain shall not be allowed without my written permission.



Signature

3/30/93

Date

Critical Assessments of Finite Element CFD Methodology for 2-D Room Air Motion Simulation

A Thesis

Presented for the

Master of Science

Degree

The University of Tennessee, Knoxville

Edward Gordon Schaub

May, 1993

DEDICATION

This work done in this thesis is dedicated to my grandfather, Gordon Edward Turpen, a true cowboy.
Who set an example I have tried to follow.

ACKNOWLEDGMENTS

My appreciation goes to the many individuals who made the work on this thesis project possible and rewarding. First, I would like to thank my major professor, Dr. A. J. Baker, for his guidance and remarkable insight to the problems encountered in the work. I would also like to thank the other members of my committee, Dr. G.S. Iannelli and Prof. Dick Kelso, who provided me with help and support in some of the difficulties encountered. I would also like to thank Winston Holmes and Faye Muly in the computer center for their help in setting up the programs to present the figures in this thesis. Particular appreciation goes to the individuals at the National Science Foundation who provided the grant to make this work possible. Thanks to the people at COMCO for answering my questions about the modeling platform used to perform the simulations.

Finally and especially, I would like to thank my parents, Edward Charles Schaub and Mary Margaret Schaub, for their support and care. They have made everything possible for their only child.

ABSTRACT

The work in this thesis is the benchmarking and validation of the continuity constraint algorithm for the solution approximation to the Navier-Stokes (NS) equation system for thermal-incompressible fluid flow. The benchmark cases are used to compare the continuity constraint solution to accepted accurate solutions. The two benchmark cases are the two-dimensional, isothermal step-wall diffuser and thermal cavity problems. The continuity constraint algorithm is then validated with comparison to experimental data obtained for a full-scale, two-dimensional test room for an isothermal case and a non-isothermal case with a heated floor.

The finite element spatial discretization utilizes the bilinear basis for all variables, and time integration is performed with a θ-implicit ordinary differential equation approximation algorithm. The continuity constraint solution approximation of velocity is used for the vorticity and streamfunction solutions in a post-processing operation. The results are presented in the form of velocity vector and isocline plots for the interpretation of the results.

the benchmark problem showed exceptional agreement for the continuity constraint solution with the accepted solutions as long as the flow remained two-dimensional. In the step-wall diffuser simulations at Reynolds numbers involving three-dimensional flow, the absence of cross-flow effects made comparison with the experimental results unsuitable. For the room air motion simulations, the results for the isothermal and non-isothermal case showed the solution to be unsteady with the appearance of oscillations in the supply jet and the absence of a stationary flow field. The transient nature of the flow made direct comparison with the experimental results inconclusive, since the experimental data was presented in a stationary format.

Table of Contents

I. Introduction 1
II. The Governing Equations 4
Navier-Stokes equation system for incompressible thermal flow 4
Boundary Conditions 6
Initial conditions 8
III. The Continuity Constraint and Pressure 10
Pressure determination 10
Vector field theory: vorticity-streamfunction formulation 11
Pressure relaxation: PPE algorithm 14
IV. Finite Element Weak Statement Algorithm 17
Conservation law form 17
Taylor modified conservation law statement 17
The weak statement 18
Spatial semi-discretization 20
Time integration algorithm 23
V. Discussion and Results 25
Thermal cavity 25
Isothermal step-wall diffuser 58
ASME WAM Session Heat Transfer Benchmark Problem 68
Room air motion simulations 76
Isothermal Case 84
Non-isothermal case 100
VI. Conclusions and Recommendations 113
References 116
Appendices 119
Appendix I. Finite Element Matrix Form of the Weak Statement 120
Appendix II. Evaluation of Newton Jacobian Matrices 124
Appendix III. Time Integration Proceduare 128
VITA 131

List of Figures

1. Vorticity Kinematic Constraint Geometry at a Wall 13
2. Thermal Cavity Boundary Conditions 26
3. de Vahl Davis: Streamfunction Contours 29
4. de Vahl Davis: Temperature Contours 29
5. de Vahl Davis: U Velocity Contours 30
6. de Vahl Davis: V Velocity Contours 30
7. de Vahl Davis: Vorticity Contours 31
8. 11X11 Uniform Mesh: Streamfunction Contours 32
   A). Continuity Constraint 32
   B). Voriticity-Streamfunction 32
9. 11X11 Uniform Mesh: Temperature Contours 33
   A). Continuity Constraint 33
   B). Voriticity-Streamfunction 33
10. 11X11 Uniform Mesh: U Velocity Contours 34
   A). Continuity Constraint 34
   B). Voriticity-Streamfunction 34
11. 11X11 Uniform Mesh: V Velocity Contours 35
   A). Continuity Constraint 35
   B). Voriticity-Streamfunction 35
12. 11X11 Uniform Mesh: Vorticity Contours 36
   A). Continuity Constraint 36
   B). Voriticity-Streamfunction 36
13. 11X11 Uniform Mesh: Velocity Vectors 37
   A). Continuity Constraint 37
   B). Voriticity-Streamfunction 37
14. Uniformly Refined Mesh: Streamfunction Contours 38
   A). Continuity Constraint 38
   B). Voriticity-Streamfunction 38
15. Uniformly Refined Mesh: Temperature Contours 39
   A). Continuity Constraint 39
   B). Voriticity-Streamfunction 39
16. Uniformly Refined Mesh: U Velocity Contours 40
   A). Continuity Constraint 40
   B). Voriticity-Streamfunction 40
17. Uniformly Refined Mesh: V Velocity Contours 41
   A). Continuity Constraint 41
   B). Voriticity-Streamfunction 41
18. Uniformly Refined Mesh: Vorticity Contours 42
   A). Continuity Constraint 42
   B). Voriticity-Streamfunction 42
19. Uniformly Refined Mesh: Velocity Vectors 43
   A). Continuity Constraint 43
   B). Voriticity-Streamfunction 43
20. Locally Refined Mesh: 11X11 45
21. Locally Refined Mesh: Streamfunction Contours 46
   A). Continuity Constraint 46
   B). Voriticity-Streamfunction 46
22. Locally Refined Mesh: Temperature Contours 47
   A). Continuity Constraint 47

B). Voriticity-Streamfunction 47
23. Locally Refined Mesh: U Velocity Contours 48
A). Continuity Constraint 48
B). Voriticity-Streamfunction 48
24. Locally Refined Mesh: V Velocity Contours 49
A). Continuity Constraint 49
B). Voriticity-Streamfunction 49
25. Locally Refined Mesh: Vorticity Contours 50
A). Continuity Constraint 50
B). Voriticity-Streamfunction 50
26. Locally Refined Mesh: Velocity Vectors 51
A). Continuity Constraint 51
B). Voriticity-Streamfunction 51
27. Artificial Viscosity: Streamfunction Contours 52
A). Continuity Constraint 52
B). Voriticity-Streamfunction 52
28. Artificial Viscosity: Temperature Contours 53
A). Continuity Constraint 53
B). Voriticity-Streamfunction 53
29. Artificial Viscosity: U Velocity Contours 54
A). Continuity Constraint 54
B). Voriticity-Streamfunction 54
30. Artificial Viscosity: V Velocity Contours 55
A). Continuity Constraint 55
B). Voriticity-Streamfunction 55
31. Artificial Viscosity: Vorticity Contours 56
A). Continuity Constraint 56
B). Voriticity-Streamfunction 56
32. Artificial Viscosity: Velocity Vectors 57
A). Continuity Constraint 57
B). Voriticity-Streamfunction 57
33. Boundary Conditions for Step-Wall Diffuser Problem 59
34. Finite Element Mesh for Step-wall Diffuser 60
35. Armaly: Predicted Locations of Detachment and Reattachment Points 62
36. Pressure Contours: Re = 400 63
A). No Artificial Viscosity 63
B). q = 0.05 63
37. Velocity Vectors: Re = 400 64
A). No Artificial Viscosity 64
B). q = 0.05 64
38. Velocity Vectors: Re = 600 65
A). q = 0.05 65
B). q = 0.1 65
C). q = 0.15 65
39. Velocity Vectors: Re = 800 67
40. Boundary Conditions for Step-Wall Diffuser Heat Transfer Problem 69
41. Finite Element Mesh: Gartling's Geometry 71
42. Velocity Vectors: Heat Transfer Benchmark Problem 72
43. Temperature Contours: Homogenous Neumann Outflow 73
44. Temperature Profile Along Duct Walls 74
45. Nusselt Number Along Duct Walls 75
46. Geometry and Probe Locations of Test Room from Zhang 77
47. Turbulent Kinetic Energy: Isothermal Case 78

48. Turbulent Kinetic Energy: Non-isothermal Case 79
49. Finite Element Mesh for Test Room Simulations 80
50. Flow Pattern of Test Room From Zhang: Isothermal Case 82
51. Velocity Vector Field Obtained With Pilot Code CFDL.2DPHI 83
A). Exhaust Duct Length = 1/2 ft. 83
B). Exhaust Duct Length = 1 ft. 83
52. Supply Diffuser Velocity Characteristics 85
53. Initial Conditions for Isothermal Case 86
A). Velocity Vector Field 86
B). Temperature Contours 86
54. Velocity Vector Plot: Isothermal Case 88
A). No Damping in Exhaust Duct 88
B). Damping in Exhaust Duct 88
55. Isothermal Case (time = 1.4 sec.) 89
A). Velocity Vectors 89
B). Streamfunction Contours 89
56. Isothermal Case (time = 5.1 sec.) 90
A). Velocity Vectors 90
B). Streamfunction Contours 90
57. Isothermal Case (time = 10.9 sec.) 91
A). Velocity Vectors 91
B). Streamfunction Contours 91
58. Isothermal Case (time = 16.9 sec.) 92
A). Velocity Vectors 92
B). Streamfunction Contours 92
59. Isothermal Case (time = 20.8 sec.) 93
A). Velocity Vectors 93
B). Streamfunction Contours 93
60. Isothermal Case (time = 26.7 sec.) 94
A). Velocity Vectors 94
B). Streamfunction Contours 94
61. Isothermal Case (time = 30.6 sec.) 95
A). Velocity Vectors 95
B). Streamfunction Contours 95
62. Isothermal Case (time = 35.5 sec.) 96
A). Velocity Vectors 96
B). Streamfunction Contours 96
63. Isothermal Case (time = 40.4 sec.) 97
A). Velocity Vectors 97
B). Streamfunction Contours 97
64. Isothermal Case (time = 46.6 sec.) 98
A). Velocity Vectors 98
B). Streamfunction Contours 98
65. Isothermal Case (time = 50.0 sec.) 99
A). Velocity Vectors 99
B). Streamfunction Contours 99
66. Velocity Magnitudes 101
A). Experimental Data 101
B). Continuity Constraint 101
67. Final Pressure Map 102
A). Room 102
B). Close-up of Supply Diffuser 102
68. Non-isothermal Case (Initial Conditions) 104

A). Velocity Vector/Streamfunction 104
B). Temperature Contours 104
69. Non-isothermal Case (time=5.5 seconds) 105
A). Velocity Vector/Streamfunction 105
B). Temperature Contours 105
70. Non-isothermal Case (time=7.9 seconds) 106
A). Velocity Vector/Streamfunction 106
B). Temperature Contours 106
71. Non-isothermal Case (time=11.8 seconds) 107
A). Velocity Vector/Streamfunction 107
B). Temperature Contours 107
72. Non-isothermal Case (time=17.9 seconds) 108
A). Velocity Vector/Streamfunction 108
B). Temperature Contours 108
73. Non-isothermal Case (time=23.9 seconds) 109
A). Velocity Vector/Streamfunction 109
B). Temperature Contours 109
74. Non-isothermal Case (time=27.1 seconds) 110
A). Velocity Vector/Streamfunction 110
B). Temperature Contours 110
75. Non-isothermal Case (time=31.6 seconds) 111
A). Velocity Vector/Streamfunction 111
B). Temperature Contours 111
76. Flow Pattern Comparison 112
A). Interpolated Flow Field from Smoke Releases (Zhang) 112
B). Simulation Results 112

List of Nomenclature

Abbreviations:

CFD	.....	Computational Fluid Dynamics
NS	.....	Navier-Stokes
OBC	.....	Outflow Boundary Conditions
PPE	.....	Pressure Poisson Equation
WS	.....	Weak Statement
TWS	.....	Taylor Weak Statement
Re	.....	Reynolds number
Re^f	.....	effective Reynolds number
Re^t	.....	turbulent Reynolds number
Pr	.....	Prandtl number
Pr^t	.....	turbulent Prandtl number
Gr	.....	Grashof number
Pe	.....	Peclet number
Pe^f	.....	effective Peclet number
Ar	.....	Archimedes number

Symbols:

u_i	.....	velocity vector
P	.....	kinematic pressure
U	.....	reference velocity
T_{max}	.....	maximum expected temperature
T_{ref}	.....	reference temperature
ΔT_{ref}	.....	temperature range
s_Θ	.....	source of thermal energy
g	.....	gravitational constant

L	.....	reference length
n	.....	normal coordinate
τ	.....	tangential coordinate
Θ	.....	potential temperature
ν_r	.....	kinematic viscosity
ν^t	.....	eddy viscosity
ρ_o	.....	density
cp	.....	specific heat
β	.....	coefficient of thermal expansion
δ	.....	Kronecker delta
ω	.....	vorticity
ψ	.....	streamfunction
k	.....	thermal conductivity
Γ_i	.....	boundary segment
f_i	.....	described Dirichlet contraint
q'	.....	non-dimensional heat flux
q^o	.....	initial condition
ϕ	.....	scalar potential
x_i	.....	coordinate

Chapter I

Introduction

The range of fluid flow problem classes amenable to simulation has increased significantly in the last couple of decades due to the advent of the computer and the increased computational abilities of these machines. Before computers, and engineer/analyst was limited to paper analysis of various reduced forms of the Navier-Stokes equation system of simulating elementary flow problems such as full developed flows in ducts or boundary layer flows.

Today, the engineer is no longer limited to paper analysis. With the increasing development of speed and capabilities of computers, the engineer can conduct a wide range of simulations to fluid flow phenomena using mathematical approximations to the full Navier-Stokes equation system. The engineer has to determine the most suitable approximation method to the solution of the Navier-Stokes equation system for performing these simulations. The procedure of numerically approximating the solution to the Navier-Stokes equation system for simulation purposes is referred to as "Computational Fluid Dynamics" with the acronym CFD.

One area of CFD analysis that has gained extensive interest is the simulation of room air motion and contaminant distribution, of use in the design of heating and ventilation systems. In the design process of room ventilation systems, the comfort, air quality, and energy efficiency must be taken into consideration.

Comfort is the most critical aspect in the design of room ventilation systems. The ventilation must be arranged in such a manner that the occupied space is free of drafts and also absent from temperature gradients such as warm or cold spots throughout the room.

The problem of contaminant distribution arises mainly in work environments where there is a particular source of contaminant distribution. One work environment example is the production of micro-processor chips where it is essential that 'dirt' not pollute the chip itself. Therefore, knowledge of the air flow patterns and corresponding contaminant transport is essential for the development of ventilation systems for the work environment.

The final aspect is energy efficiency where savings in energy usage of a room can be substantial with proper ventilation design. The CFD models must be able to take into account various heat sources within the room along with radiant heat transfer from the windows including the effects of contaminant distribution on radiant heat transfer [19].

Previously, scale-model and full-scale experimental rooms had to be set up in order to determine the air flow patterns for a particular ventilation system and room geometry. The experimental room is expensive to arrange and only minor modifications could be made without major investment. In addition, the gathering of data is time consuming and also costly. With CFD capabilities, analysis of numerous variables on various geometries and ventilation arrangements can be made at relatively less cost. The question the engineer has to answer is whether the solution obtained is accurate, hence reliable, and whether the CFD method used was pertinent for analyzing the problem or is there a better method.

Three characteristics are of paramount importance in CFD algorithm methodology: 1) accuracy, 2) efficiency, and 3) computer requirements. The first of these, accuracy, is a difficult aspect to measure, since few analytical solutions exist to the Navier-Stokes equation system. The accuracy assessment of a CFD approximation algorithm is often made by verification with an analytical solution for a simple problem, benchmarking with an accepted accurate solution, and validation with experimental data for real problem classes. In addition, the algorithm must be proven accurate for a range of problems, in order to be confident in its application to realistic problems.

Computer requirement refers to the computer resources, i.e., memory and storage, an algorithm requires to perform a simulation. This is usually determined by the matrix size and structure produced by the algorithm. The smaller or more sparse the matrix formed, and required to solve, the less memory required.

The final aspect is the efficiency of the algorithm can perform the simulation. For a steady simulation, the faster an algorithm can achieve steady-state from the initial condition, the better. For transient unsteady solutions, efficiency is determined by the larger time step size the algorithm allows while satisfying a specific error tolerance.

The objective of the thesis is to answer the basic questions on accuracy with verification and benchmarking for the recently developed finite element CFD continuity constraint algorithm [13,14] for the thermal-incompressible Navier-Stokes equations. The accuracy and some aspects of efficiency will be addressed on classical two-dimensional benchmark problems and comparison to alternative mathematical forms for incompressible Navier-Stokes and experimental data. Simulations are then performed on a full-scale experimental two dimensional room setup to address validation on a realistic problem case.

CHAPTER II

The Governing Equations

Navier-Stokes equation system for incompressible thermal flow

The simulation of room air motion is performed by generating a numerical approximation to the solution of the Navier-Stokes (NS) equation system for incompressible-thermal fluid flow. The corresponding initial value partial differential equation system expressing the conservation mass, linear momentum, and energy upon a suitable non-dimensionalization is

$$L(\rho_o) = \frac{\partial u_i}{\partial x_i} = 0 \tag{1}$$

$$L(u_i) = \frac{\partial u_i}{\partial t} + \frac{\partial}{\partial x_j}\left(u_j u_i + P\delta_{ij} - \frac{1}{Re}\frac{\partial u_i}{\partial x_j} \right) - Ar\Theta\delta_{ig} = 0 \tag{2}$$

$$L(\Theta) = \frac{\partial \Theta}{\partial t} + \frac{\partial}{\partial x_j}\left(u_j\Theta - \frac{1}{Pe}\frac{\partial \Theta}{\partial x_j} \right) - s_\Theta = 0 \tag{3}$$

The variables in this system and their normalization are

u_i - velocity vector; $u = \frac{u_i^*}{U}$,

P - kinematic pressure; $P = \frac{p}{\rho_o U^2}$,

Θ - potential temperature; $\Theta = \frac{T - T_{ref}}{\Delta T_{ref}}$,

U - reference velocity,

ΔT_{ref} - expected temperature range; $\Delta T_{ref} = T_{max} - T_{ref}$,

T_{max} - maximum expected temperature,

T_{ref} - reference temperature

s_Θ - source of thermal energy

The dimensionless groups and fluid properties appearing in the equation system are the

Re - Reynolds number; $\mathrm{Re} = \dfrac{UL}{\nu_r}$,

Pr - Prandtl number, $\mathrm{Pr} = \dfrac{c_p \rho_o \nu_r}{k}$,

Gr - Grashof number; $\mathrm{Gr} = \dfrac{g\beta\Delta T_{ref} L}{\nu_r^2}$,

Pe - Peclet number, $\mathrm{Pe} = \mathrm{RePr}$,

L - reference length

ν_r - kinematic viscosity,

ρ_0 - density,

c_p - specific heat,

β - coefficient of thermal expansion,

g - gravitational constant.

For turbulent flow analysis, the Reynolds-averaged form of the conservation law statements is used with identification of a turbulence closure model [1; p. 6]. In the eddy-viscosity concept, the turbulent Reynolds stress term appearing in the momentum and the turbulent heat flux of the energy equation are replaced with an eddy-viscosity term. The Reynolds number of the momentum equation appears in the Reynolds-averaged form as

$$\frac{1}{\mathrm{Re}} \Rightarrow \frac{1}{\mathrm{Re}} + \nu^t = \frac{1}{\mathrm{Re}}\left(1 + \mathrm{Re}^t\right) \equiv \frac{1}{\mathrm{Re}^f} \tag{4}$$

where ν^t is the eddy-viscosity and Re^t (ν^t/ν) is the turbulent Reynolds number. The effective Reynolds number thereby simulates the added diffusive transport of a turbulent flow, as theorized in an eddy-viscosity closure model.

Similarly, the Peclet number appearing in the diffusive transport of thermal energy is expressed as

$$\frac{1}{Pe} \Rightarrow \frac{1}{Pe} + \frac{\nu^t}{Pr^t} \equiv \frac{1}{Pe}\left(1 + Re^t\right) \equiv \frac{1}{Pe^f} \tag{5}$$

where Pr^t, the turbulent Prandtl number is assumed identical to Pr and Pe^f is the effective(diffusive) Peclet number.

Validation of a proper turbulence model is beyond the scope of this theses topic. Therefore, for laminar flow analysis, Re^t and Pe^t are treated as constants for setting the level of effective diffusive transport. The use of Re^t and Pe^t in this manner is analogous to adjusting the laminar eddy-viscosity to set the Reynolds and Peclet numbers.

In the momentum equation, the Boussinesq body force approximation is made, where δ_{ig} is the Kronecker delta aligned with the gravity direction. As a result, thermal energy distributions act as a source of momentum. Defining the reference velocity as

$$U = \sqrt{g\beta L \Delta T_{ref}} \tag{6}$$

yields the Grashof number equal to the Reynolds number squared ($Gr=Re^2$), thus producing an Archimedes number of unity.

The NS equation system is defined on the domain Ω with the boundary closure $\partial\Omega = \Gamma_1 \oplus \Gamma_2 \oplus \ldots \Gamma_{i=N}$, where Γ_i are disjoint boundary segments for application of boundary conditions. The NS equation system forms an initial boundary value problem (IBVP) that requires the application of appropriate boundary and initial conditions for the problem statement to be properly posed.

Boundary Conditions

Since Re>0 by definition, the underlying character of the NS equation system is a second-order elliptical partial differential equation system. Therefore, the well-posedness of the system requires the application of constraint conditions all around the boundary. The second-order spatial derivatives require at least two auxiliary conditions from differential equation theory for the velocity and temperature. Valid boundary conditions for velocity are also restricted by the constraint of continuity, equation (1).

Typically, the inflow velocity and temperature are known values prescribed by

$$u_i n_i = f_u(\tau), \Theta = f_\Theta(\tau); \text{ on } \Gamma_D \tag{7}$$

where τ is a coordinate tangent to the boundary segment Γ_D, which denotes a boundary with prescribed Dirichlet data. If either the velocity or temperature at the inflow boundary is not known, a vanishing Neumann condition for these variables is assumed valid.

At impenetrable walls, the simplest condition for velocity is a no slip boundary condition, where both the normal and tangential components of velocity are zero. Another valid boundary condition is a slip wall, or traction boundary, where the tangential component of velocity is not zero but constrained by

$$\frac{\partial u_\tau}{\partial n} = -\tau_{wall}, u_n = 0; \text{ on } \Gamma_N \tag{8}$$

Here, n denotes the direction normal to the boundary, u_τ the tangential component of velocity, and τ_{wall} is the drag at the wall. The expression Γ_N identifies a prescribed Neumann boundary. A fully slip wall condition corresponds to τ_{wall} set equal to zero. Since the wall is impenetrable, the normal component of velocity is always zero.

A range of boundary conditions at the walls are valid for temperature. A known temperature is the prescribed Dirichlet data as expressed in the inflow boundary condition of equation (7). Alternatively, a heat flux specification at the wall is of the form

$$-\frac{\partial \Theta}{\partial n} = q'; \text{ on } \Gamma_N \tag{9}$$

where q' is the prescribed non-dimensional heat flux. In the absence of the constraints, the homogeneous Neumann condition corresponding to an adiabatic wall is used.

Outflow boundaries occur since the domain is truncated for computational purposes. The proper outflow boundary condition (OBC) varies for different problems specifications. The most convenient form of an outflow boundary for fully developed flow is a vanishing Neumann condition on the velocities and temperature, i.e.,

$$\frac{\partial u_\tau}{\partial n} = \frac{\partial u_n}{\partial n} = 0; \frac{\partial \Theta}{\partial n} = 0: \text{on } \Gamma_O \tag{10}$$

where u_n is the velocity component perpendicular to the boundary. Equation (10) is not valid when the flow is undeveloped at the outflow boundary. In this case, a traction boundary condition can be applied at the boundary which consists of a normal and tangential component

$$-P + \frac{2}{Re}\frac{\partial u_\tau}{\partial n} = F_n$$
$$\frac{1}{Re}\left(\frac{\partial u_\tau}{\partial n} + \frac{\partial u_n}{\partial n}\right) = F_\tau \qquad (11)$$

where F_n is the normal traction and F_τ is the tangential traction. Rarely, though, are these tractions known, hence proper use of equation (11) has come under much discussion [2].

The remaining boundary condition is a symmetry plane, to mirror image along a plane in Ω to reduce the size of the problem domain. Symmetry plane boundary conditions are identical to a fully slip wall boundary condition where the normal component of velocity is zero and the tangential component, along with temperature, have a homogeneous Neumann condition.

Initial Conditions

The single requirement for a properly posed initial condition on momentum is that it satisfy the continuity constraint. The rate of obtaining a steady-state solution (converged solution) of a time integration algorithm, in part, depends on the specified initial conditions, hence it is best to avoid "cold starts" where the initial velocity field is assumed zero throughout Ω.

One initial condition that is easy to form and satisfies continuity is an irrotational flow field

$$\varepsilon_{kij}\frac{\partial u_i^o}{\partial x_j} \equiv 0 \qquad (12)$$

where superscript o denotes the initial velocity field. Therefore, since the velocity field is irrotational it can be expressed as the gradient of a scalar potential

$$u_i^o = \frac{\partial \phi}{\partial x_i} \qquad (13)$$

Placing this expression into the continuity equation produces the Laplacian for the potential

$$-\frac{\partial^2 \phi}{\partial x_i \partial x_i} = 0 \qquad (14)$$

Neumann boundary conditions are obtained from the normal projection of equation (13) onto a boundary

$$\frac{\partial \phi}{\partial x_i} n_i = u_n \tag{15}$$

resulting in a prescribe Neumann condition at inflow boundaries, and a homogeneous Neumann boundary at impenetrable walls. The initial condition for the temperature is not restricted by continuity. An initial temperature can be obtained by solving a simple Poisson equation

$$-\frac{\partial^2 T}{\partial x_i \partial x_i} = 0 \tag{16}$$

subject to know fixed surface temperature distributions.

Chapter III

The Continuity Constraint and Pressure

For CFD simulation of incompressible fluid flow, the main difficulty is the satisfaction of the continuity constraint, expressed by (1). Specifically, any solution to the momentum equation must be divergence free and the pressure gradient must be compatible with this solution.

The pressure functions kinematically in the momentum equation as an essential Lagrange multiplier that maintains a solenoidal velocity field. In this view, pressure has a purely mathematical meaning. However, the pressure also has a physical meaning where it is the normal hydrostatic stress in dimensions of force per unit area [3, p.67]. The difficulty is that no algebraic equation of state exists relating pressure to other state variables of the Navier-Stokes equation system, as in compressible flow. Therefore, the pressure corresponding to a solenoidal velocity field is an unknown quantity in the momentum equation (2), and either a dependent variable transformation must be used to eliminate the appearance of the pressure gradient term entirely, or an approximate continuity enforcement model must be applied to enforce the action of pressure.

Pressure determination

A pressure Poisson equation (PPE) can be derived by forming the divergence of the momentum equation (2). The form is

$$L(P) = \frac{\partial}{\partial x_i}(L(u_i)) = \frac{\partial^2 P}{\partial x_i \partial x_i} + \frac{\partial}{\partial x_i}\left(u_j \frac{\partial u_i}{\partial x_j}\right) - Ar\frac{\partial \Theta}{\partial x_i}\delta_{ig} + \frac{\partial}{\partial x_i}\left(\frac{\partial u_i}{\partial t}\right) - \frac{\partial^2}{\partial x_i \partial x_j}\left(\frac{1}{Re^f}\frac{\partial u_i}{\partial x_j}\right) = 0 \tag{17}$$

If the velocity field appearing in equation (18) is indeed divergence free, the time and viscosity terms vanish identically using the communitive property of derivatives and the continuity equation (1). Otherwise, these terms must be evaluated, which presents the main difficulty of accurately determining the third-order spatial derivative that appears in the velocity diffusive term. Formulations which solve the pressure via the Poisson equation are referred to as PPE formulations in the literature [2].

Boundary conditions for the PPE formulation are usually derived [4] by projecting the momentum equation onto Γ in the normal and tangential directions. The normal direction projection results in a non-homogeneous Neumann condition of the form

$$L(u_i)n_i \Rightarrow \frac{\partial P}{\partial n} = \frac{1}{Re^f}\nabla^2 u_n - u_n\frac{\partial u_n}{\partial n} - \frac{\partial u_n}{\partial t} + Ar\Theta\delta_{ig}n_i \tag{18}$$

The tangential projection requires integration over the boundary surface Γ resulting in a non-homogenous Dirichlet pressure boundary condition. Equation (18) leads to (or induces) solutions for the pressure field that also satisfy this Dirichlet boundary conditions, as verified by Gresho and Sani [4]. In addition, the Neumann condition maintains a divergence-free velocity acceleration at start up (t=0) and throughout the transient (t>0).

A unique solution for the PPE requires at least one Dirichlet constraint on pressure. The homogeneous Neumann condition for velocity on the outflow results in a homogeneous Dirichlet condition for pressure. When a traction boundary condition is applied at the outflow, the pressure is considered known information.

Vector field theory: vorticity-streamfunction formulation

The pressure term can be eliminated in equation (2) only by taking the curl of momentum. The resulting vorticity transport equation for a two dimensional velocity field is

$$L(u_i)\varepsilon_{3ij} = L(\omega) = \frac{\partial\omega}{\partial t} + \frac{\partial}{\partial x_j}\left(u_j\omega - \frac{1}{Re^f}\frac{\partial\omega}{\partial x_j}\right) - Ar\frac{\partial\Theta}{\partial x} = 0; \qquad 1 \le i,j \le 2 \tag{19}$$

with the corresponding vorticity definition

$$\omega \equiv \frac{\partial u_i}{\partial x_j}\varepsilon_{3ij} = \left(\frac{\partial v}{\partial x} - \frac{\partial u}{\partial y}\right) \tag{20}$$

A divergence free velocity vector field in two dimensions can be guaranteed the curl of the x_3 scalar component of a vector potential function as

$$u_i = \frac{\partial\psi\hat{k}}{\partial x_j}\varepsilon_{ijk} \tag{21}$$

where ψ is called the streamfunction. Equation (21) satisfies continuity identically, and eliminating u_i in the vorticity transport equation yields

$$L(\omega) = \frac{\partial \omega}{\partial t} + \frac{\partial}{\partial x_j}\left(\frac{\partial \psi}{\partial x_j}\varepsilon_{ij3}(\omega) - \frac{1}{Re^f}\frac{\partial \omega}{\partial x_j}\right) - Ar\frac{\partial \Theta}{\partial x} = 0; \qquad (22)$$
$$1 \le i, j \le 2,$$

The vorticity transport equation now requires that compatibility must be established between streamfunction and vorticity. Replacing the velocity vector field with the streamfunction in equation (20) produces the Poisson compatibility equation

$$L(\psi) = -\frac{\partial^2 \psi}{\partial x_i \partial x_i} - \omega = 0 \qquad (23)$$

The boundary conditions for vorticity and streamfunction can be determined from their comparisons to equations (20) and (21), respectively. At any inflow boundary, equation (21) requires the conservation of mass flow

$$\hat{n}_i \bullet u_i(\tau)h = \Delta\psi \qquad (24)$$

where h is the dimension across the inflow region. On the inflow plane itself, a vanishing Neumann condition is used for streamfunction.

The inflow vorticity Dirichlet condition is obtained from equation (20) as

$$\omega(\tau) = \left(\frac{\partial u_\tau}{\partial n} - \frac{\partial u_n}{\partial \tau} \right) \qquad (25)$$

The homogenous Neumann outflow condition for velocity results in the same for vorticity and stream function.

The wall boundary condition for streamfunction in a simply connected domain is Dirichlet data as determined by the mass flow rate applied at the inflow boundary. For multiply connected domains, the boundary streamfunction values cannot be easily determined. The inability to apply such a Dirichlet constraint in multiply connected domains for streamfunction is one of the main detractions of the vorticity-streamfunction formulation.

The wall vorticity boundary condition is a reduced form of the compatibility condition, equation (23), as

$$\omega_w = -\left.\frac{\partial^2 \psi}{\partial n^2}\right|_w \tag{26}$$

where subscript w identifies the wall boundary. The differential equation (26) requires a numerical approximation for specifying the second-order normal derivative of streamfunction [5]. A Taylor series expansion on streamfunction produces such a finite-difference expression of all order derivatives of streamfunction. The first-order normal derivative is the velocity component parallel to the wall, i.e.,

$$\left.\frac{d\psi}{dn}\right|_w = -u_\tau \tag{27}$$

A second-order accurate approximation for the vorticity at the wall is [5]

$$\omega_w = -3\left(\frac{\psi_{w+1} - \psi_w}{\Delta n^2}\right) - \frac{\omega_{w+1}}{2} - \frac{3u_\tau}{\Delta n} + O\left(\Delta n^3\right) \tag{28}$$

Figure 1 is a sketch of the wall boundary geometry

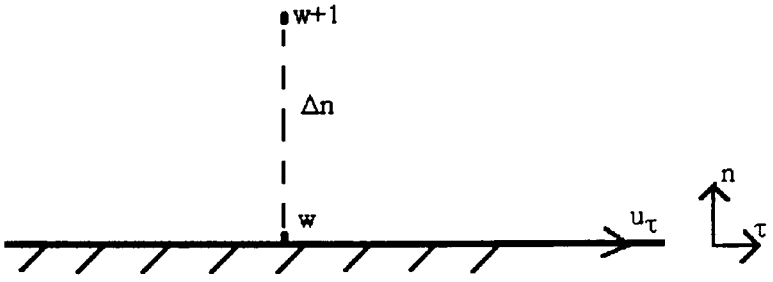


Figure 1
Vorticity Kinematic Constraint Geometry at a Wall

where Δn is the normal distance separating wall values (w) and the nearest interior neighbor (w+1). A homogenous Neumann condition for both streamfunction and vorticity is a applied at symmetry planes.

Pressure relaxation: PPE algorithm

The derivation of a PPE algorithm begins via a time semi-discretization of the momentum equation (2). Using a θ-implicit Taylor series yields

$$u_i^{n+1} - u_i^n = -\theta\Delta t\frac{\partial}{\partial x_j}\left\{u_i u_j + P\delta_{ij} - \frac{1}{Re^f}\frac{\partial u_i}{\partial x_j}\right\}^{n+1} \tag{29}$$
$$(1-\theta)\Delta t\frac{\partial}{\partial x_j}\left\{u_i u_j + P\delta_{ij} - \frac{1}{Re^f}\frac{\partial u_i}{\partial x_j}\right\}^{n} + O\left(\Delta t^3\right)$$

where both u_i^{n+1} and u_i^n are assumed divergence free velocity fields with the corresponding pressure distributions P^n and P^{n+1}. However, the solenoidal velocity field and corresponding pressure are both unknowns at the new time (n+1). Therefore, an estimate is usually made of the pressure P_A for determining an approximate velocity field $\tilde{u}_i$, which is unlikely to be solenoidal. The Taylor series expression then becomes

$$\tilde{u}_i^{n+1} - u_i^n = -\theta\Delta t\frac{\partial}{\partial x_j}\left\{\tilde{u}_i\tilde{u}_j + P_A\delta_{ij} - \frac{1}{Re^f}\frac{\partial \tilde{u}_i}{\partial x_j}\right\}^{n+1} \tag{30}$$
$$(1-\theta)\Delta t\frac{\partial}{\partial x_j}\left\{u_i u_j + P\delta_{ij} - \frac{1}{Re^f}\frac{\partial u_i}{\partial x_j}\right\}^{n} + O\left(\Delta t^2\right)$$

The error in the velocity estimate $\tilde{u}_i^{n+1}$ is determined by subtracting equations (30) and (29), which yields.

$$\left(u_i - \tilde{u}_i\right)^{n+1} = -\theta\Delta t\frac{\partial}{\partial x_j}\left\{\left(u_i u_j - \tilde{u}_i\tilde{u}_j\right) + \left(P - P_A\right)\delta_{ij} - \frac{1}{Re^f}\left(\frac{\partial u_i}{\partial x_j} - \frac{\partial \tilde{u}_i}{\partial x_j}\right)\right\}^{n+1} \tag{31}$$

Under certain restrictions [13], the convective and diffusive terms on the right hand side of equation (31) will vanish. Therefore, from vector field theory the curl of equation (31) vanishes, hence the vector field difference can be expressed as a gradient of a scalar potential function

$$\left(u_i - \tilde{u}_i\right)^{n+1} \equiv -\frac{\partial \phi^{n+1}}{\partial x_i} \tag{32}$$

In order to insure a nominally zero potential gradient, equation (31) must be solved with iterative cycling

through the momentum equation [13]. Simplifying the convection term in (32) by replacing $\tilde{u}_j$ with u_j and expressing the velocity error as a vector value ($e_i = u_i - \tilde{u}_i$), the approximation error of equation (31) is expressed in an iterative form as

$$(e_i)_{p+1}^{n+1} \approx -\theta\Delta t \frac{\partial}{\partial x_j}\left\{ u_j e_i + (P - P_A)\delta_{ij} - \frac{1}{Re^f}\frac{\partial e_i}{\partial x_j}\right\}_p^{n+1} \tag{33}$$

Again, a conservative error requires truncating the convective and diffusive terms, the gradient potential is then expressed as

$$(u_i - \tilde{u}_i)_{p+1}^{n+1} \approx -\frac{\partial \phi_{p+1}^{n+1}}{\partial x_i} \tag{34}$$

Directly from equation (33), a pressure expression can be obtained

$$\theta\Delta t \frac{\partial (P - P_A)_p^{n+1}}{\partial x_i} = \frac{\partial \phi_{p+1}^{n+1}}{\partial x_i} \tag{35}$$

$$\Rightarrow P^{n+1} = P_A + \frac{1}{\theta\Delta t}\phi_{p+1}^{n+1} + C;\ C = 0$$

The iteration index has been removed from P^{n+1} since no iteration is required on the action of the divergence free pressure field being sought. The right hand side of equation (35) exemplifies the iterative process which approximates the action of the required pressure field in a momentum solution process.

The divergence of equation (34), and employing the continuity constraint, produces a Poisson equation for ϕ in the form

$$-\frac{\partial^2 \phi}{\partial x_i \partial x_i} + \frac{\partial \tilde{u}_i}{\partial x_i} = 0 \tag{36}$$

Closure of this Poisson equation requires specification of boundary conditions for ϕ all around Γ. Neumann constraint is identified by the normal projection of the gradient expression (32) onto the boundary

$$(u_i - \tilde{u}_i)n_i \equiv -\frac{\partial \phi}{\partial x_i} n_i \text{ on } \Gamma_N \tag{37}$$

which becomes homogenous on all Γ_D for velocity. For a unique solution, a Dirichlet constraint for ϕ

must be identified. The admissible algorithm must seek to drive $\phi_p \Rightarrow 0$ as the iterations proceed. Therefore, the remaining outflow boundary is set to zero where a vanishing Neumann boundary condition exists for velocity.

Chapter IV

Finite Element Weak Statement Algorithm

Conservation law form

Each initial value statement PDE presented in Chapter III can be expressed in the conservation law form as

$$L(q) = \frac{\partial q}{\partial t} + \frac{\partial}{\partial x_j}\left(f_j - f_j^v\right) - s_q = 0 \tag{38}$$

In equation (38), $q \equiv (x_i,t)$ is the "state variable", the functional f_j is the "kinematic flux vector" which contains the convection terms, and f_j^v is the "dissipative flux vector" that contains all diffusive terms. The pressure term is absent, or placed in either f_j or f_j^v depending on the mathematical model. Finally, s_q is the source for the state variable, which includes the body force term of momentum. The state variables and their associated flux vector and source expressions are

$$q = \begin{Bmatrix} u_i \\ \Theta \\ \omega \end{Bmatrix}; f_j = \begin{Bmatrix} u_j u_i \\ u_j \Theta \\ u_j \omega \end{Bmatrix}; f_j^v = \begin{Bmatrix} \frac{1}{Re^f}\frac{\partial u_i}{\partial x_j} \\ \frac{1}{Pe^f}\frac{\partial \Theta}{\partial x_j} \\ \frac{1}{Re^f}\frac{\partial \omega}{\partial x_j} \end{Bmatrix}; s_q = \begin{Bmatrix} -Ar\Theta\delta_{ig} \\ s_q \\ Ar\frac{\partial \Theta}{\partial x_j}\varepsilon_{ij}\delta_{ig} \end{Bmatrix} \tag{39}$$

In addition to equation (38), various algorithms selectively contain Poisson equations written on the auxiliary variables in the form

$$L(q_a) = -\frac{\partial^2 q_a}{\partial x_i \partial x_i} - s(q) = 0 \tag{40}$$

where q_a is the auxiliary variable (e.g., ψ and ϕ) and $s(q)$ is the corresponding source dependent on a state variable of the system.

Taylor modified conservation law statement

The numerical solution of each initial value PDE statement requires a semi-discrete approximation of the time evolution due to the presence of the first-order time derivative. One method of approximation is a θ-

implicit Taylor series expansion

$$q^{n+1} = q^n + \Delta t\left(\theta\frac{\partial q^{n+1}}{\partial t} + (1-\theta)\frac{\partial q^n}{\partial t}\right) + O(\Delta t^3) \tag{41}$$

which can provide for second-order accuracy when θ=1/2, where θ determines the position in the time interval ($\Delta t=t^{n+1}-t^n$) at which the Taylor series is evaluated. At progressively larger Reynolds numbers (or Peclet numbers), the diffusive character of the conservation law statement diminishes, hence equation (38) exhibits a more hyperbolic character. The larger Reynolds numbers tend to create sharp gradients especially near Γ_D, that may trigger numerical solution oscillations on insufficient spatial discretizations. These solution oscillations appear typically of the wavelength 2h, where h is a local mesh length measure.

A theory for damping these oscillations suggests retaining the higher order time derivative in the Taylor series expansion of equation (41). The next higher order form of equation (41) produces a modified form of the statement [6]

$$L_m(q) = \frac{\partial q}{\partial t} + \frac{\partial}{\partial x_j}\left(f_j - f_j^v\right) - s_q - \frac{\Delta t}{2}\frac{\partial}{\partial x_j}\left(\bar{\beta}A_j A_k \frac{\partial q}{\partial x_k}\right) \tag{42}$$

where A_j $(\frac{\partial f_j}{\partial q})$ is the jacobian (matrix) of the kinematic flux vector. In equation (42), the notation L_m identifies the Taylor series modified statement, and $\bar{\beta}$ is an arbitrary coefficient. The jacobian state variable system is

$$q = \begin{Bmatrix} u_i \\ \Theta \\ \omega \end{Bmatrix}; \; A_j = \begin{bmatrix} u_j + u_i\delta_{ij} & 0 & 0 \\ 0 & u_j & 0 \\ 0 & 0 & u_j \end{bmatrix} \tag{43}$$

The weak statement

A numerical approximate solution is sought for the given initial value statements and Poisson equations since an analytical solution is not readily obtained. The selected approximation technique employs the weak statement, where the inner product of the approximation to the governing PDE systems with a weight function is required to vanish. The weak statement in integral form is

$$WS \equiv \int_{\Omega} wL_m(q^N)d\Omega = 0, \text{ for all } w(x_i,t) \tag{44}$$

where $w=w(x_i,t)$ is any Lebesque integrable function and q^N is an approximation to the solution of $L_m(q)$. Inherent within any approximation is its associated error, and placement into L(q) is a measure of the error in the solution, i.e., $L_m(q^N) \neq 0$. The weak statement requires this approximation error measure to vanish in an integrated sense over Ω for any set of functions, w.

The weak statement to the general form of the conservation law statement given in equation (38) is

$$TWS = \int_{\Omega} wL_m(q^N)d\Omega = \int_{\Omega} w\left(\frac{\partial q^N}{\partial t} + \frac{\partial (fj)^N}{\partial xj}\right)d\Omega + \int_{\Omega} \frac{\partial w}{\partial x_j}\left(f_j^v\right)^N d\Omega$$
$$+ \frac{\Delta t}{2}\int_{\Omega} \frac{\partial w}{\partial x_j}\left(\bar{\beta}A_jA_k\frac{\partial q^N}{\partial x_k}\right)d\Omega - \oint_{\partial\Omega} w(f_j^v)^N n_j d\Omega = 0 \tag{45}$$

where the Green-Gauss theorem is applied to the dissipative flux vector and the augmenting $\bar{\beta}$ term, thereby reducing the order of differentiation required of the trial space and permitting direct enforcement of Neumann conditions on the boundary within the resulting surface integrals. The $\bar{\beta}$ expression is not applied at the boundaries, hence the created surface integral vanishes identically.

The weak statement for the auxiliary Poisson equation is

$$WS = \int_{\Omega} wL\left(q_a^N\right)d\Omega = \int_{\Omega} \frac{\partial w}{\partial x_i}\frac{\partial q_a^N}{\partial x_i}d\Omega + \int_{\Omega} ws\left(q^N\right)d\Omega - \oint_{\partial\Omega} w\frac{\partial q_a^N}{\partial x_i}n_i d\Omega = 0 \tag{46}$$

The approximation, q^N, and the weight function, $w(x_i,t)$, are each implemented using projection onto an appropriate set of the trial and test function spaces [7]. Assuming space and time separable, the approximate solution form is

$$q(x_i,t) \cong q^N(x_i,t) \equiv \sum_{k=1}^{N} \Psi_k(x_i)Q_k(t) \tag{47}$$

where Ψ_k is a trial space member, containing all spatial dependency, and Q_k is the (unknown) time dependent expansion coefficient set. Since w is known, then its interpolation is

$$w(x_i,t) \equiv w^M(x_i,t) \equiv \sum_{k=1}^{M} \Phi_k(x_i) W_k(t) \tag{48}$$

where Φ_k is the space of test functions with W_k the known (time dependent) coefficient set. The Galerkin criteria requires the trial space and the test space to contain identical members. Further, since the time dependence in $w(x_i,t)$ thus totally supported by $W_k(t)$, the stationary point of the Taylor modified conservation law weak statement of equation (45) is

$$\begin{aligned} TWS = \int_\Omega \Psi_k L_m(q^N) d\Omega = \int_\Omega \Psi_k \left(\frac{\partial q^N}{\partial t} + \frac{\partial (fj)^N}{\partial x_j} \right) d\Omega + \int_\Omega \frac{\partial \Psi_k}{\partial x_j} (f_j^v)^N d\Omega \\ + \frac{\Delta t}{2} \int_\Omega \frac{\partial \Psi_k}{\partial x_j} \left(\bar{\beta} A_j A_k \frac{\partial q^N}{\partial x_k} \right) d\Omega - \oint_{\partial\Omega} \Psi_k (f_j^v)^N n_j d\Omega = 0 \end{aligned} \tag{49}$$

where TWS represents "Taylor weak statement". The companion stationary Galerkin weak statement for the Poisson equation of equation (46) is

$$GWS = \int_\Omega \Psi_k L\left(q_a^N\right) d\Omega = \int_\Omega \frac{\partial \Psi_k}{\partial x_i} \frac{\partial q_a^N}{\partial x_i} - \int_\Omega \Psi_k \, s\left(q^N\right) d\Omega - \oint_{\partial\Omega} \Psi_k \frac{\partial q_a^N}{\partial x_i} d\Omega = 0 \tag{50}$$

Spatial semi-discretization

The finite element method employs a spatial semi-discretization of Ω and defines trial space members locally using Lagrange polynomials defined on individual elements making up the domain discretization. The local weak statement integrals are then assembled over the domain to determine the spatially discrete governing equations. The variable interpolation is then expressed as

$$\begin{aligned} q^N(x_i,t) \equiv q^h(x_i,t) = \bigcup_e q_e(x_i,t); \\ q_e(x_i,t) = \left\{ N_I^+(\eta_j) \right\}^T \{Q\}_e \end{aligned} \tag{51}$$

where subscript e denotes element value. $\{Q\}_e$ is the column vector of the variable interpolated by the basis given in equation (47) at the nodal points of the element. The basis used for this thesis project is the isoparametric bilinear quadrilateral basis

$$\left\{N_I^+\right\} = \frac{1}{4}\begin{Bmatrix}(1-\eta_1)(1-\eta_2)\\(1+\eta_1)(1-\eta_2)\\(1+\eta_1)(1+\eta_2)\\(1-\eta_1)(1+\eta_2)\end{Bmatrix} \tag{52}$$

where η_1 and η_2 are the local coordinate system on the element.

The TWS is defined in terms of the global coordinate space (x_i), whereas the basis definition uses the element local system (η_i). To evaluate the integrals, a coordinate transformation from global to local uses the same basis set used for the variable approximation. Hence,

$$\begin{aligned} x_e &= \left\{N_I^+(\eta_j)\right\}^T \{X\}_e \\ y_e &= \left\{N_I^+(\eta_j)\right\}^T \{Y\}_e \end{aligned} \tag{53}$$

where $\{X\}_e$ and $\{Y\}_e$ are the nodal coordinates of Ω_e.

Following the given spatial discretization, the TWS then becomes expressed using the assembly operation as

$$\begin{aligned} TWS^h = S_e\Bigg(& DET_e \int_{\Omega_e} \left\{N_I^+\right\}\left\{N_I^+\right\}^T d\eta_1 d\eta_2 \{Q\}'_e + ETAJK_e \int_{\Omega_e} \left\{N_I^+\right\} \frac{\partial\left\{N_I^+\right\}^T}{\partial\eta_k} d\eta_1 d\eta_2 \{FJ\}_e \\ & + \frac{ETAJK_e ETAJM_e}{DET_e} \int_{\Omega_e} \frac{\partial\left\{N_I^+\right\}}{\partial\eta_k} \frac{\partial\left\{N_I^+\right\}^T}{\partial\eta_m} d\eta_1 d\eta_2 \{FVJ\}_e \\ & + \frac{\Delta t\overline{\beta_e}}{2} \frac{ETAJM_e ETAKL_e}{DET_e} \int_{\Omega_e} \frac{\partial\left\{N_I^+\right\}}{\partial\eta_m} \Bigg(\left\{N_I^+\right\}^T \{AJ\}_e \left\{N_I^+\right\}^T \{AK\}_e \frac{\partial\left\{N_I^+\right\}^T}{\partial\eta_l} \Bigg) d\eta_1 d\eta_2 \{Q\}_e \\ & - DET2_e \oint_{\partial\Omega_e} \left\{N_I^+\right\}\left\{N_I^+\right\}^T d\Omega \{FVJ\}_e \{NJ\}_e d\eta_1 d\eta_2 \Bigg) = \{0\} \end{aligned} \tag{54}$$

where S_e denotes assembly of element operations over the discretization. The data $ETAJI_e$ in equation (54) are the element-average metric data set representing the derivative transformation from the element (local) to global coordinate system [7;p. 223], and DET_e is the element centroidal value of the determinant

of the forward transformation (from global to the local space). $DET2_e$ is the corresponding measure of the surface integral. The terms $\{FJ\}_e$ and $\{FVJ\}_e$ are column matrices containing nodal values of the kinematic and dissipative flux vector approximations, respectively. Correspondingly, $\{AJ\}_e$ and $\{AK\}_e$ are column matrices of the kinematic flux vector jacobian approximation nodal values.

Similarly, the finite element weak statement for the Poisson equation (50) becomes the assembly operation

$$GWS^h = S_e\left(\frac{ETAIK_e ETAIL_e}{DET_e} \int_{\Omega_e} \frac{\partial\{N_I^+\}}{\partial\eta_k}\frac{\partial\{N_I^+\}^T}{\partial\eta_l} d\eta_1 d\eta_2 \{QA\}_e + DET_e \int_{\Omega} \{N_I^+\}\{N_I^+\}^T d\eta_1 d\eta_2 \{Q\}_e \right.$$
$$\left. - DET2_e \oint_{\partial\Omega_e} \{N_I^+\}\frac{\partial\{N_I^+\}^T}{\partial\eta_l} d\eta_1 d\eta_2 \{QA\}_e \{NI\}_e \right) = \{0\} \qquad (55)$$

The integral statements of equations (54) and (55) from matrix statements. The specific matrix forms are given in Appendix I.

The $\bar{\beta}$ term in equation (54) may be modified to eliminate the presence of the time step Δt. A steady-state solution is considered the limit as time approaches infinity, hence Δt may become quite large. For a time evolution solution procedure, the local time step size is regularly adjusted dependent on convergence. Hence, numerical dissipation contributed by the $\bar{\beta}$ expression can adversely increase via Δt and 'swamp' the solution approximation. The time step Δt can be eliminated by introducing an element level Courant number

$$\left(\frac{\bar{\beta}\Delta t}{2}\right)_e \cong \frac{\nu_q \sqrt{DET_e}}{2\left|(u_j)_e\right|} \qquad (56)$$

Here, ν_q is an specifiable positive parameter controlling the numerical dissipation level independent of Δt and $|(u_j)_e|$ is the element average velocity magnitude. Computational experiments by Noronha and Baker [6] demonstrate that the level of ν_q can be dependent on the specific problem and the continuity model. Experience has shown that the preferred method is to gradually increase ν_q until the solution

oscillation are damped, then adjust the mesh to better resolve the local solution gradients.

Time integration algorithm

The matrix forms of the finite element discretized weak statements for the conservation law statement, equation (54), and any auxiliary Poisson equation (55) have been developed. In compact form, the conservation law weak statement is

$$TWS^h = [M]\{Q\}' + \{R(Q)\} = \{0\} \tag{57}$$

where [M] is a global rank square matrix, $\{Q\}'=d\{Q\}/dt$, and $\{R(Q)\}$ is the residual column matrix containing all but the first assembled terms in equation (54).

The companion weak statement of the Poisson equation is

$$GWS^h = [D]\{QA\} - \{S(Q)\} = \{0\} \tag{58}$$

where [D] is the square, global-rank, diffusion matrix and $\{S(Q)\}$ the column matrix of the source term.

Equation (57) is a coupled ordinary differential equation (ODE) system requiring evaluation. For the θ-implicit ODE algorithm, equation (57) permits evaluation of the time derivative. Substituting equation (57) into the θ-implicit algorithm produces the matrix algebra statement

$$\begin{aligned}\{F(Q)\} &= [M]\left\{Q^{n+1} - Q^n\right\} - \Delta t\left(\theta\frac{d\{Q\}^{n+1}}{dt} + (1-\theta)\frac{d\{Q\}^n}{dt}\right)\\ &= [M]\{\Delta Q\}^{n+1} + \Delta t\left(\theta\{R\}^{n+1} + (1-\theta)\{R\}^n\right) = \{0\}\end{aligned} \tag{59}$$

where $\{\Delta Q\}$ represents the change in $\{Q\}$ over the time interval Δt. The Newton iterative solution form for (59) [5] is

$$\left[M + \theta\Delta t[J]^{n+1}\right]\{\delta Q\}_{p+1}^{n+1} = -\{FQ\}_p^{n+1};\ [J]^{n+1} = \frac{\partial\{R\}^{n+1}}{\partial\{Q\}^{n+1}} \tag{60}$$

where [J] is the jacobian of the weak statement from equation (59) and p is the iteration index. At convergence, the new time index (n+1) level is accumulated as

$$\{Q\}_{p+1}^{n+1} = \{Q\}^n + \sum_{i=0}^{p}\{\delta Q\}_{i+1}^{n+1} \tag{61}$$

The Newton iteration is performed until $\max|\{\delta Q\}_{p+1}| \le \varepsilon$ where ε is a suitably small number. Appendix

II presents the jacobian ([J]) evaluation for the various state variable selections. The actual implementation of the Newton algorithm for the selected systems is presented in Appendix III.

Chapter V

Discussion and Results

The goal of this thesis project is to assess benchmarking and validation issues for accurate CFD simulation of room air motion problems using the continuity constraint algorithm. Any CFD algorithm/code requires validation with experimental data, but such quality data is very sparse in this problem class. The alternative is benchmarking for simpler problems, where an accepted accurate solution is known, to gain confidence for real engineering analysis. The thesis project focuses on two-dimensional problems, and addresses the issues of accuracy, convergence, efficiency, and artificial viscosity for the continuity constraint algorithm, as a complement to the vorticitity-stream function finite element CFD formulation results [14].

Three benchmark problems are selected to support this goal. The first is the thermal cavity in which a fixed temperature difference exists between the two vertical walls of a square cavity. In this problem, the momentum and temperature fields are coupled through the Boussinesq body force term. The second benchmark is the close-coupled, isothermal step-wall diffuser, for which detailed experimental data exist [10]. The third benchmark problem is the thermal backward-facing step, with the momentum and temperature solutions decoupled, and a heat flux applied at the channel walls for determining appropriate outflow boundary conditions on temperature.

Following the benchmark problems, CFD simulation experiments for a full-scale laboratory room are presented for validation. These results obtained using the continuity constraint algorithm are then compared with the experimental data of Zhang et al [15].

Thermal cavity

The thermal cavity problem is a classic benchmark problem for buoyancy-driven flows. The problem consists of a square cavity with differentially heated walls. Figure 2 is a sketch of the problem domain and the boundary conditions.

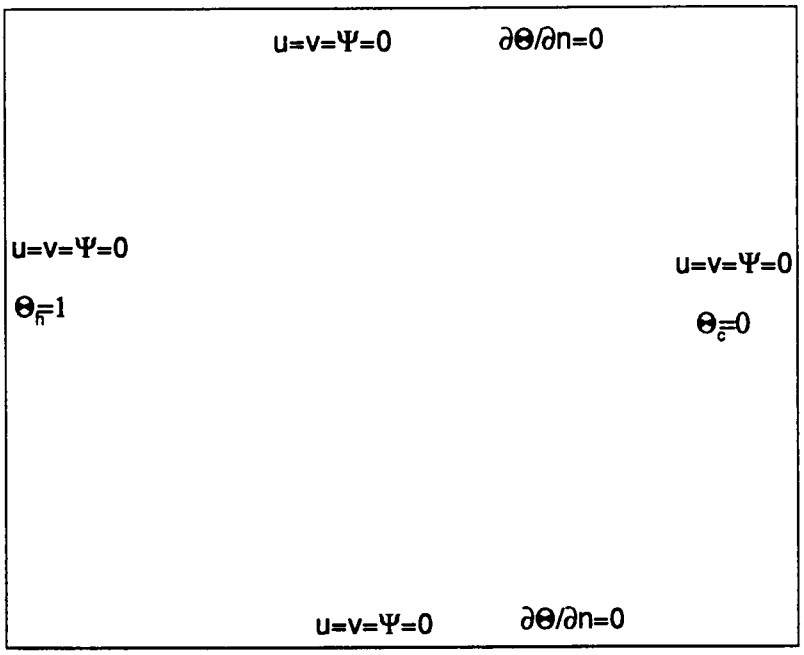


Figure 2
Thermal Cavity Boundary Conditions

Simulations are performed for Rayleigh numbers of 10^3, 10^4, 10^5, and 10^6 where Ra=GrPr for equation (2). The results obtained are compared with the CFD solutions of de Vahl Davis [16], who performed a mesh refinement and extrapolation procedure to achieve what is believed to be considerable soluton accuracy. He used a second-order finite difference, uniform mesh approximation for conducting these simulations, with refinement performed by doubling the mesh density. The mesh sizes used were 11x11, 21x21, 41x41, and 81x81.

The thermal cavity simulation is of specific use for constructing adequate meshes for the room air motion simulations. A mesh refinement was performed in the present analysis, but the goal is a mesh sizing not exceeding what generates an "engineering adequate solution", i.e., one free of mesh scale oscillations and detailed enough to capture solution details. The results obtained with the continuity constraint algorithm are compared with de Vahl Davis simulations and the verified vorticity-streamfunction formulation for the general character of the flow field variables. For this simulation, the temperature solution process is decoupled from momentum (in the matrix Jacobian, Appendix II) to reduce the workstation core memory requirements, as will be required for the room simulations.

The non-dimensionalization utilizes the velocity scaling for thermal problems given by equation (6). Table I gives the Rayleigh number and the corresponding reference values used in the simulations

Table I
Reference Values For Thermal Cavity Problem (L = 1ft.)

Ra	Gr[1]	$Re=Gr^{1/2}$	U (ft/sec)	t_{ref} (sec)
10^3	$1.47x10^3$	38.34	$6.1x10^{-3}$	163.93
10^4	$1.47x10^4$	121.24	$1.9x10^{-2}$	52.63
10^5	$1.47x10^5$	383.41	0.061	16.39
10^6	$1.47x10^6$	1212.24	0.19	5.26

1 - Pr = 0.68 for air at 70°F

Figures 3 through 7 are excerpted from the de Vahl Davis paper, for comparison purposes. Figures 8 though 13 compare isocline distributions and companion velocity vector distributions obtained with the continuity constraint algorithm and the vorticity-streamfunction formulation, on a uniform 11x11 mesh. The vorticity and streamfunction contours for the continuity constraint algorithm are obtained as a post-processing operation on the velocity field, whereas the velocity field for the vorticity-streamfunction formulation is obtained via post-processing the streamfunction solution. The isocline levels plotted are non-dimensional, and "jaggedness" of the contours at lower Rayleigh numbers ($Ra \leq 10^5$) are attibuted to the sparseness for interpolation between distant nodal points to generate a contour. The continuity constraint and vorticity-streamfunction solutions at Rayleigh numbers of 10^3 through 10^5 are comparable and agree qualitatively in character with the de Vahl Davis solutions. Importantly, solution oscillations appear essentially absent, even on the extremely coarse (engineering) mesh.

At Rayleigh number of 10^6, mesh scale oscillations have developed in both CFD solutions at the upper right hand and lower left hand corners of the domain. The solution oscillations are indicated by isolated "bubbles" and/or "wiggles" in the contour maps. These oscillations are generated by coarse-mesh resolution of the sharp gradients adjacent to vertical walls where the temperature and wall boundary constraints are applied. Comparison of the oscillations at $Ra=10^6$, for continuity constraint and vorticity-streamfunction solutions, confirms the oscillations are more severe with the latter formulation. This is especially apparent in the velocity vector distribution, Figure 13.

Thus, a uniform mesh refinement to 21x21 was performed for the highest Rayleigh number simulations. The steady-state solution at $Ra = 10^5$ on the 11x11 mesh was used as an initial condition for the 21x21 solution mesh for both algorithms. Figures 14 through 19 directly compare these solutions on the two meshes. The 21x21 mesh results confirm the relative absence of solution oscillations of the state variable members which is also reflected in the auxiliary variables, and all are in better agreement with de Vahl Davis. The finer mesh also provides better solution detail for analysis, which is especially observable on the velocity vetor plots, Figure 19

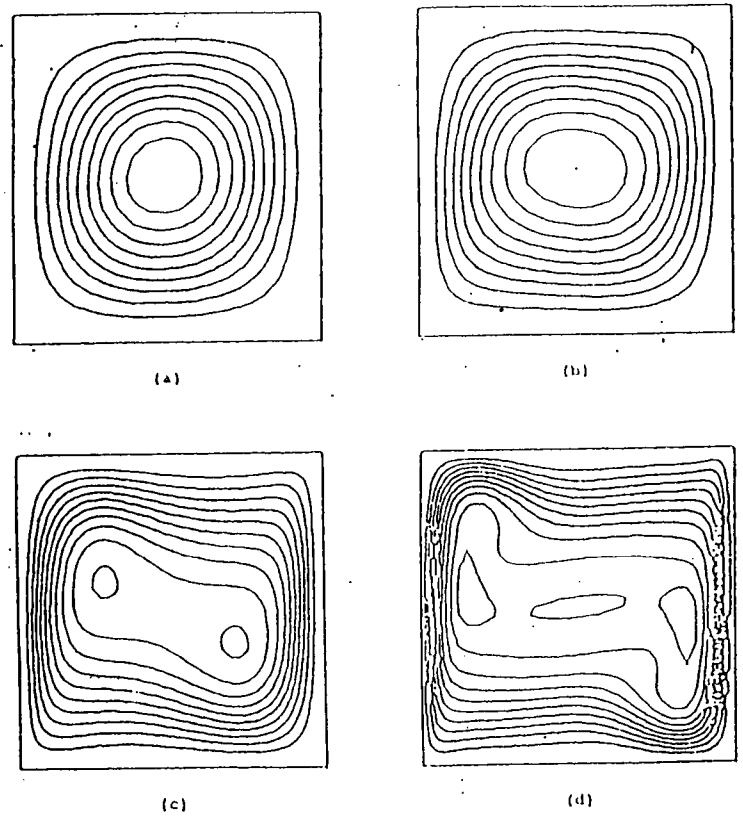


Figure 3
Davis
Streamfunction Contours
a). Ra=10^3; -1.174(0.1174))0;
b). Ra=10^4; -5.071(0.5071)0;
c). Ra=10^5; -9.507,-8.646(0.9607)0;
d). Ra=10^6; -16.27,-15.07(1.675)0

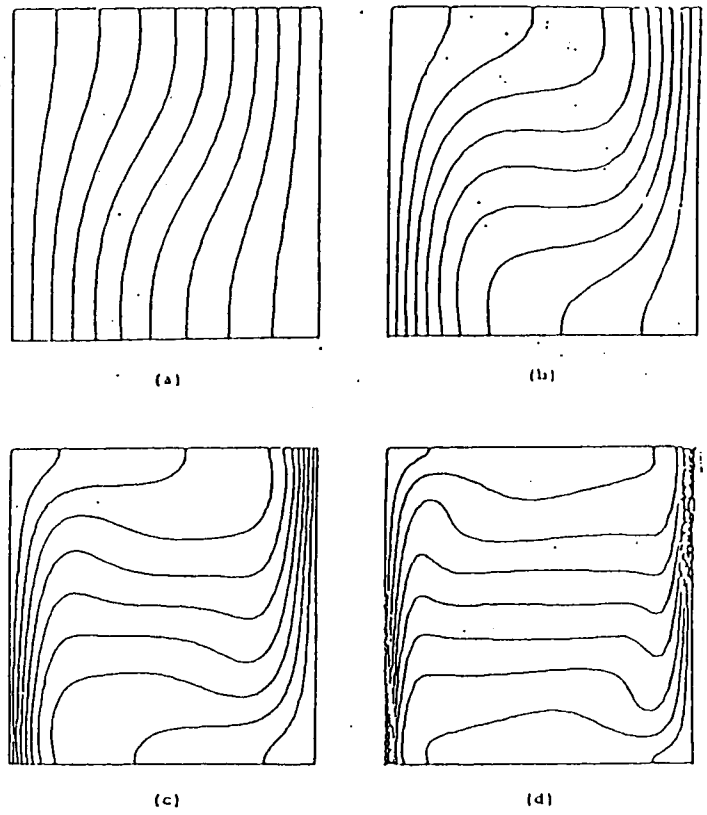


Figure 4
Davis
Temperature Contours
a). Ra=10^3,
b). Ra=10^4,
c). Ra=10^5,
d). Ra=10^6

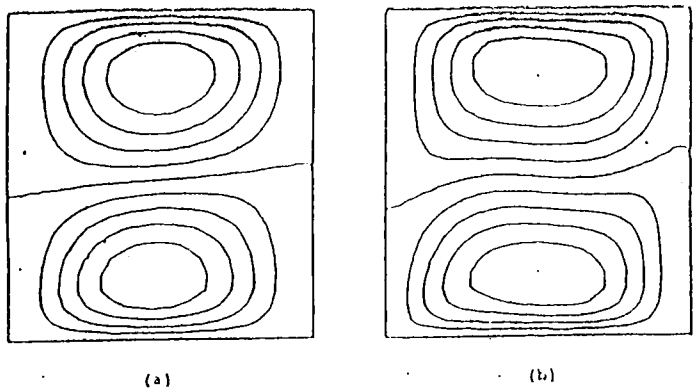


Figure 5
Davis
U Velocity Contours
a). Ra=10^3; -3.637(0.7274)3.637;
b). Ra=10^4; -16.00(3.20)16.00;
c). Ra=10^5; -43.59(8.719)43.59;
d). Ra=10^6; -125.5(25.1)125.5

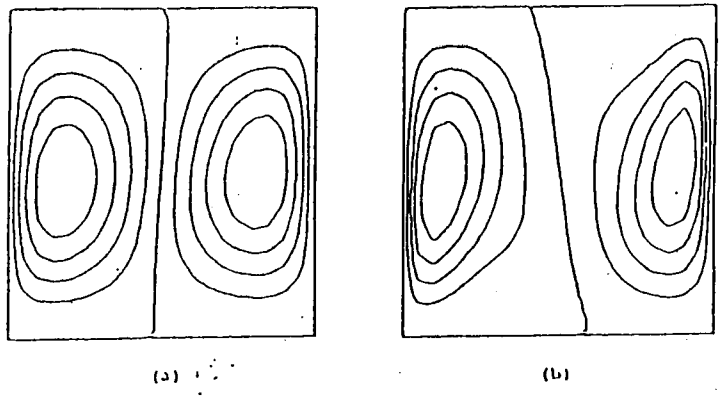


Figure 6
Davis
V Velocity Contours
a). Ra=10^3; -3.663(0.7327)3.663;
b). Ra=10^4; -19.39(3.877)19.39;
c). Ra=10^5; -67.96(13.59)67.96;
d). Ra=10^6; -207.6(41.52)207.6

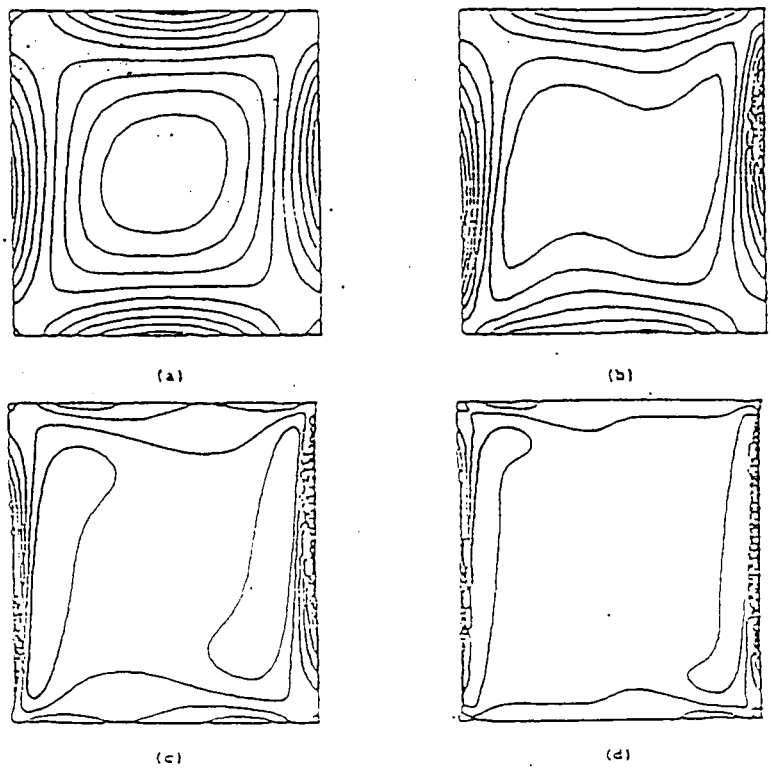
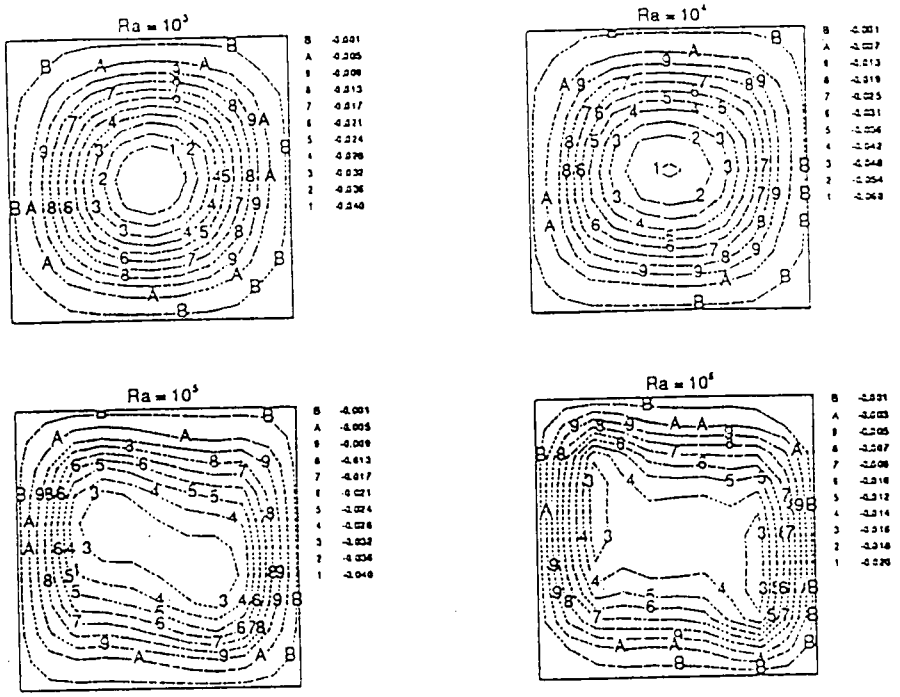
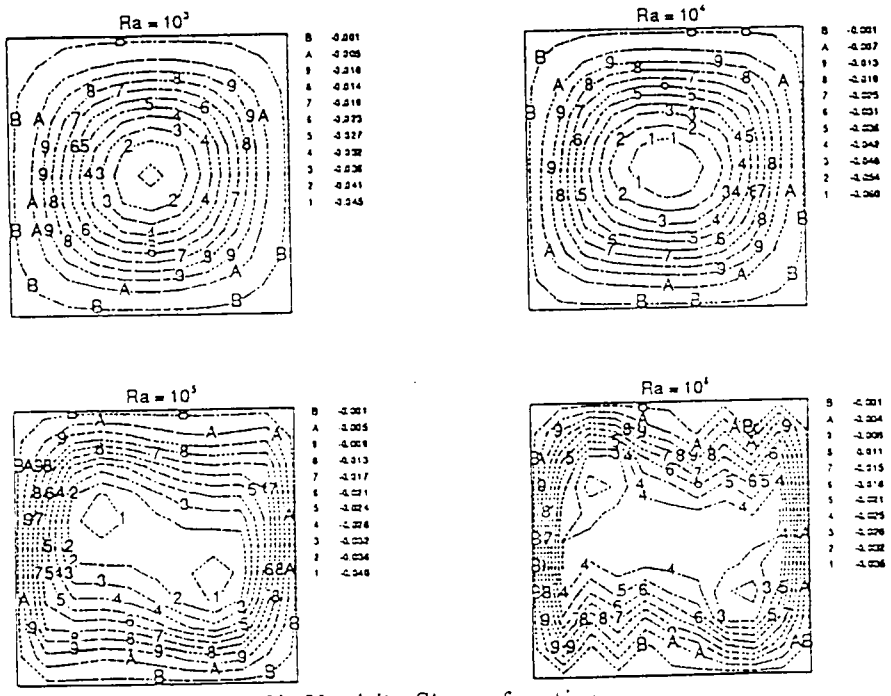


Figure 7
Davis
Vorticity Contours
a). $Ra=10^3$; -32.01(8.328)51.27;
b). $Ra=10^4$; -124.8(55.17)426.9;
c). $Ra=10^5$; -600.0(322.6)2626;
d). $Ra=10^6$; -3178(1847.1)15293

11X11 Uniform Mesh



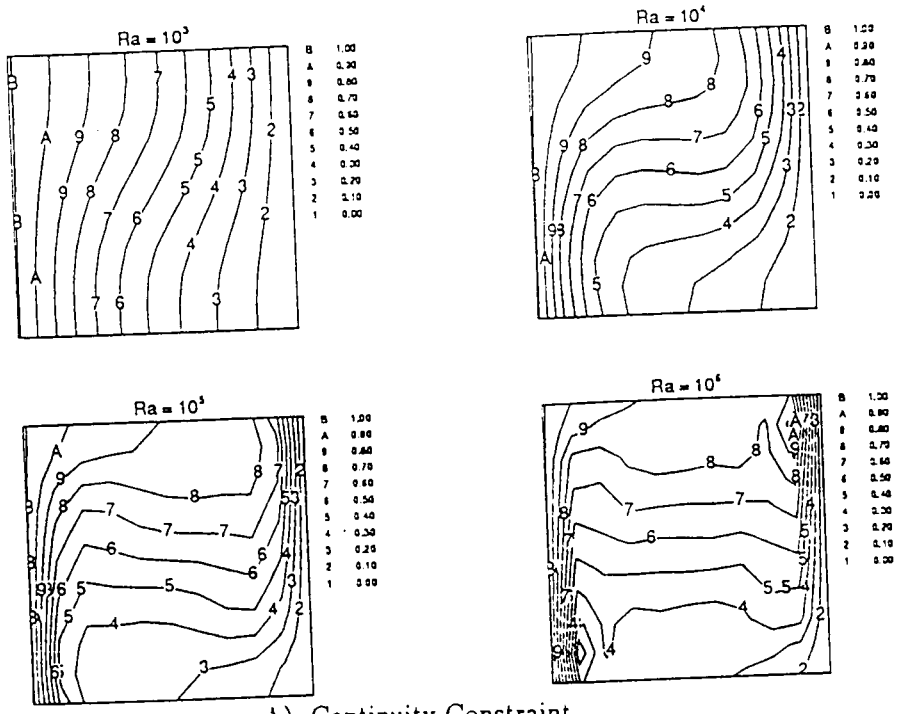
A). Continuity Constraint



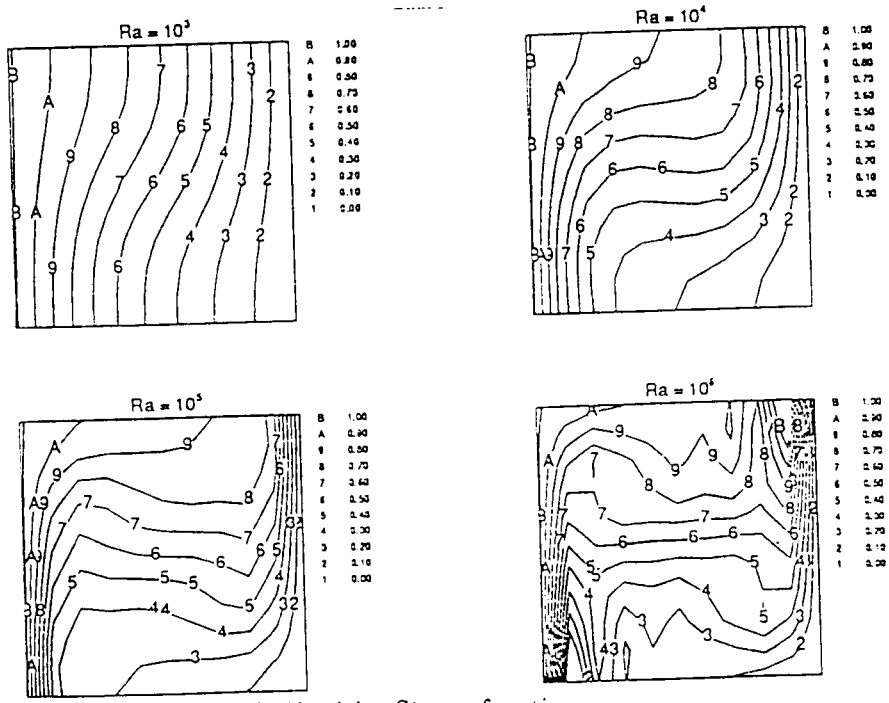
B). Vorticity-Streamfunction

Figure 8
Streamfunction Contours

11X11 Uniform Mesh



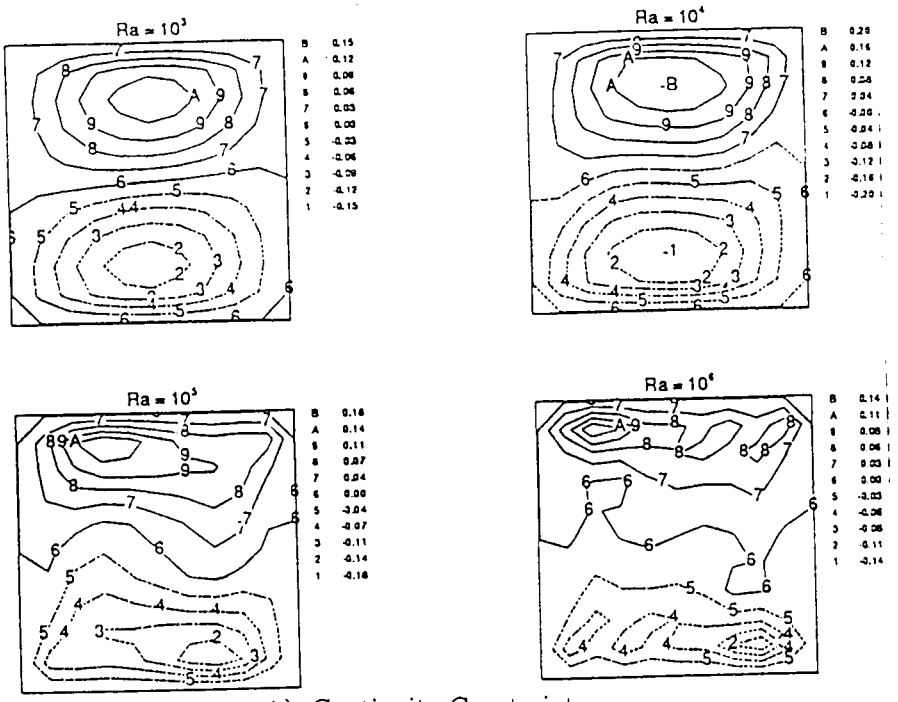
A). Continuity Constraint



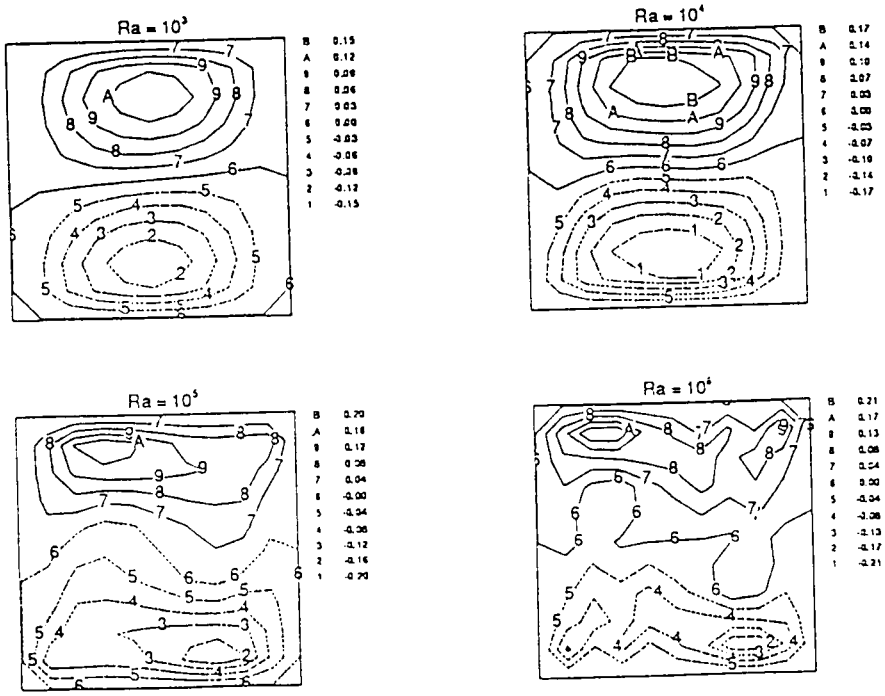
B). Vorticity-Streamfunction

Figure 9
Temperature Contours

11X11 Uniform Mesh



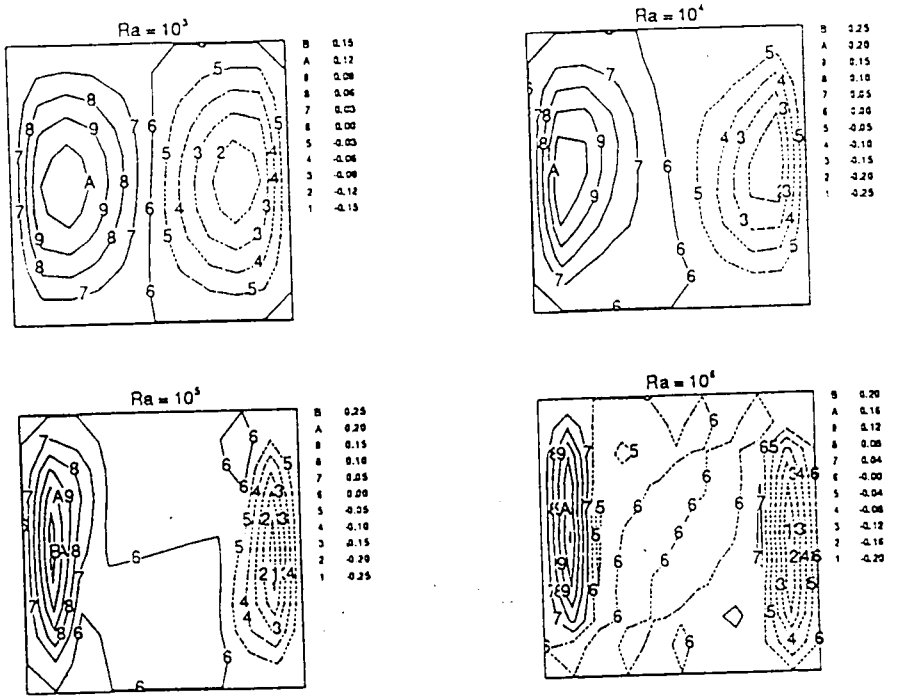
A). Continuity Constraint



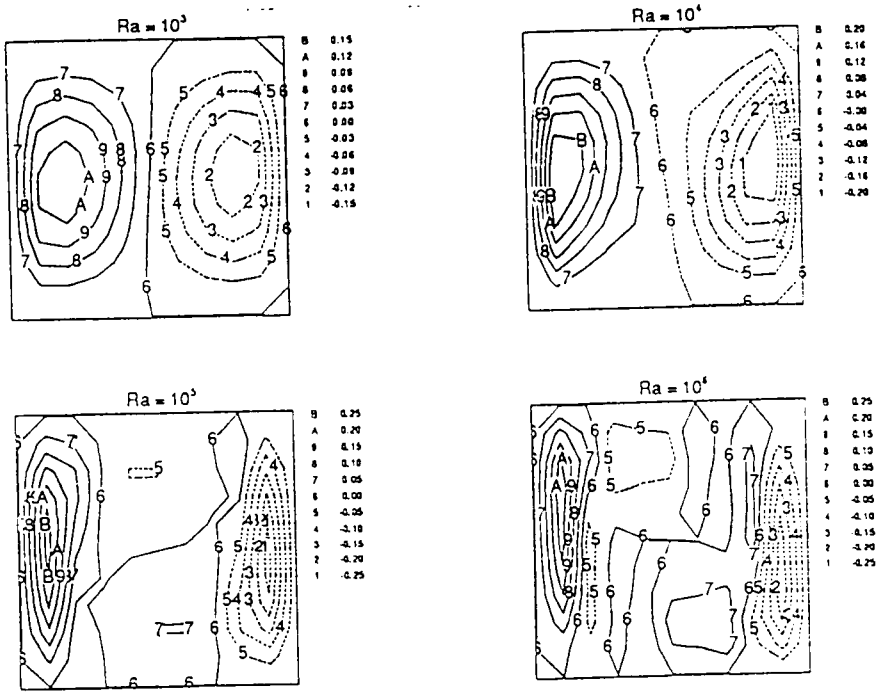
B). Vorticity-Streamfunction

Figure 10
U Velocity Contours

11X11 Uniform Mesh



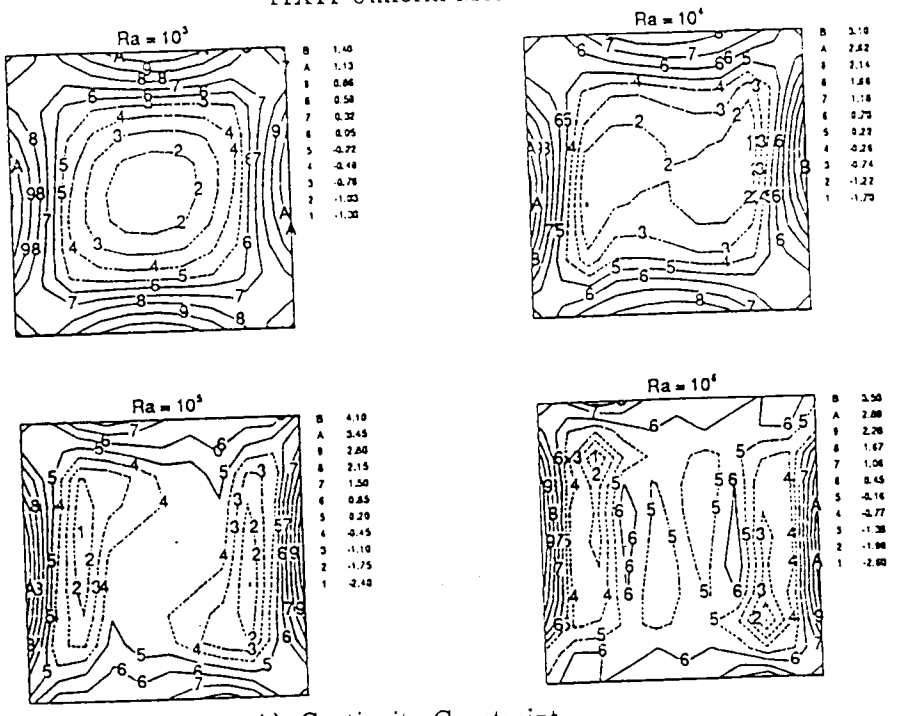
A). Continuity Constraint



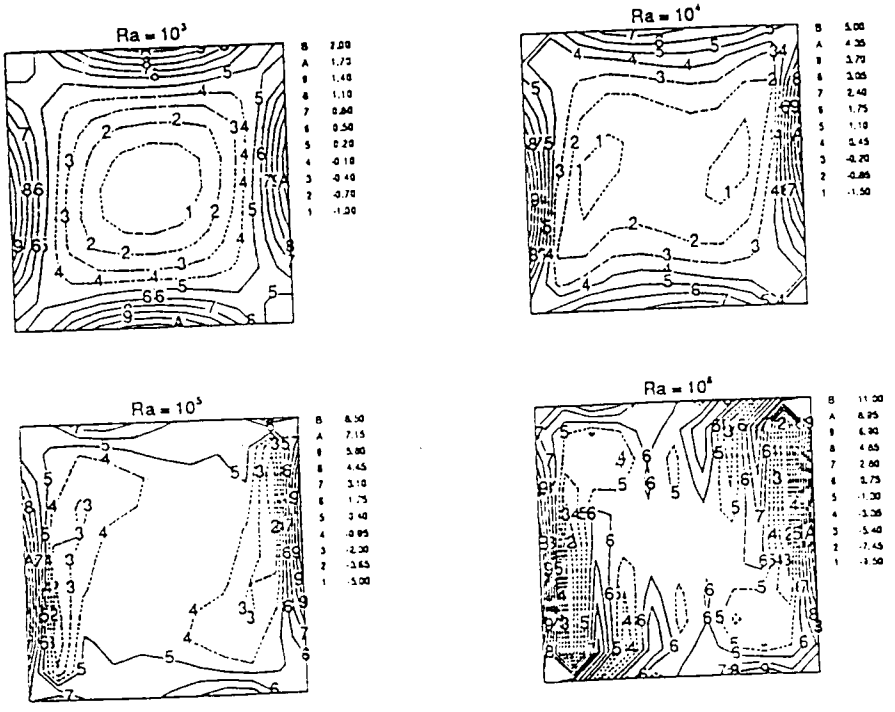
B). Vorticity-Streamfunction

Figure 11
V Velocity Contours

11X11 Uniform Mesh



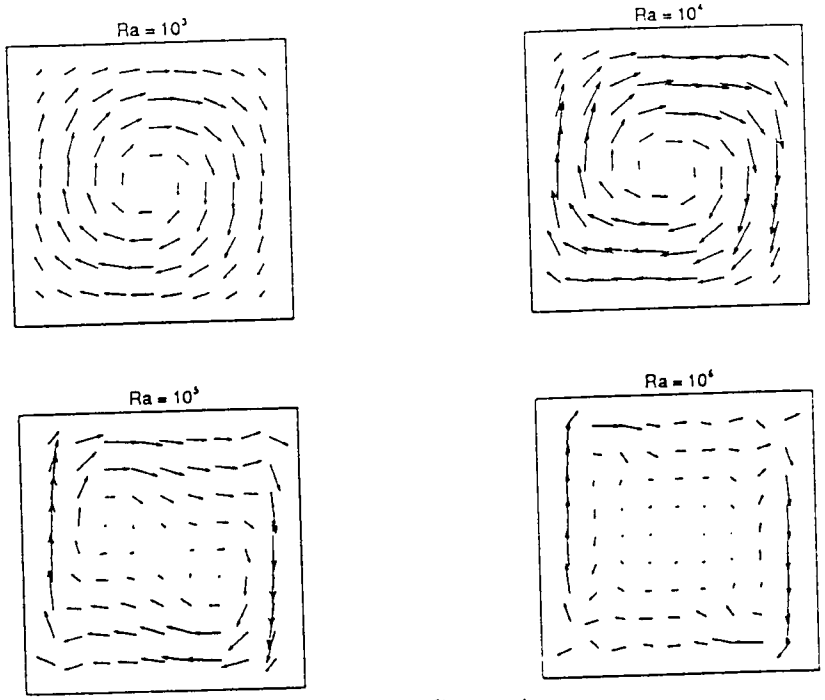
A). Continuity Constraint



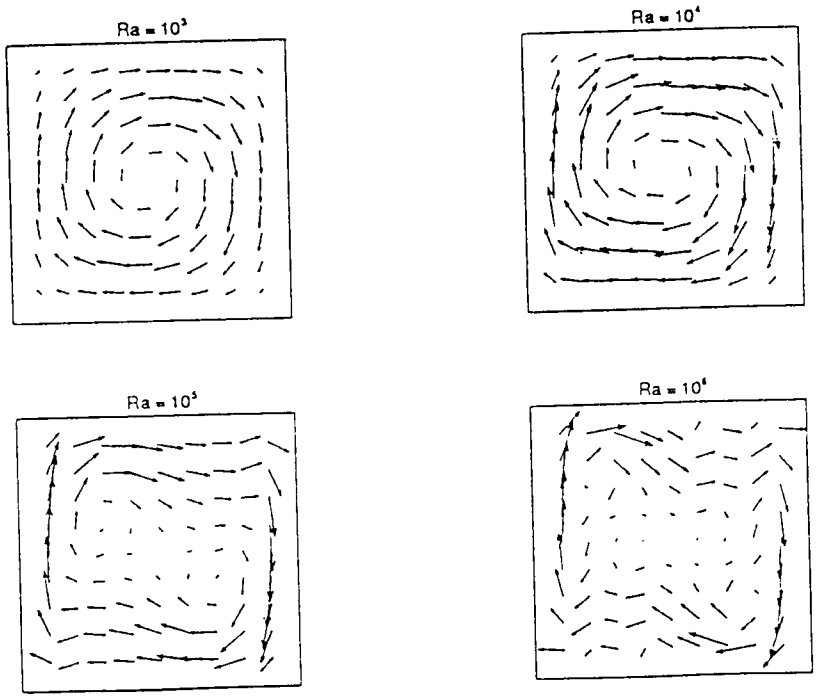
B). Vorticity-Streamfunction

Figure 12
Vorticity Contours

11X11 Uniform Mesh



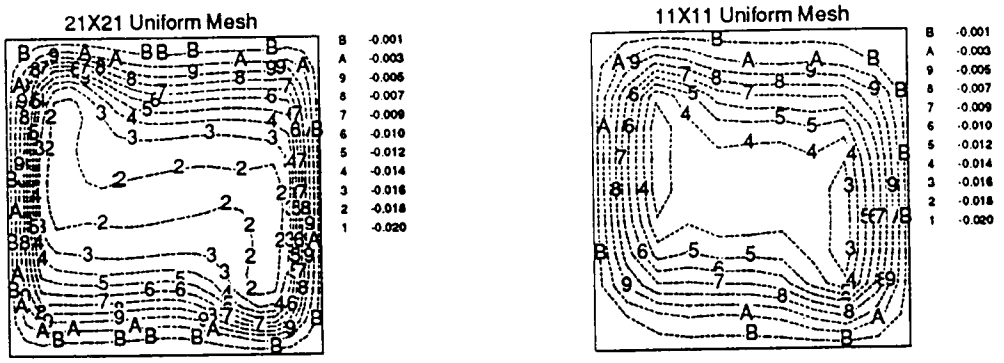
A). Continuity Constraint



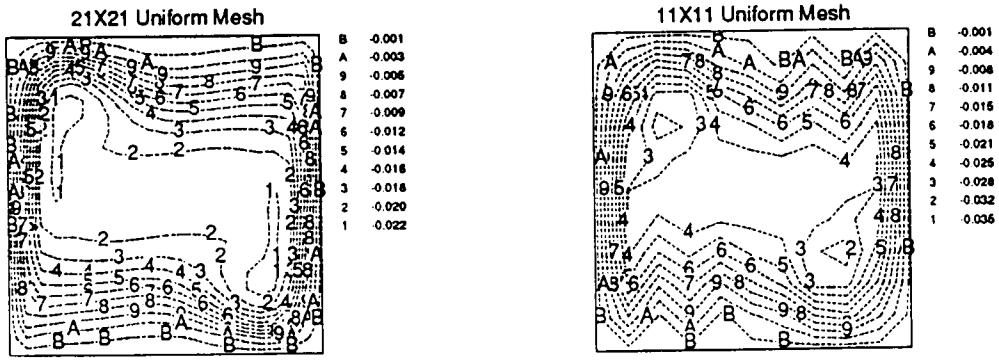
B). Vorticity-Streamfunction

Figure 13
Velocity Vectors

$Ra = 10^6$



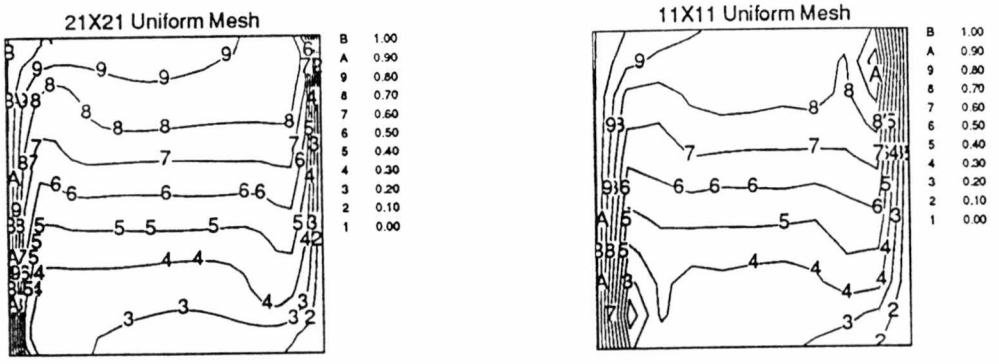
A). Continuity Constraint



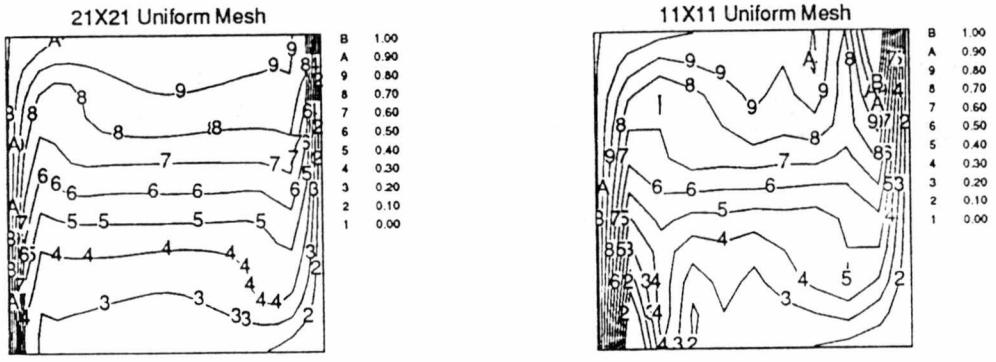
B). Vorticity-Streamfunction

Figure 14
Streamfunction Contours
Uniformly Refined Mesh

$\mathtt{Ra} = 10^6$



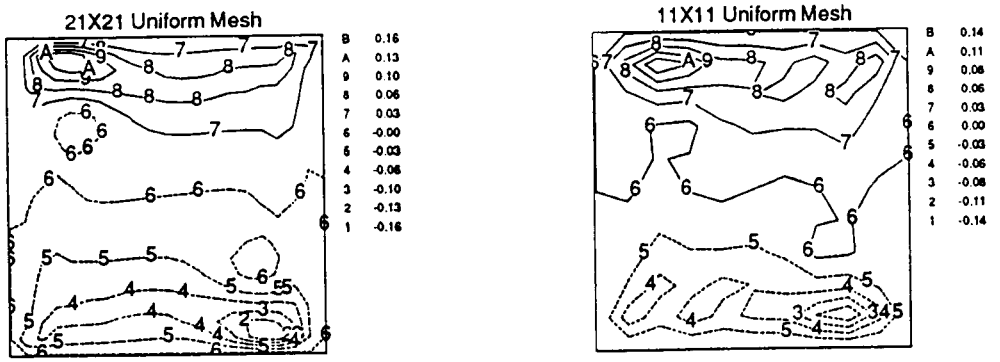
A). Continuity Constraint



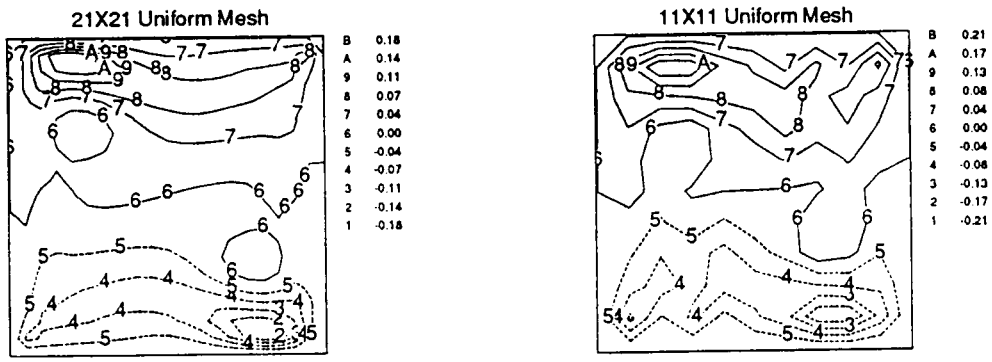
B). Vorticity-Streamfunction

Figure 15
Temperature Contours
Uniformly Refined Mesh

$Ra = 10^6$



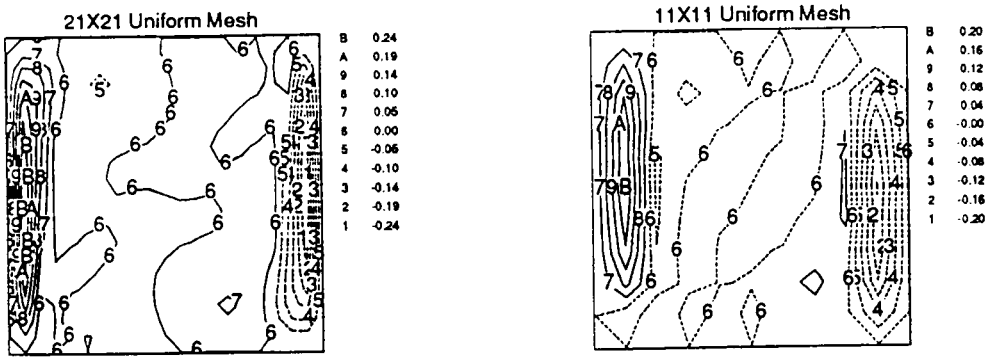
A). Continuity Constraint



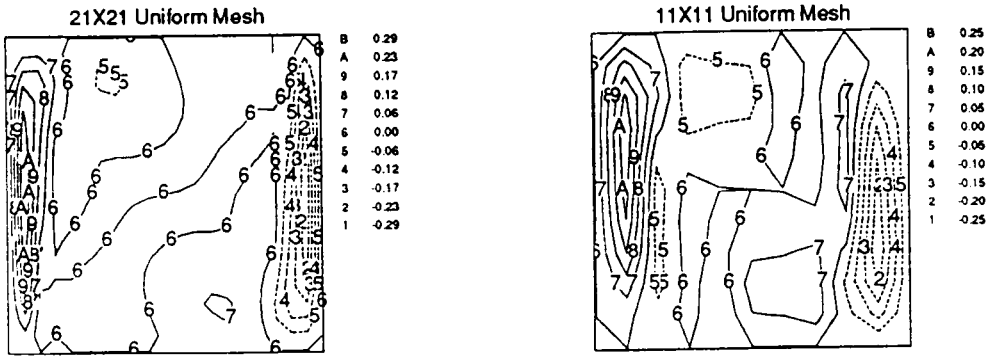
B). Vorticity-Streamfunction

Figure 16
U Velocity Contours
Uniformly Refined Mesh

$Ra = 10^6$



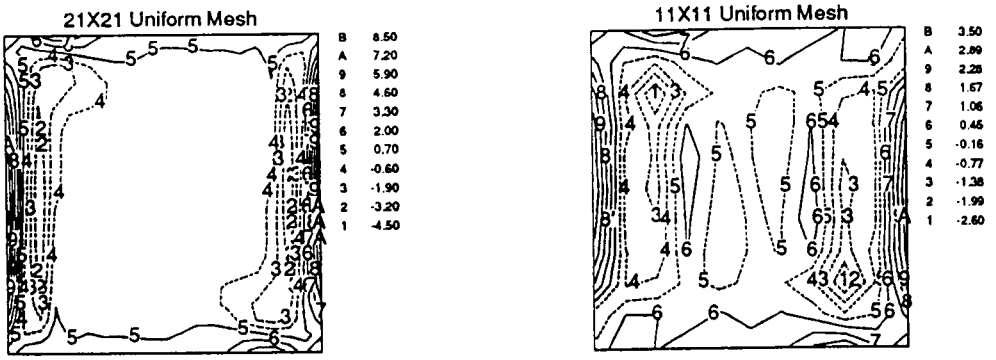
A). Continuity Constraint



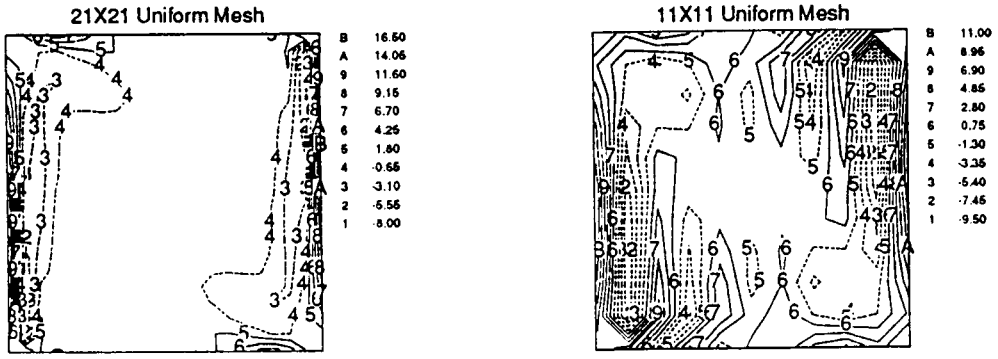
B). Vorticity-Streamfunction

Figure 17
V Velocity Contours
Uniformly Refined Mesh

$Ra = 10^6$



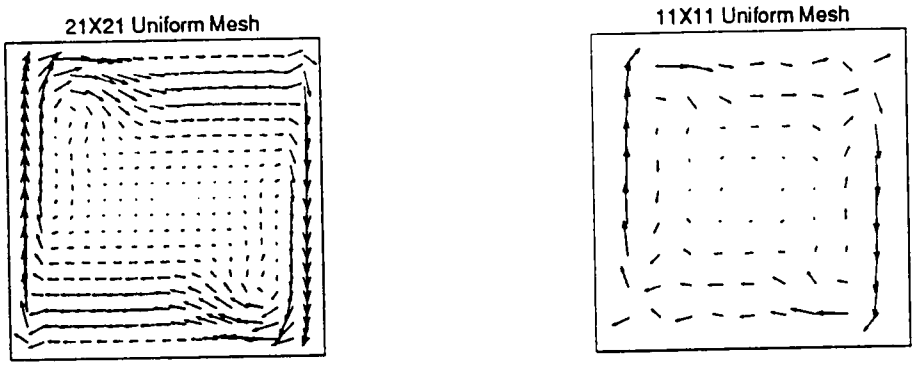
A). Continuity Constraint



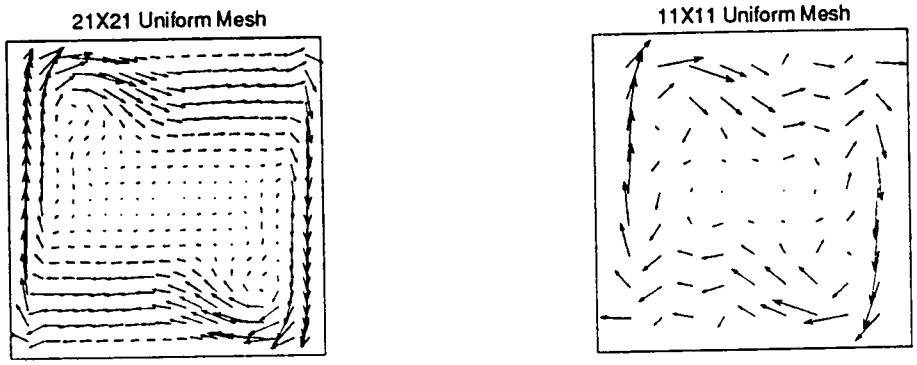
B). Vorticity-Streamfunction

Figure 18
Vorticity Contours
Uniformly Refined Mesh

$Ra = 10^6$



A). Continuity Constraint



B). Vorticity-Streamfunction

Figure 19
Velocity Vectors
Uniformly Refined Mesh

With the finite element method, there exists the capability to perform a local mesh adjustment/refinement in regions of sharp gradients without increasing the mesh nodalization which would require more computer resources. The solutions for $Ra=10^6$ on the 11x11 mesh showed the upper right hand and lower left hand corners the regions producing the solution oscillations. Figure 20 shows the locally adjusted non-uniform 11x11 mesh with modest refinement near the wall corners. Figures 21 through 25 directly compare solutions on the uniform and the locally refined mesh. The local refinement reduces the oscillations in the corners and improvess quality, but sacrifices the solution detail toward the center of the domain. This lack of detail is especially apparent in the velocity vector plots, Figure 26. Further mesh refinement toward the corners may have eliminated the oscillations completely, but would also have destroyed any detail in the center.

Another control for mesh scale oscillations is the use of artificial viscosity. On the final simulation sets, artificial viscosity in the form of equation (56) was added to assess dampening of the oscillations. Element average velocities, as given in Appendix I, are used in the matrix formulation of these terms. For the continuity constraint algorithm, a value of $\nu_q = 0.1$ was used for the Courant number term, equation (56), for both momentum and temperature. A final (very large) value of $\nu_q = 3.0$ was used in the vorticity-streamfunction formulation,

Figures 27 through 32 compare the results which shows the added dissipation is effective in damping the solution oscillations without eliminating the solution quality at $Ra=10^6$. These data confirm the use of artificial dissipation was more successful with the continuity constraint algorithm than with the vorticity formulation. The velocity vector distribution in Figure 32 show the solution oscillations along the wall boundaries and near corners are eliminated. The generated streamfunction contours from the continuity constraint velocity solution also agree significantly better with the de Vahl Davis results. The temperature contours show that more artificial viscosity may be required for thermal transport prediction, but further numerical dissipation may destroy the solution quality.

A higher value of ν_q was required for the vorticity solution for two reasons: 1). the dissipation terms are expressed in terms of velocity instead of streamfunction in the code, and 2). the mesh-scale oscillations

11X11 Mesh

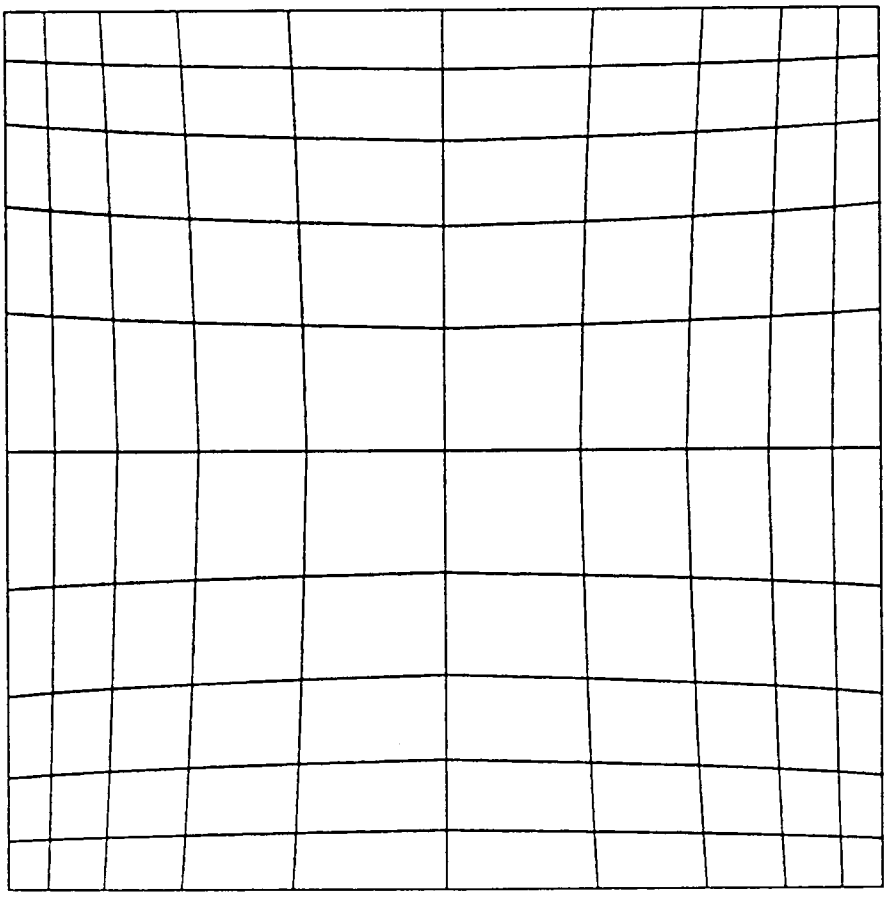
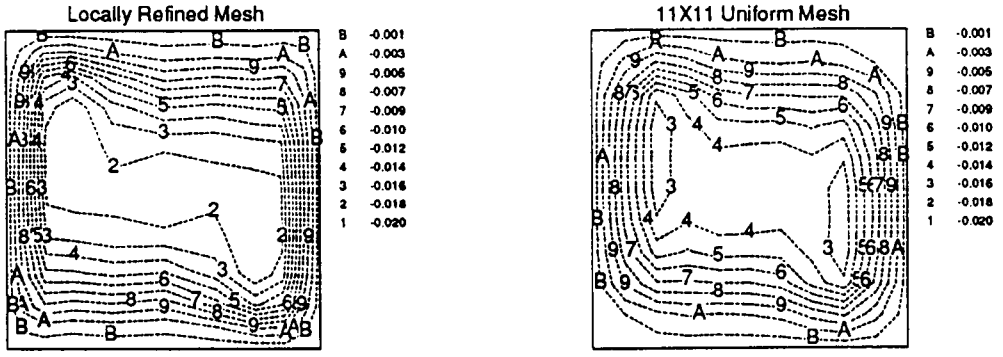
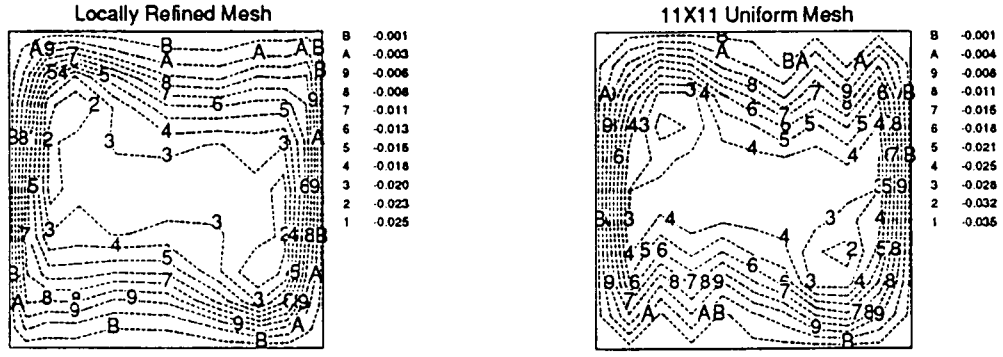


Figure 20
Locally Refined Mesh

$\mathrm{Ra} = 10^6$



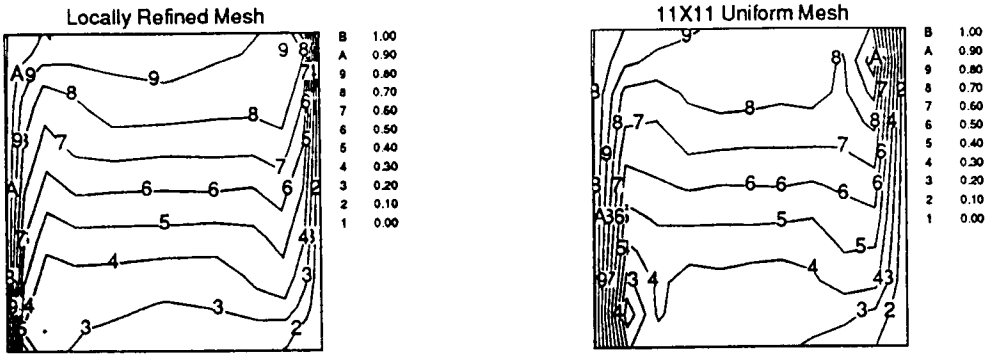
A). Continuity Constraint



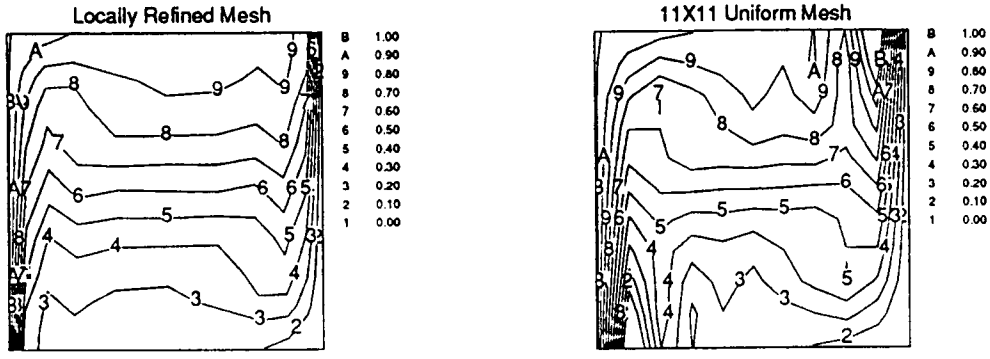
B). Vorticity-Streamfunction

Figure 21
Streamfunction Contours
Locally Refined Mesh

$Ra = 10^6$



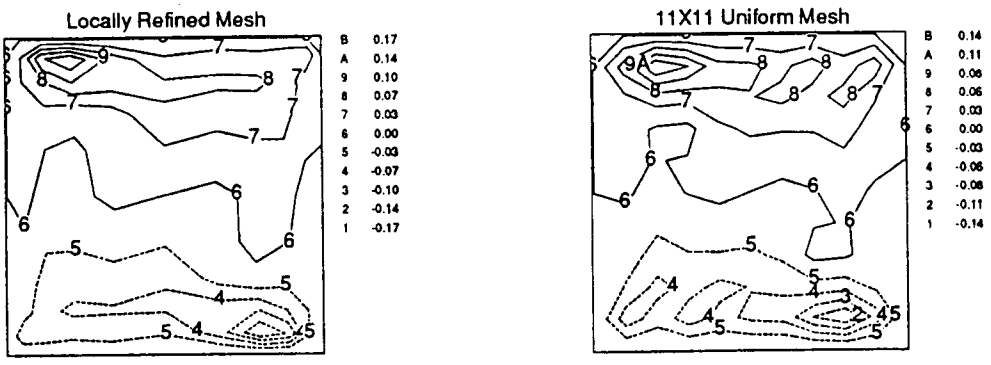
A). Continuity Constraint



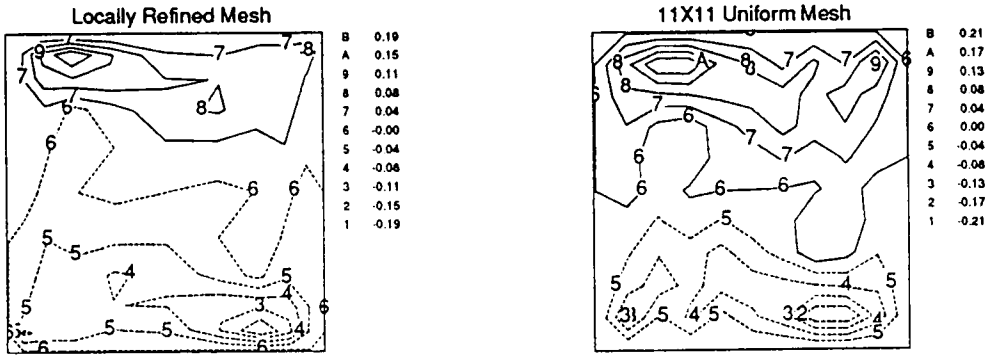
B). Vorticity-Streamfunction

Figure 22
Temperature Contours
Locally Refined Mesh

$Ra = 10^6$



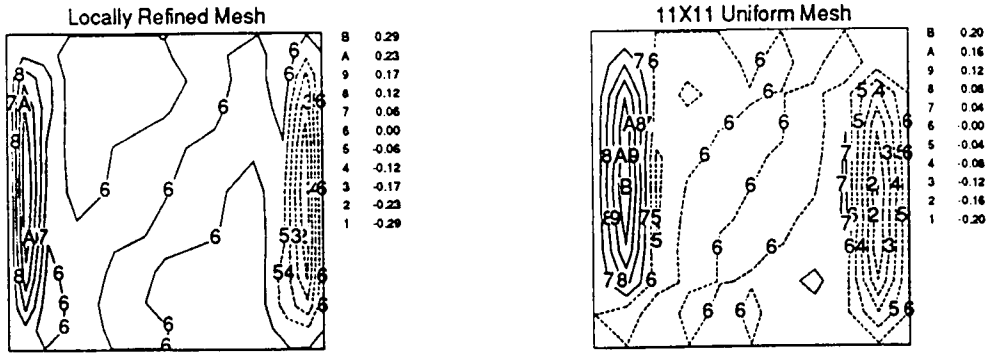
A). Continuity Constraint



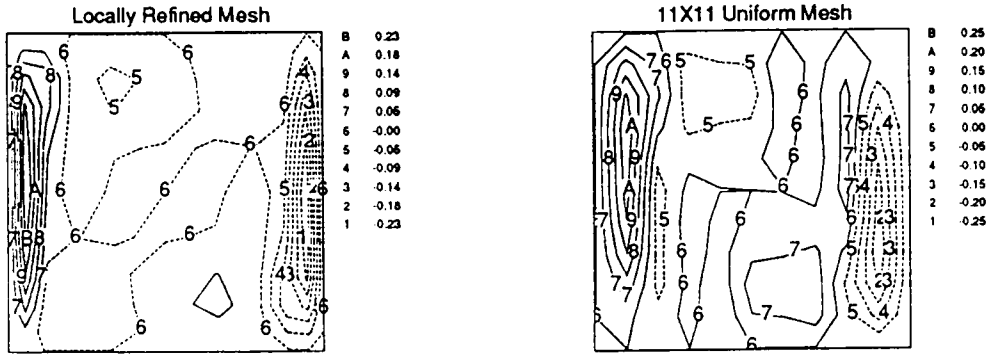
B). Vorticity-Streamfunction

Figure 23
U Velocity Contours
Locallyly Refined Mesh

$Ra = 10^6$



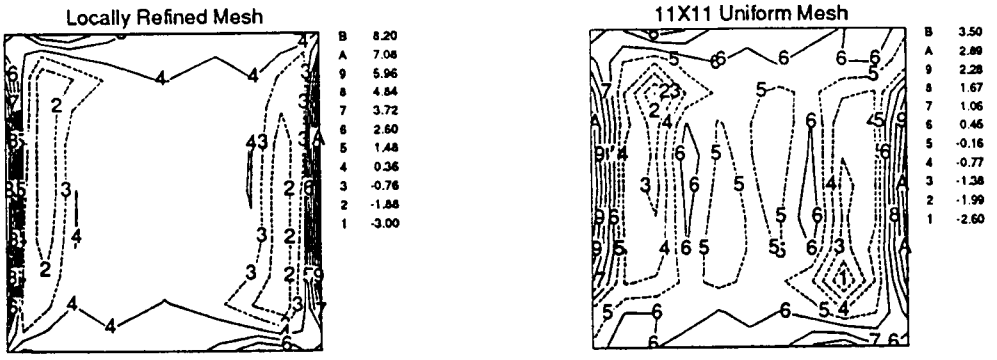
A). Continuity Constraint



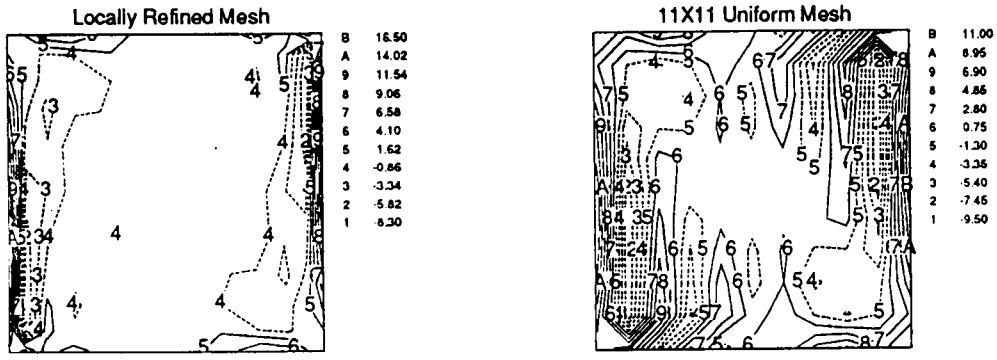
B). Vorticity-Streamfunction

Figure 24
V Velocity Contours
Locally Refined Mesh

$Ra = 10^6$



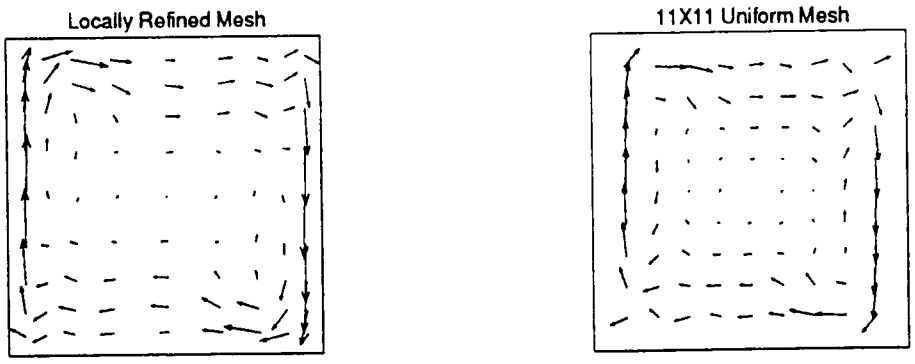
A). Continuity Constraint



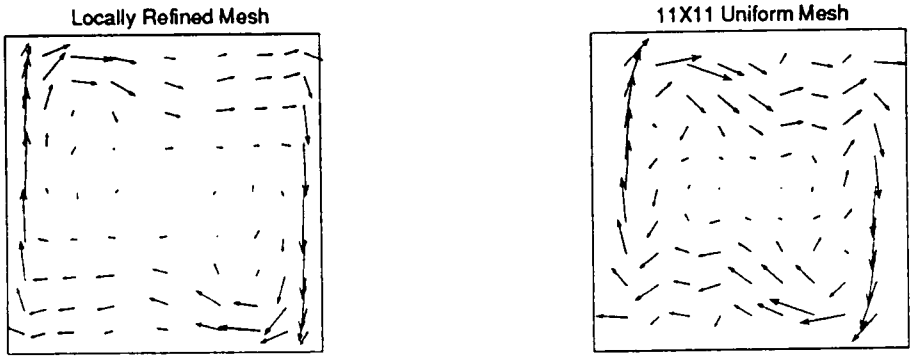
B). Vorticity-Streamfunction

Figure 25
Vorticity Contours
Locally Refined Mesh

$Ra = 10^6$



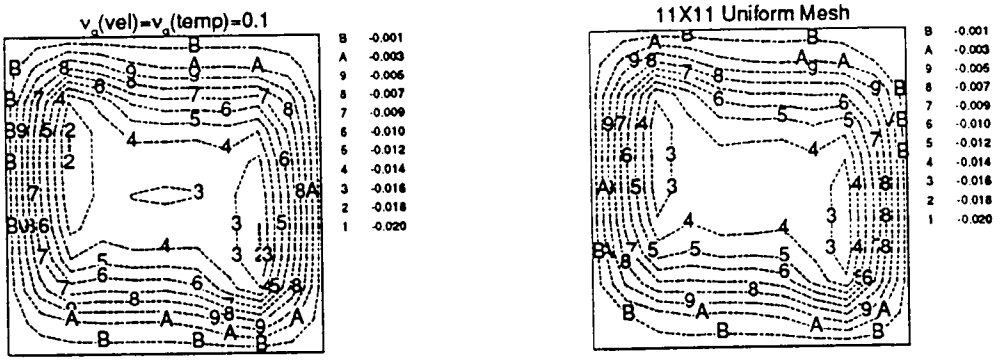
A). Continuity Constraint



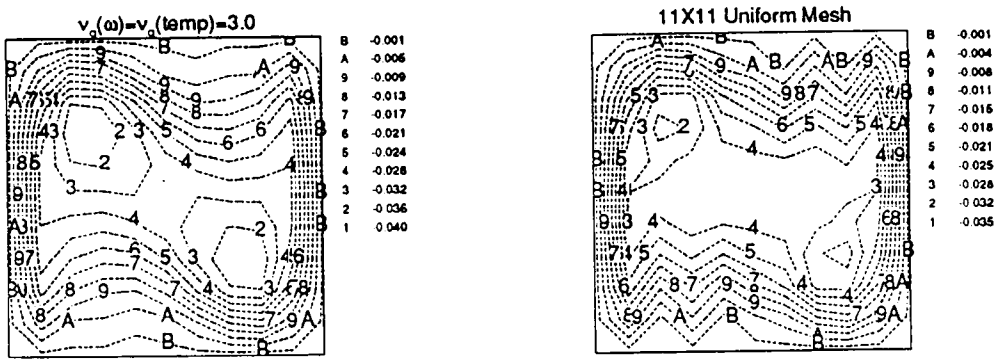
B). Vorticity-Streamfunction

Figure 26
Velocity Vectors
Locally Refined Mesh

$Ra = 10^6$



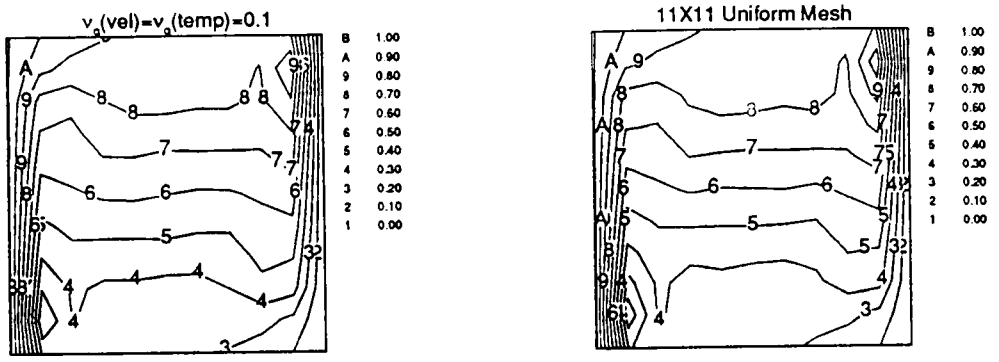
A). Continuity Constraint



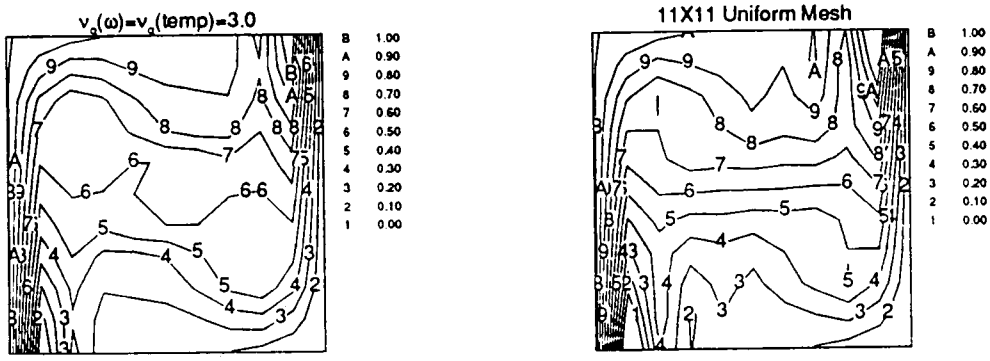
B). Vorticity-Streamfunction

Figure 27
Streamfunction Contours
Artificial Viscosity

$Ra = 10^6$



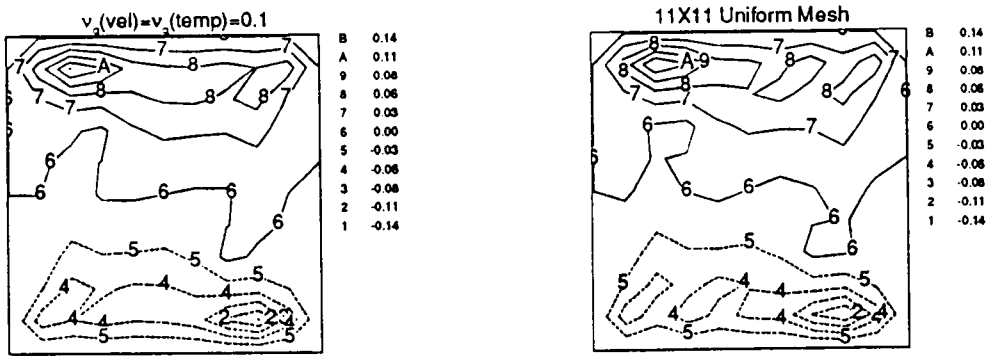
A). Continuity Constraint



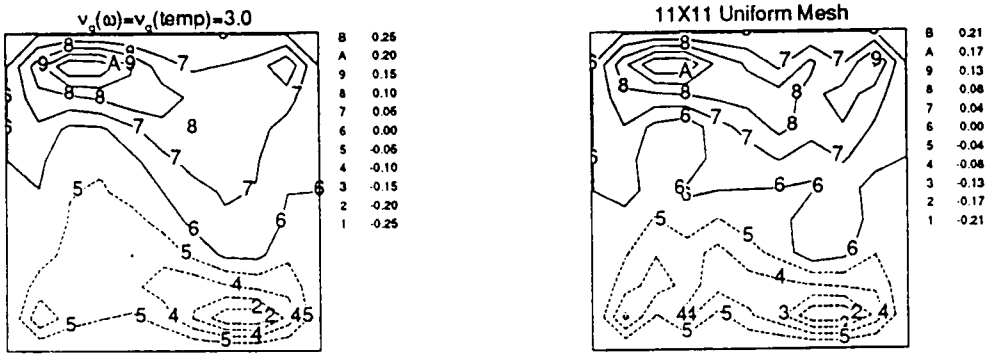
B). Vorticity-Streamfunction

Figure 28
Temperature Contours
Artificial Viscosity

$Ra = 10^6$



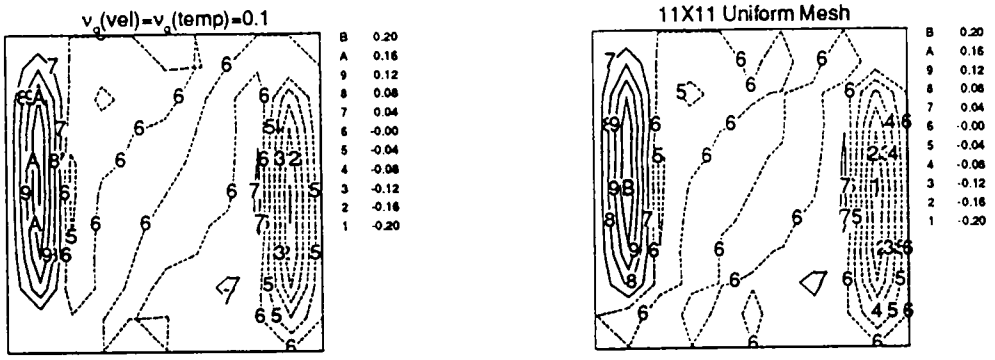
A). Continuity Constraint



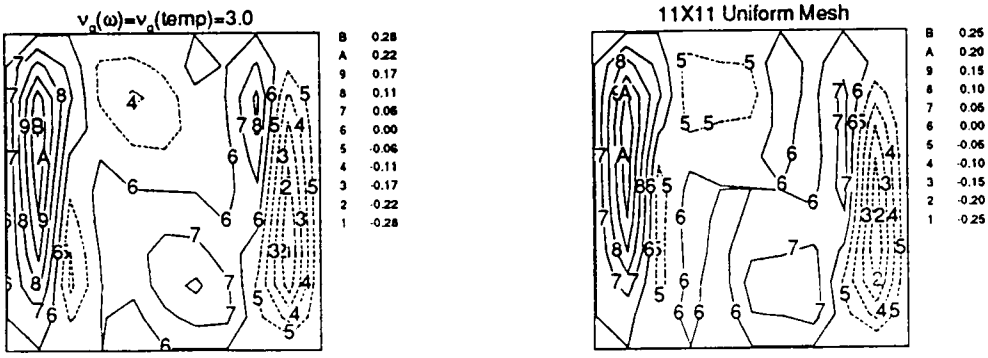
B). Vorticity-Streamfunction

Figure 29
U Velocity Contours
Artificial Viscosity

$Ra = 10^6$



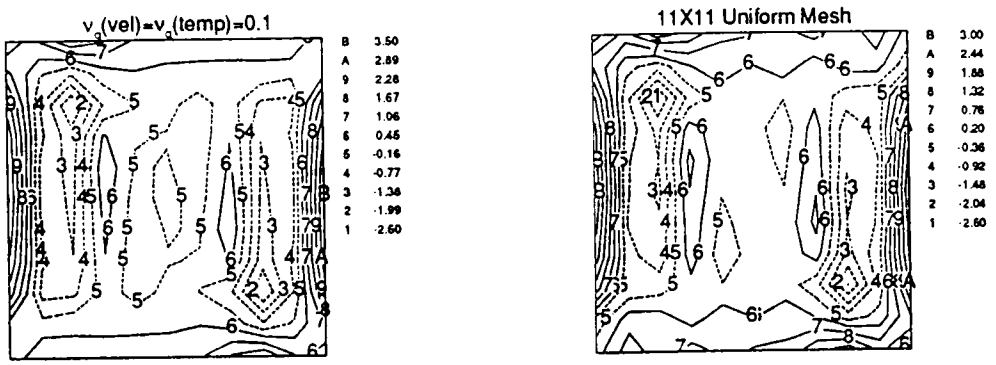
A). Continuity Constraint



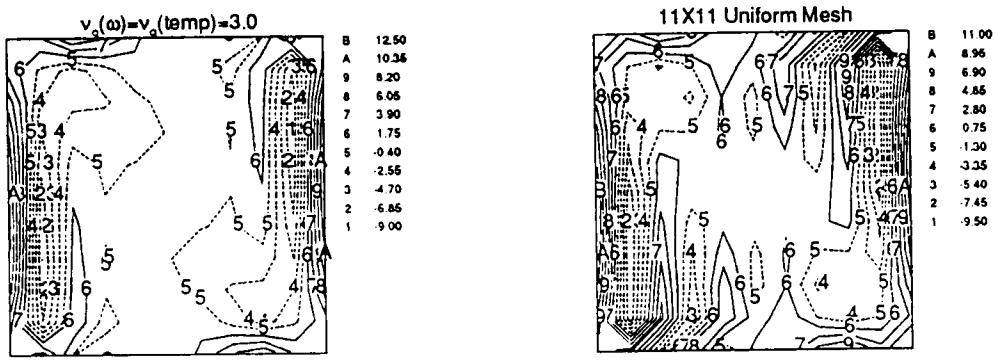
B). Vorticity-Streamfunction

Figure 30
V Velocity Contours
Artificial Viscosity

$Ra = 10^6$



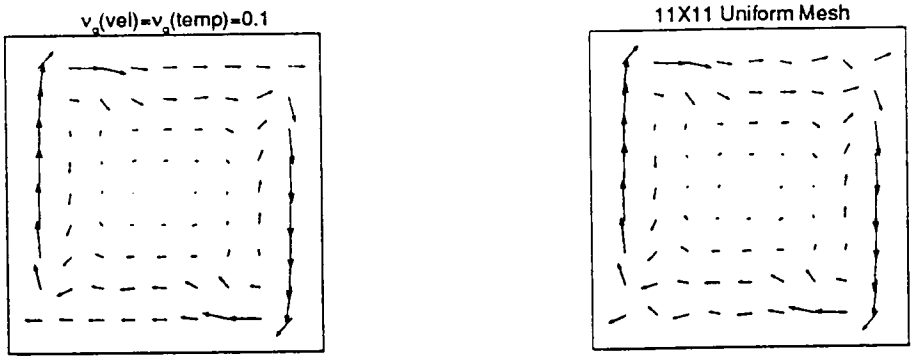
A). Continuity Constraint



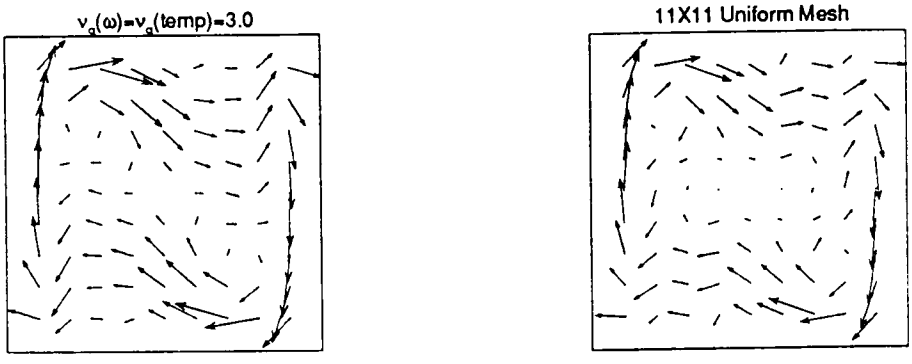
B). Vorticity-Streamfunction

Figure 31
Vorticity Contours
Artificial Viscosity

Ra = 10^6



A). Continuity Constraint



B). Vorticity-Streamfunction

Figure 32
Velocity Vectors
Artificial Viscosity

are more severe with the vorticity formulation. Expressing the artificial viscosity terms in the form of streamfunction instead of velocity forms very complex, 2nd-degree hyper-matrices, which have been avoided in this project.

Isothermal step-wall diffuser

The step-wall problem falls into the class of constrained internal flows, where the flow enters and exits the solution domain. Problems of this class require application of outflow boundary conditions, where the state variables must leave the domain without disturbing the upstream flow. The expansion immediately after the step also produces a complex flow field with multiple recirculation regions as a function of Reynolds number. The complexity of the flow field in combination with an outflow boundary makes this problem an excellent benchmark test for the continuity constraint CFD algorithm.

Experimental data for the isothermal step-wall problem is provided by Armaly et al [9] to verify the general character of the simulation flow field. Figure 33 presents the domain description and boundary conditions used in the simulations for the isothermal step-wall. Fully developed duct flow is the specified (Dirichlet) condition for inflow velocity. A reference length of 0.104cm (3.41×10^{-3} ft), the supply duct hydraulic diameter, is used in obtaining the normalized coordinates given in Figure 33. The reference velocity is then determined from the reference length and Reynolds number, i.e., U=Rev/L.

Computations are performed on the meshing given in Figure 34. A uniform mesh in the transverse direction is used on the inlet plane with refinement toward the walls and step corner. For assessing round-off error processes, the entire problem domain is rotated 30^{o} in the counter-clockwise direction. The rotation of the mesh eliminates two problems: 1). requires specification of Dirichlet data for the v velocity component on the inlet, and 2). eliminates round-off error in the v velocity computations within the supply duct due to constraining a zero v velocity on the inlet.

Steady-state is assumed to be achieved when various energy norms stabalize (Appendix III). A stable pressure norm was selected for determing the converged steady-state solution, since the pressure is evaluated intermittently during the time integration and not involved with the iterative process as with the velocity and continuity costraint. The pressure was updated every three time steps to prevent continuity

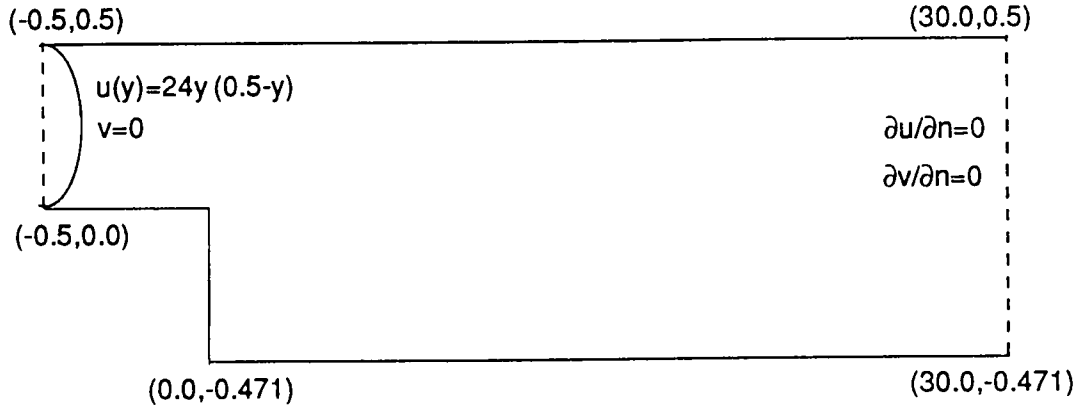


Figure 33
Boundary Conditions for Step-Wall Diffuser Problem

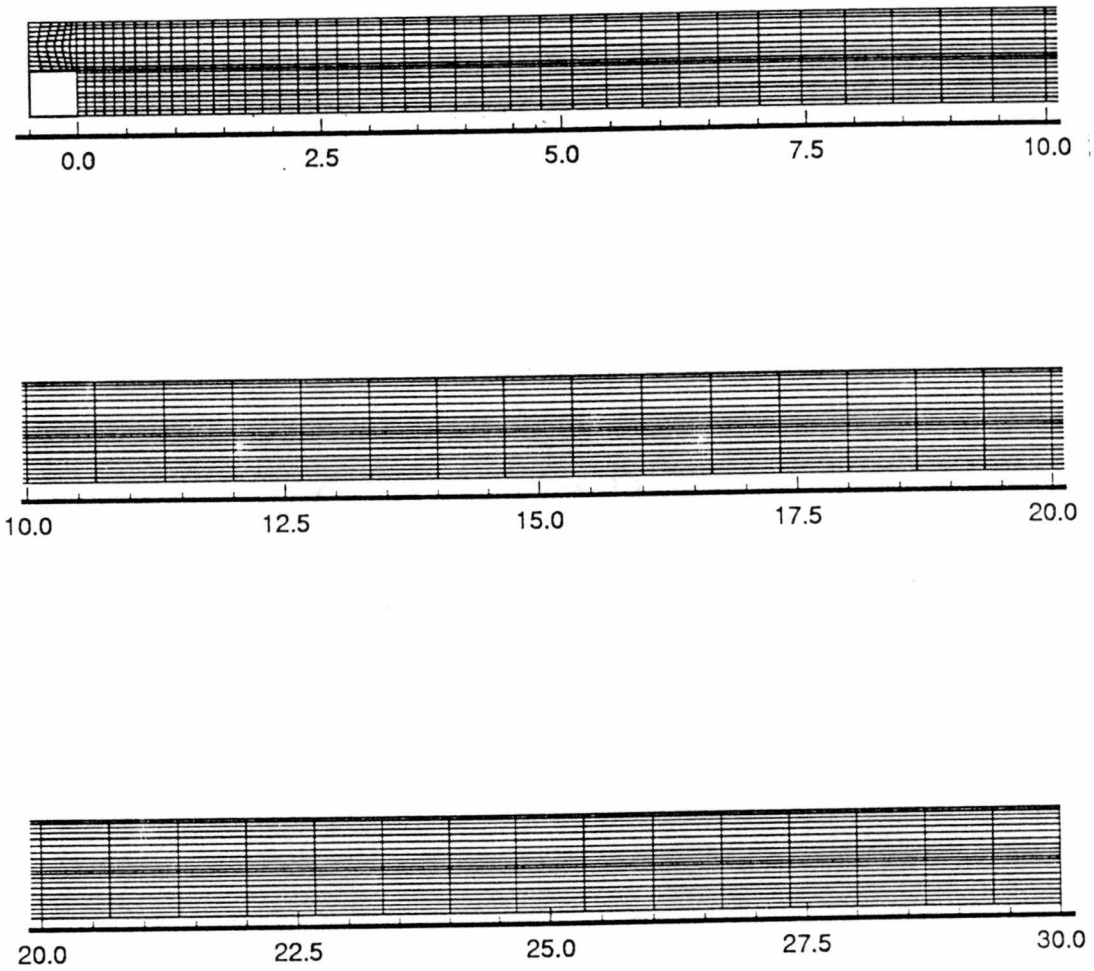


Figure 34
Finite Element Mesh for Step-Wall Diffuser

error from swamping the solution. In the simulations, the algorithm required application of artificial viscosity to eliminate pressure field dispersion-induced errors in the inlet flow region. For simulation verification, the reattachment and detachment locations of the continuity constraint algorithm will be compared with Armaly's results. Figure 35 is an excerpt from the Armaly paper graphing measured detachment and reattachment locations of all seperation regions.

Figure 36 compares the pressure contours for Re = 400 with no artificial viscosity and with $\nu_q = 0.05$ (refer to equation (17)). With no artificial dissipation, some pressure contours show significant oscillations, as induced by the dispersive error mode in the velocity field. A small level of artificial viscosity ($\nu_q = 0.05$) reduces the oscillation magnitude to negligible, as confirmed in the bottom figure. Figure 37 shows the corresponding velocity vector plots with the zero vorticity contour superimposed on the field for identifying the point of reattachment for the bottom recirculation region. Without artificial viscosity, the perturbations produced at the inlet destroy the solution quality to the point where the reattachment point falls considerably short of the predicted position. The bottom figure with $\nu_q = 0.05$ demonstrates that the artificial dissipation enhances solution quality without compromising accuracy as measured by the location of the reattachment point.

Figures 38 shows the simulation results for Re=600 and the various artificial viscosity levels of ν_q = 0.05, 0.1, and 0.15. The Armaly attachment experimental results data are listed above the inlet in the top figure. Only at the highest artificial viscosity of 0.15 was a stable pressure norm obtained. For the lower artificial viscosity levels, the pressure norm did not reach a stable value. The figures contain the time point at which the calculations are halted. At the given times steps, the difference between the pressure norms at consecutive pressure updates reached a minimal value. The results show that the increase in artificial viscosity had minimal impact on the location of the reattachment point for the bottom recirculation point or the detachment point of the top recirculation regions. The effect of artificial viscosity is most notable on the length of the top recirculation region, where Armaly gives a length of 2.5. The interpolated lengths for the continuity constraint results are 3, 3.7, and 4.1 for $\nu_q = 0.05$, 0.1, and 0.15, respectively.

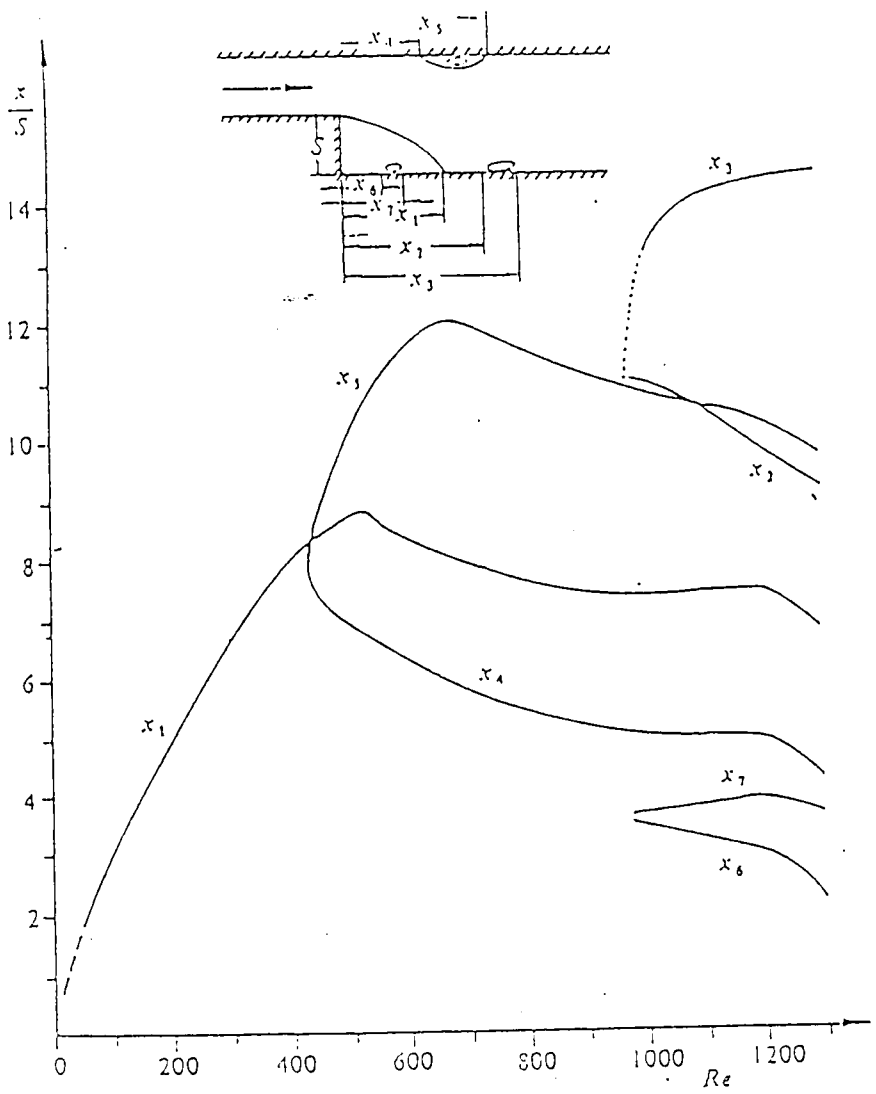


Figure 35
Armaly
Predicted Locations of Flow Detachment and Reattachment
as a Function of Reynolds Number

Re = 400

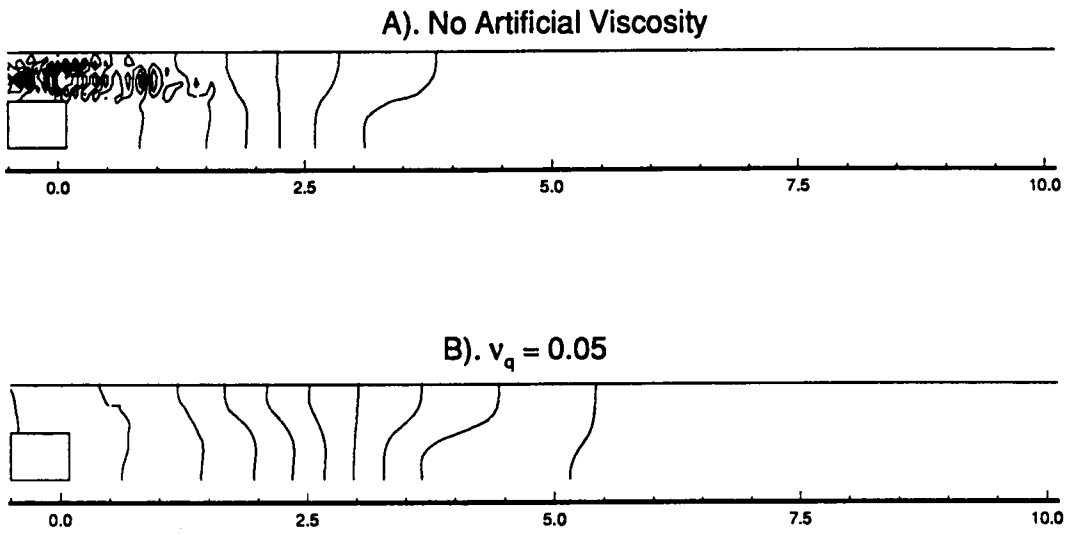


Figure 36
Pressure Contours

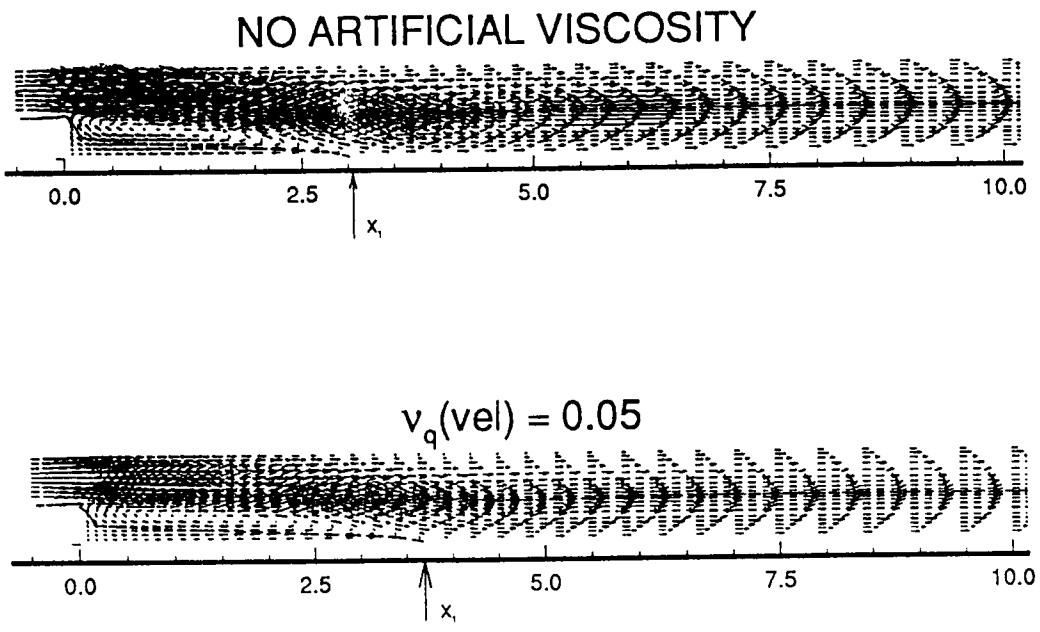


Figure 37
Velocity Vectors

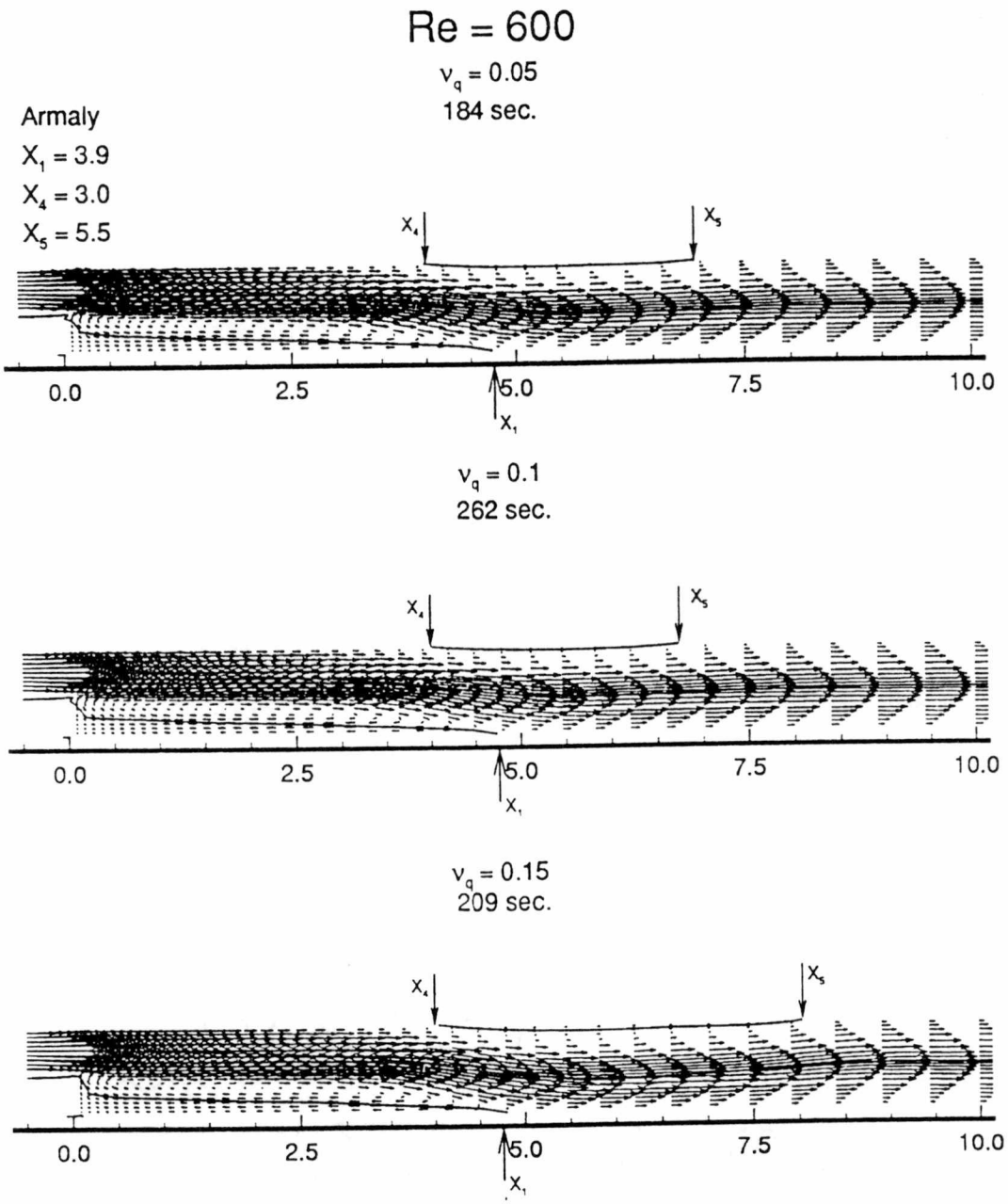


Figure 38
Velocity Vectors

The discrepancy in the location of the recirculation region with the Armaly results is attributed to the three-dimensional character of the flow. Armaly indicates for Re>420, the flow is not two-dimensional with cross-flow effects from the retaining wall influencing the centerline where measurements are taken. In addition, computational experiments performed by Williams [13] for three dimensional simulations of the step-wall diffuser support the three dimensional character of the flow, where in William's results, the eddies formed at the retaining wall perturb the flow up to the centerline of the duct. Furthermore, the mesh is fairly coarse at the point of reattachment of the top recirculation region resulting in inconsistency of locating the point of the zero vorticity contour.

The results of two-dimensional simulations at Re=600 and higher Reynolds number, cannot accurately be compared with the Armaly data since the flow is actually three-dimensional. Alternatively, the results at Re=800 can be compared with Gartling's benchmark CFD results [11]. Gartling performed a mesh refinement study on the step-wall diffuser with meshes ranging from 6x120 to 40x800. Gartling's geometry did not contain the inflow diffuser region, but placed the fully developed velocity profile directly above the step. In addition, the step height was a non-dimensional 0.5 instead of 0.471.

A value of $\nu_q = 0.15$ is used for the artificial viscosity to provide appropriate numerical damping for the Reynolds number 800 simulation. A converged pressure norm was not obtained with the continuity constraint simulations, indicating the problem may actually be unsteady. The simulations were stopped when consecutive pressure norm changes remained below 10^{-8} requiring 300 times steps. Figure 39 compares the continuity constraint solution with Gartling's coarsest mesh results for attachment points listed above the inlet. The location of the bottom reattachment point and the top detachment point are modestly less than what Gartling obtained. Some of the discrepancy is attributed to the lack of a supply diffuser in Gartling's simulations, where Armaly indicates the expansion immediately after the step does perturb the flow within the inlet region. Gartling obtained a length of 5.69 for the top recirculation bubble, whereas a length of 4.8 was obtained with the continuity constraint simulation on this mesh.

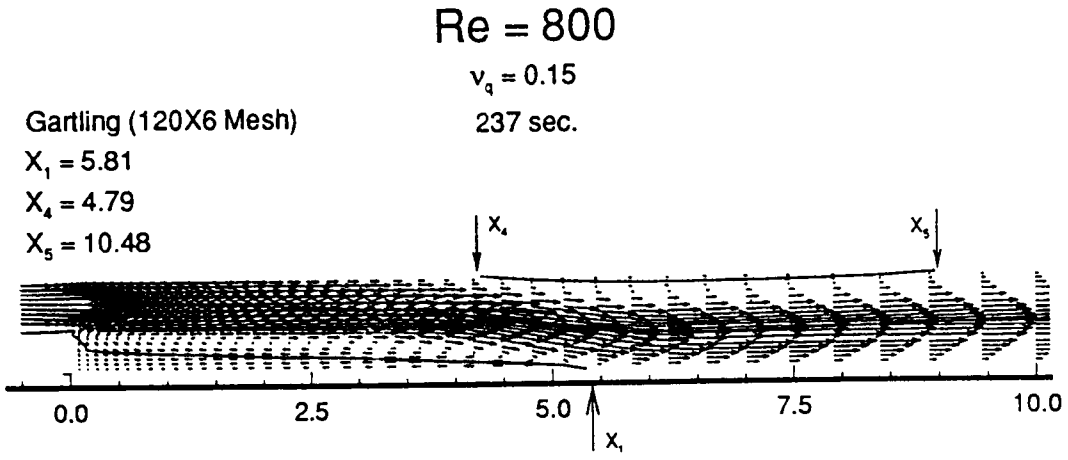


Figure 39
Velocity Vectors

ASME WAM Session Heat Transfer Benchmark Problem

This benchmark heat transfer problem developed by the K-12 committee of the ASME for the evaluation of heat transfer codes is flow in a step-wall diffuser with a constant heat flux applied along the upper and lower walls immediately downstream of the step. The step-wall lies in the horizontal plane, thus decoupling the velocity from temperature solution process.

The velocity field is described by Gartling's simulation [11]. In addition to the parabolic inlet profile for velocity, a temperature Dirichlet constraint on temperature is applied at the inlet corresponding to fully developed duct flow [17]. Figure 40 shows a sketch of the domain and the boundary conditions for this problem. The wall and outflow boundary conditions for velocity are the same as for the isothermal case, Figure 33. Two outflow boundary conditions can be used for temperature; (1) a homogeneous Neumann condition, and an (2) efflux condition. The efflux boundary condition allows any temperature flux through the outflow boundary if the flux is not homogeneous (fully developed). The non-dimensional heat flux applied at the walls is

$$q' = -\frac{1}{Pe}\frac{\partial \Theta}{\partial y} = -\frac{1}{Pe}\left(\frac{32}{5}\right) \tag{62}$$

where heat is extracted from the fluid in the duct. From the heat flux, the Nusselt number along the upper and lower walls can be evaluated directly as

$$Nu_x = \pm\frac{2}{\Theta_w - \Theta_b}\frac{\partial \Theta}{\partial y}\bigg|_{y=0,1} = \pm\frac{2}{\Theta_w - \Theta_b}\left(\frac{32}{5}\right) \tag{63}$$

where Θ_b is the non-dimensional bulk temperature along the duct is

(64)

$$\Theta_b(x) = \frac{\int_{-0.5}^{0,5} u(y)\Theta(y)dy}{\int_{-0.5}^{0.5} u(y)dy}$$

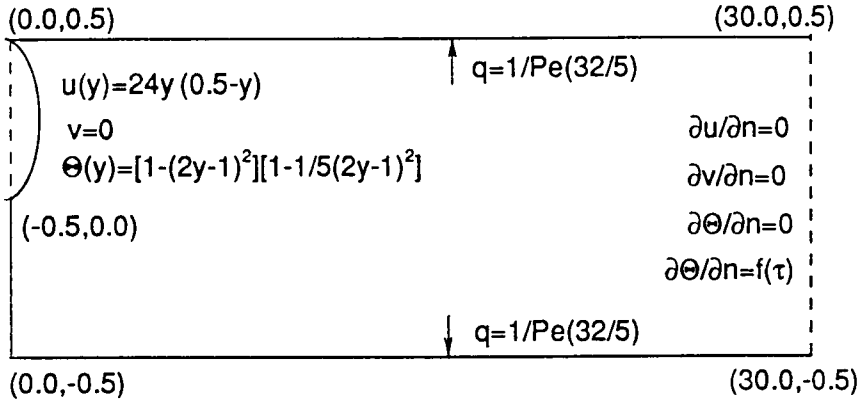


Figure 40
Boundary Conditions for Step-Wall Diffuser,Heat Transfer Problem

The Reynolds number of the problem is 800 giving a Peclet number of 544 for a Prandtl number of 0.68 for air at 70°F. The same reference values for the isothermal problem are applied with the reference length of 3.41×10^{-3} ft. giving a reference velocity of 37.3 ft/sec. Since the hydrodynamics is decoupled from the temperature field, the reference temperature and expected temperature change are arbitrarily selected. A reference temperature of 70° F corresponding to the fluid properties of air is applied in the simulations with an expected temperature change of 100° F.

Figure 41 shows the mesh on which the simulations are performed with refinement near the duct walls and the step. For this simulation, the vorticity-stream function formulation was used to obtain the steady-state velocity field, which is then used in solving the decoupled energy equation. Figure 42 shows the resultant isothermal velocity field with the zero vorticity contour superimposed for identifying the recirculation regions, for comparison with Gartlting's' coarsest mesh results given above the figure. These results agree very well with the Gartling data, while the modest discrepancies can be attributed to the relatively coarse (axial) mesh in these regions. The reattachment point of the bottom recirculation bubble obtained with the vorticity-streamfunction formulation is approximately 5.8. The top recirculation point detaches at 4.7 and reattaches at 10.4 giving a length of 5.7, where Gartling obtained a length of 5.69.

Figure 43 graphs the temperature contours for the entire domain, and clearly shows the inverse thermal boundary layer still developing at the outflow plane. The lack of solution oscillations reflecting from the outflow boundary may also indicate a homogenous Neumann outflow condition is valid for the problem even though the thermal boundary layer is still developing. Figure 44 gives the temperature profiles along the duct walls showing the temperature decreases toward the outflow boundary, as the wall temperatures approach the same level. Figure 45 shows the Nusselt number calculations along the upper and lower walls, where Karac [18] gives a solution of 8.23 for a fully developed flow Nusselt number for a uniform heat flux in a channel. The present values obtained are 8.34 at the top wall ,and 8.20 on the bottom wall, giving an average value of 8.27, in excellent agreement.

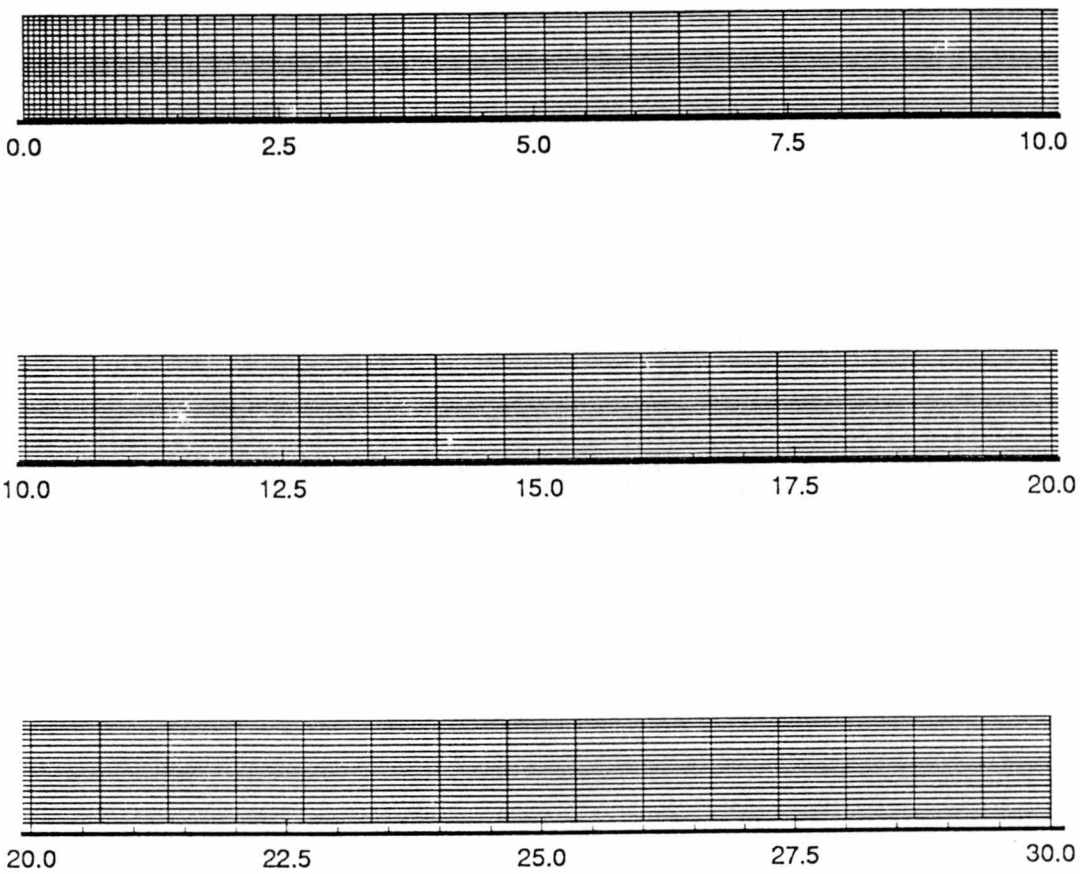


Figure 41
Finite Element Mesh: Gartling's Geometry

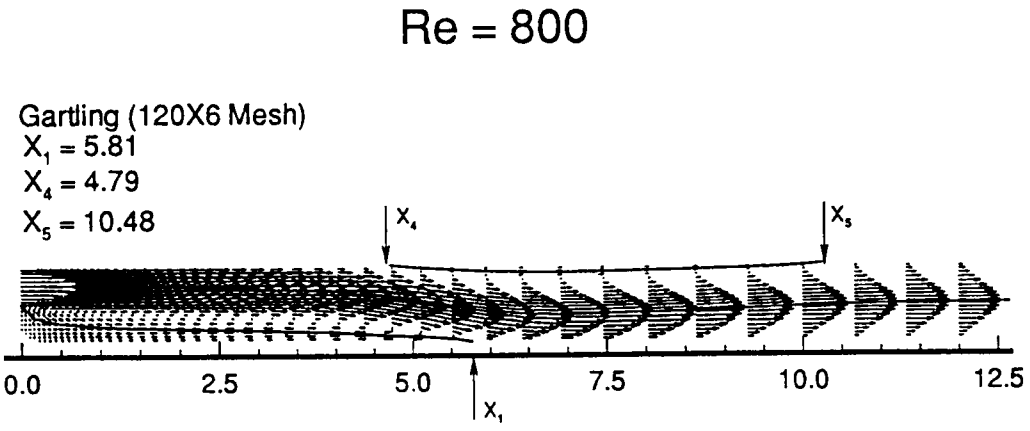


Figure 42
Velocity Vectors
Heat Transfer Benchmark Problem

Pe = 544

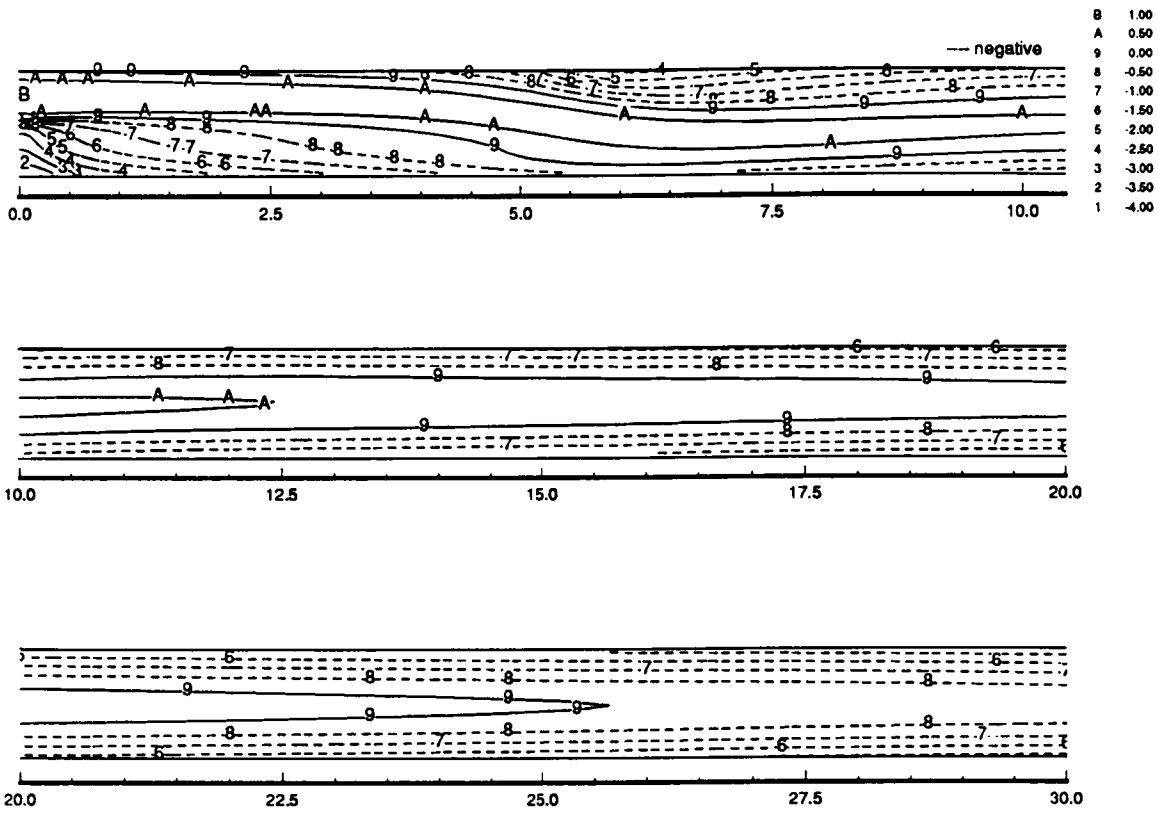


Figure 43
Temperature Contours
Homogeneous Neumann Outflow

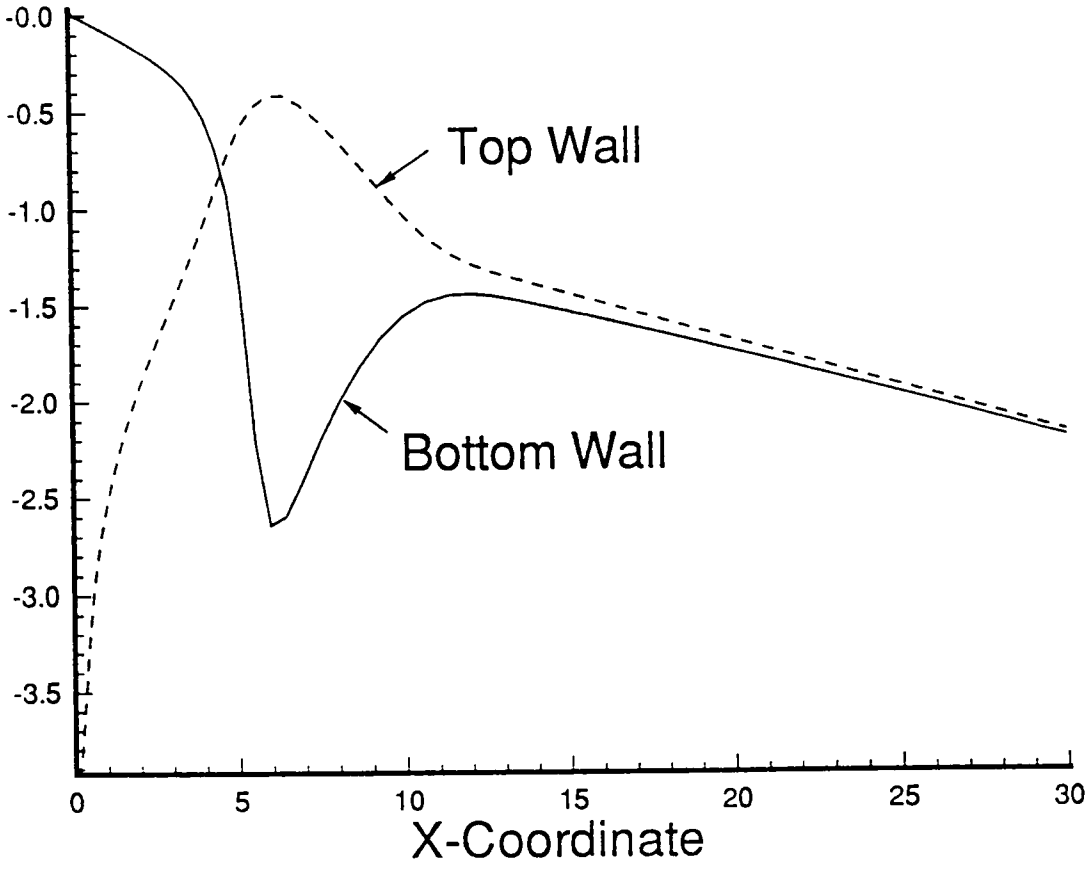


Figure 44
Temperature Profile Along Duct Walls

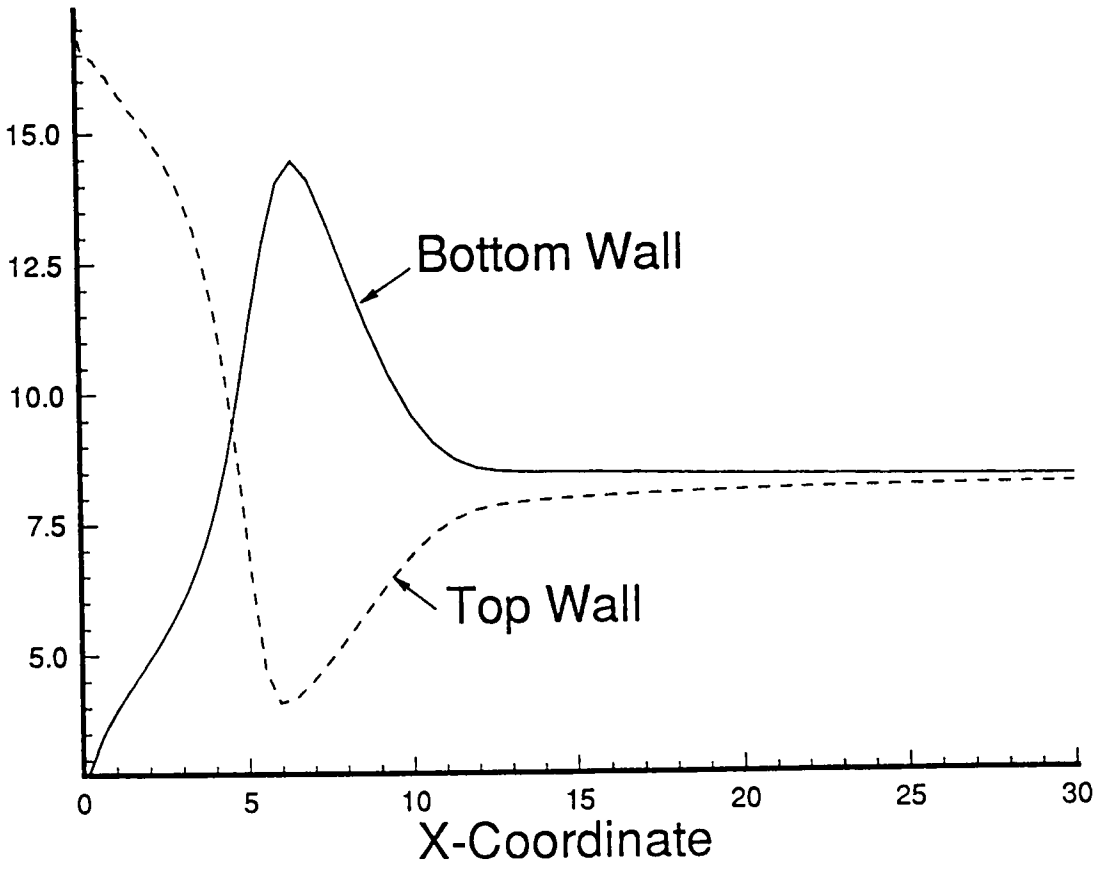


Figure 45
Nusselt Number Along Duct Walls

Room air motion simulation

The benchmark cases presented demonstrate the capabilities of the continuity constraint algorithm, and selected use of artificial viscosity for obtaining an oscillation-free accurate solution. These results give confidence to the main purpose of the work which is the simulation of 2-D room air motion. The generated CFD simulation results are compared with experimental data obtained at the University of Illinois/Urbana-Champagne and reported by Zhang, et al [15]. Experimental data on select distribution of velocity (actually speed), turbulent kinetic energy, and temperature were obtained for an isothermal case and a non-isothermal case with a heated floor. Figure 46 illustrates the room geometry the location of experimental measurements, as reported in Zhang's draft ASHRAE paper, a dissertation condensation.

The experimental tests were performed at a Reynolds number of 5735 based on the average inlet velocity of 5.88 ft/sec and the supply duct width of 2 inches. At this Reynolds number and with a short supply duct, only very modest turbulent phenomena is expected and most likely restricted to the supply diffuser region. Therefore, the simulations presented are performed using the simplest turbulence closure model (a constant, uniform Re^t). Figures 47 and 48 shows the distribution of the turbulent kinetic energy measured by Zhang for the isothermal and non-isothermal test cases, respectfully, where the turbulent kinetic energy is a characteristic parameter of turbulent phenomena [1,pp. 20,21]. The diffuser jet region is the only area containing non-negligible turbulence phenomena for both test cases, with some added turbulence generated by buoyancy effects within the floor region for the non-isothermal case. Based on the visual scale of turbulent kinetic energy in the diffuser jet region, an effective Reynolds number of 1000, corresponding to a constant turbulent Reynolds number of 5, is selected for the CFD simulations. The turbulent Reynolds number of 5 should capture the essence of dissipative effects of turbulence in the diffuser jet region, but not overwhelm the convected character of the flow elsewhere in the room.

The base room geometry, results of previous computational experiments using the continuity constraint pilot code, and the results of the benchmark problems were used in establishing a suitable mesh for the simulations, Figure 49. The supply diffuser meshing is based on the step-wall simulations, where the expansion at the wall plane certainly perturbs the flow entering the region. In addition, the wall juncture

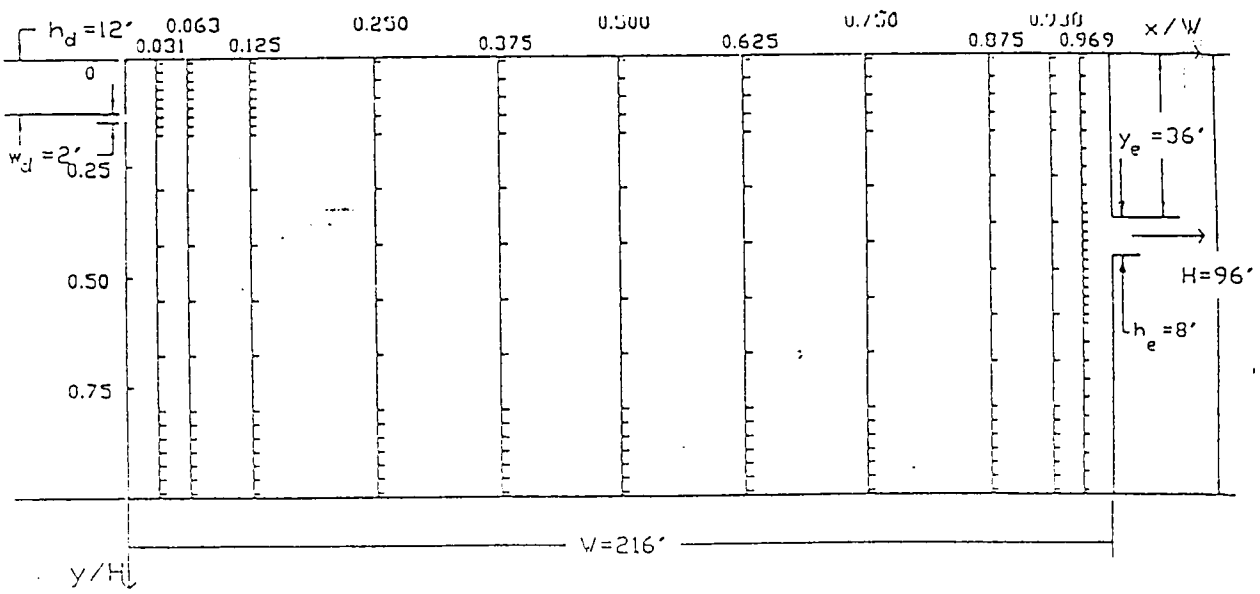
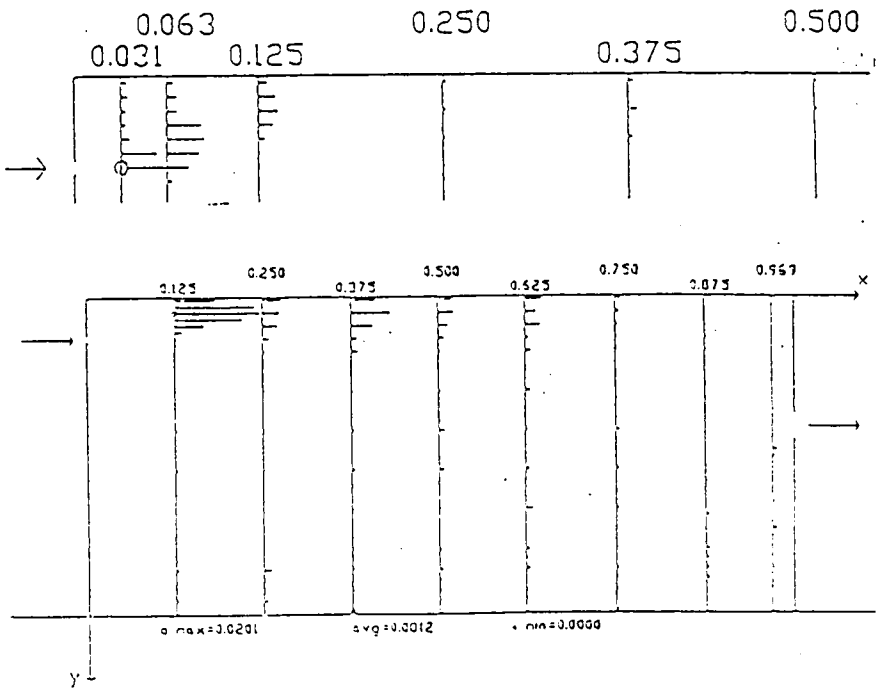


Figure 46
Zhang
Geometry and Probe Locations of Test Room

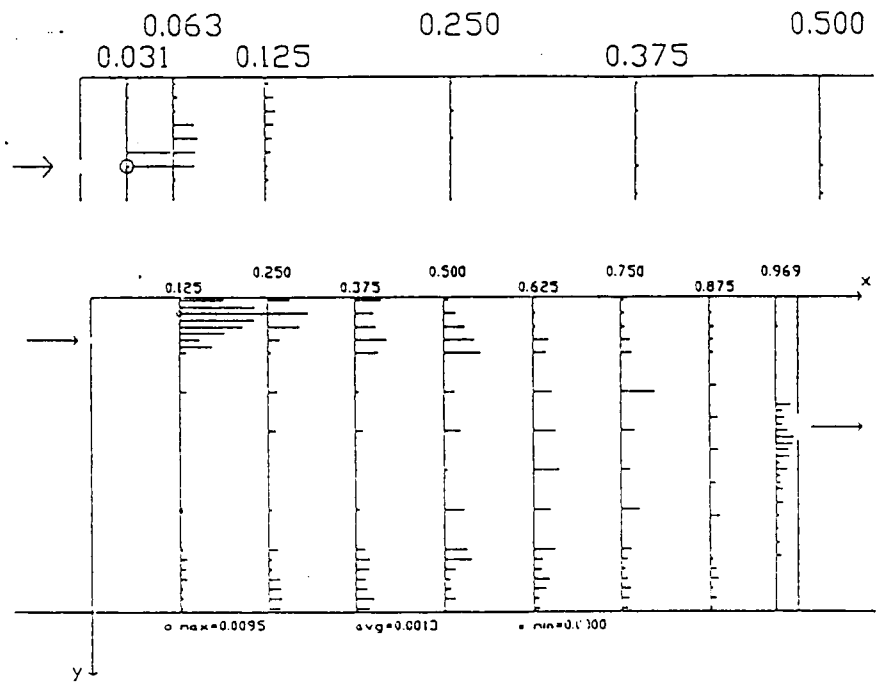
a. jet region:

b. entire flow field:



Length of Bar Indicates Magnitude

Figure 47
Zhang
Distribution of Turbulent Kinetic Energy ($k/0.5U_d^2$)
Isothermal Case



Length of Bar Indicates Magnitude

Figure 48
Zhang
Distribution of Turbulent Kinetic Energy ($k/0.5U_d^2$)
Thermal Case

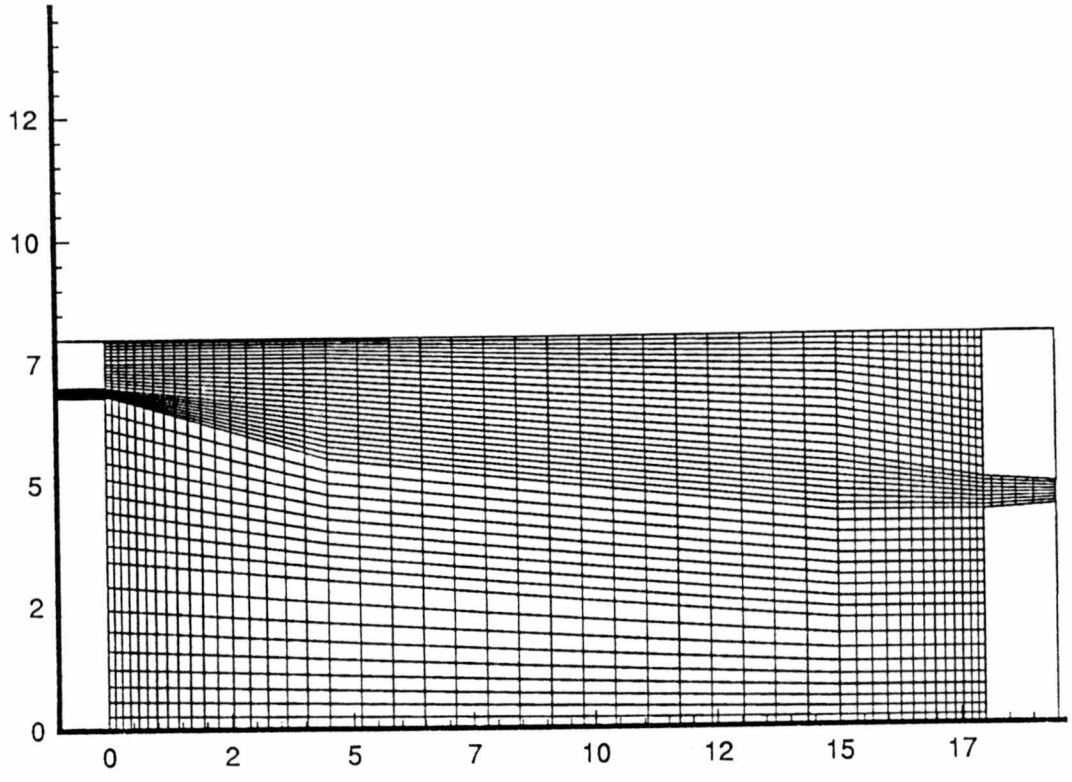


Figure 49
Finite Element Mesh for Test Room Simulations

at the supply diffuser is a geometric singularity. Constraining the velocity at the juncture will most likely result in high local dispersion error, given the narrow width of the supply diffuser. Utilizing a supply duct allows this perturbation to occur downstream of the constrained inflow boundary, and not in the room. A length of one half foot is used for the supply duct, with seven elements in the transverse direction and 4 elements in the longitudinal direction.

A room exhaust duct region is also specified, beyond the room exit plane, due to the geometric singularity at this wall location. Figure 50, from Zhang's report, shows the isothermal visualized flow pattern, as obtained by smoke releases at different locations in the room. The overall flow pattern indicates the velocity field is probably unsteady, thus a non-homogeneous normal derivative at the exhaust plane. In addition, the smoke release immediately before the exhaust plane shows velocity field fluctuations, further indicating the velocity is not normal to the room exit plane.

Computational experiments with the two-dimensional continuity constraint pilot code CFDL.2DPHI were used to establish the length of the exhaust duct. In these computational experiments, various wall boundaries of slip, drag, and no slip were used on the ceiling. The rest of the walls were slip wall boundaries, with a uniform (slug) profile at the inlet boundary. The simulations were performed on an unrotated domain, and with the domain rotated 45^{o} counter-clockwise. The initial unrotated domain simulations used an exhaust duct of only one half a foot which resulted in an unclosed recirculation region forming at the outflow boundary. The exhaust length was then extended to one and a half feet, in an effort to put the outflow boundary beyond the recirculation region. Figure 51 compares the results with the extension of the exhaust duct. The bottom figure with the exhaust duct extended to one and a half feet shows an unclosed recirculation region still forming at the outflow boundary. In order to dampen the recirculation cell forming at the outflow boundary, the exhaust duct was then tapered to accelerate the flow. The final mesh for the exhaust duct contains five elements in the longitudinal direction with seven in the transverse direction.

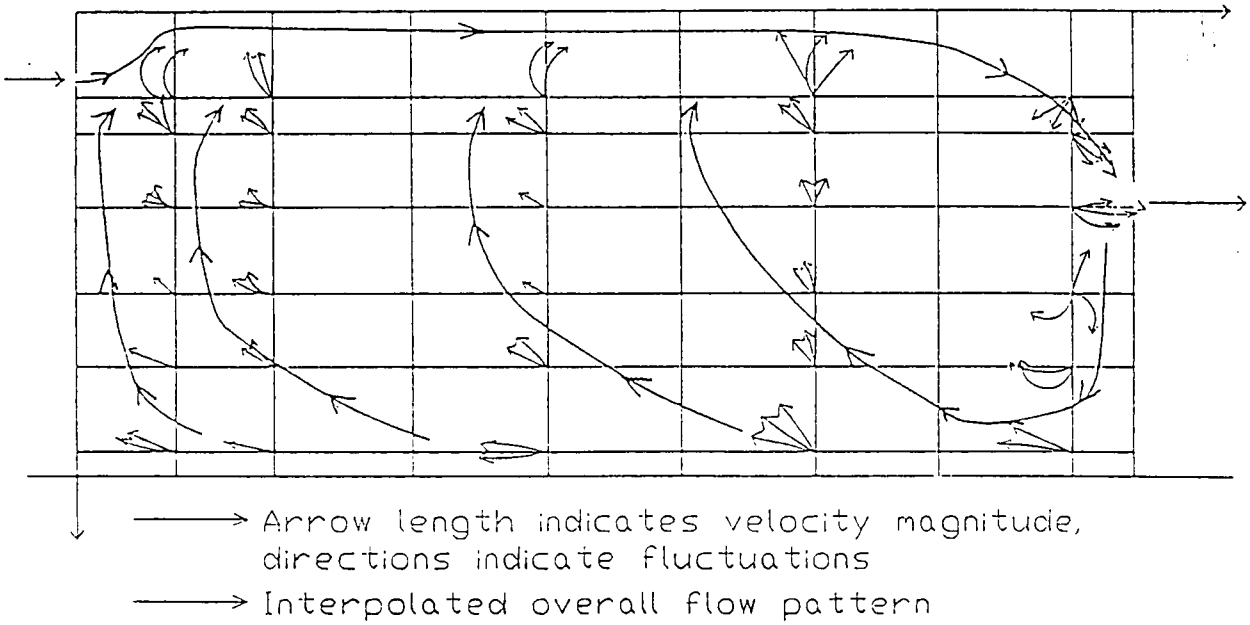
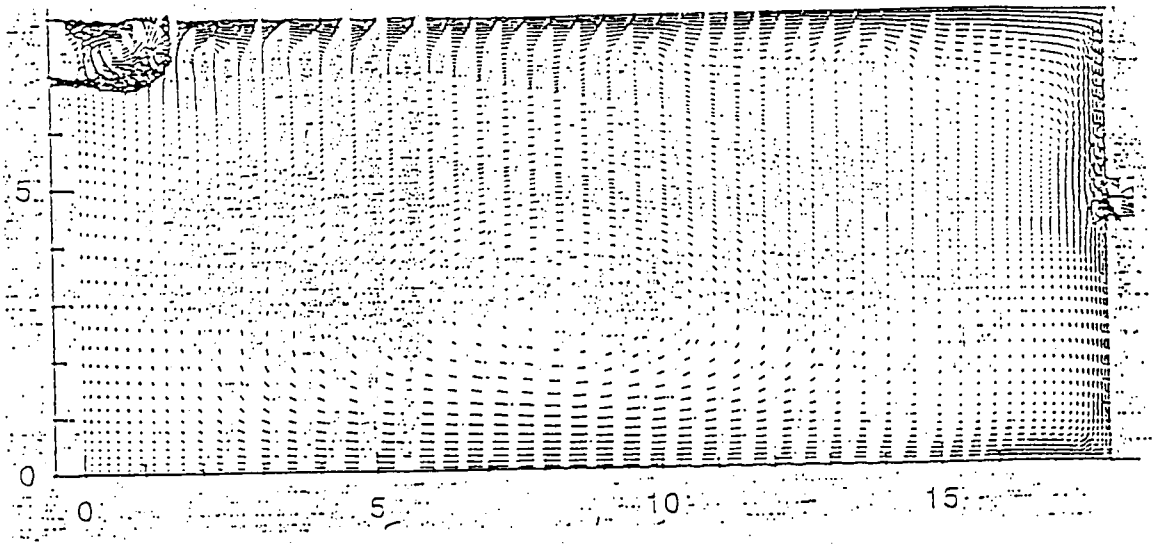


Figure 50
Flow Pattern of Test Room from Zhang
Isothermal Case

A). Exhaust Duct Length = 1/2 ft.: No Slip Ceiling



B). Exhaust Duct Length = 1 1/2 ft.: No Slip Ceiling

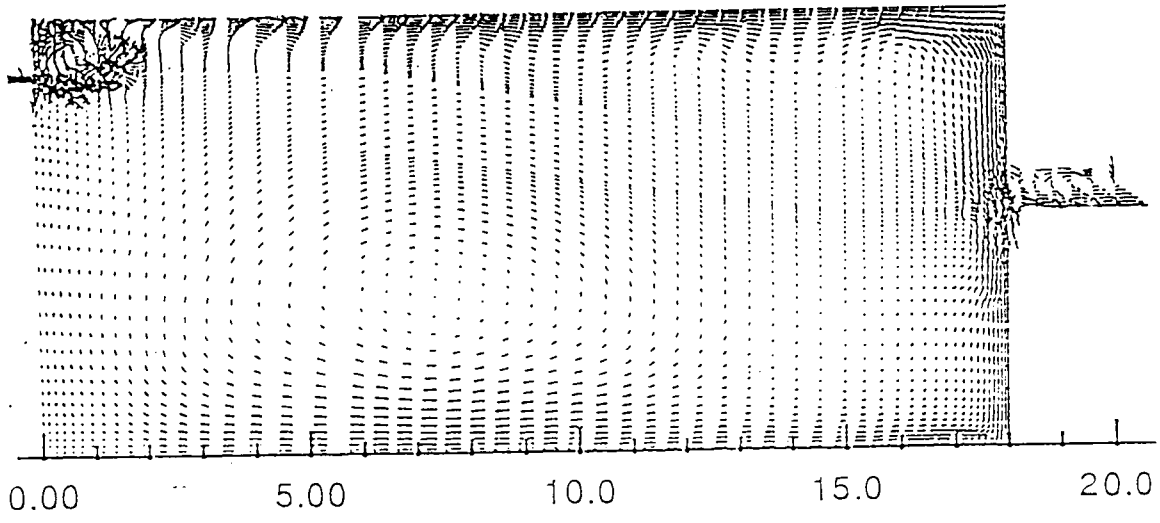


Figure 51
Velocity Vector Field
CFDL.2DPHI Pilot Code

Within the room itself, 47 elements span the longitudinal direction, with 43 elements spanning the transverse direction. A non-uniform refinement is applied near the walls and wall junctures with the supply and exhaust ducts.

Figure 52 is the velocity characteristics at the supply diffuser reported by Zhang, which is assumed to be taken at the supply diffuser exhaust plane into the room. The velocity profile resembles partially developed turbulent channel flow profile, with perturbations at the edges caused by the local expansion into the room. In the simulation, upon reaching the supply diffuser wall juncture, the expansion into the room should perturb the velocity profile in a similar manner. As an approximation, a fully developed laminar duct flow profile is used as the inlet boundary conditions for velocity at the supply diffuser duct. No slip wall boundary conditions are used at all the walls including the supply and exhaust ducts. The domain is rotated 30^{o} counter-clockwise to eliminate any round-off error accumulation due to velocity level disparities in the supply duct (where the v component velocity is virtually zero). A reference length of 1 (L=1ft.) with a reference velocity of 1 (U=1ft/sec) are used for the simulations, producing a reference time scale of unity. A value of ν_q=0.1 for artificial viscosity of momentum and temperature is used, based on the benchmark results, which should be sufficient to damp any solution oscillations generated within the supply diffuser region.

Isothermal Case

Figure 50 was used in establishing the initial conditions for the isothermal test case. The figure shows the supply jet attaching to the ceiling after entering the room. This is due to the Coanda effect, where the pressure difference below and above the jet lift the jet to the ceiling. To simulate the Coanda effect, the supply jet was constrained to a temperature of 75^{o}F while the ceiling is heated to 80^{o}F, which should produce a stable thermal stratification. The temperature difference of 5^{o}F results in an Archimedes number of 0.3. When the fully developed ceiling jet reached the far wall, the thermal effects were removed and the simulations proceeded as isothermal. Figure 53 shows the velocity field this computed as the initial conditions of both the isothermal and non-isothermal simulations. The corresponding isotherm distribution is also shown for reference.

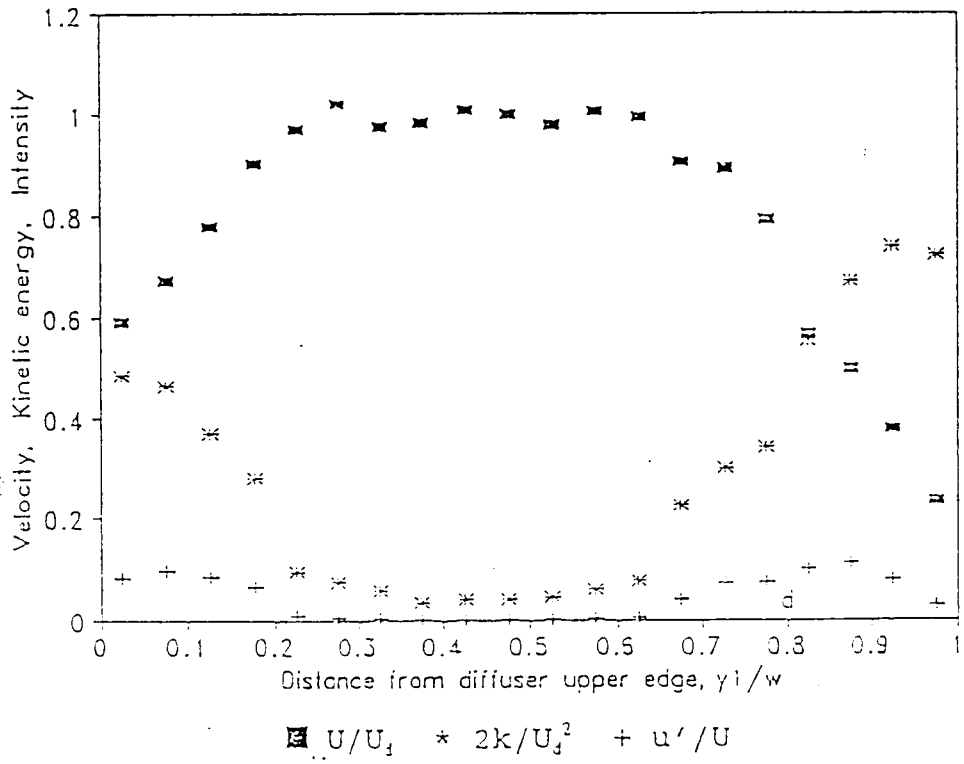


Figure 52
Zhang
Velocity Profile at Supply Diffuser

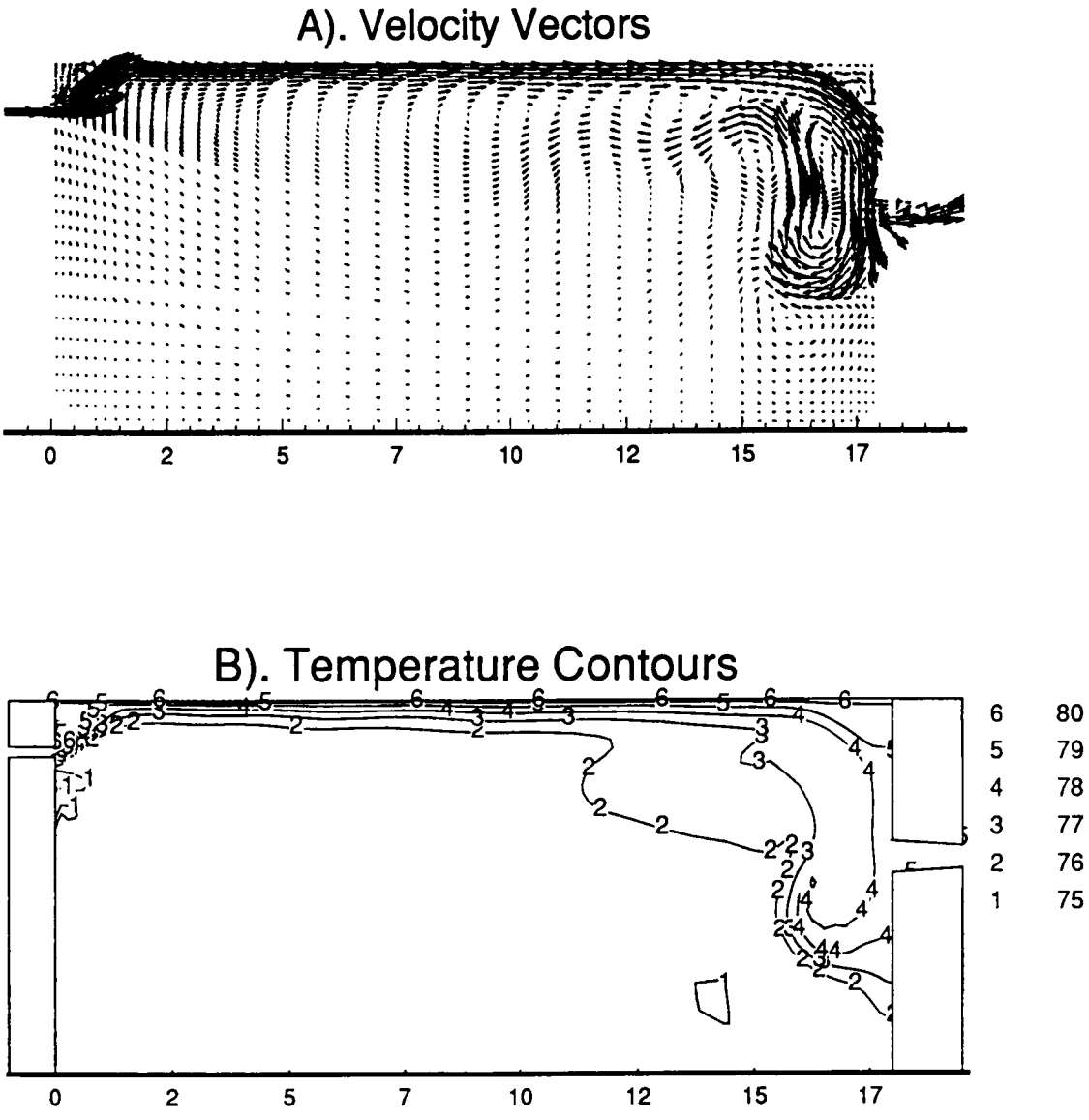


Figure 53
Initial Conditions - Isothermal Case

The simulations were carried out for 100 time steps and then stopped due to difficulties in the iteration sequence, the time step size was decreasing to an unacceptable value of 10^{-5}. The problem is located at the outflow diffuser, where a recirculation region still formed across the outflow boundary. The top figure of Figure 54 shows the velocity vector plot at 33 seconds with the perturbation at the outflow causing the difficulty in the time integration. To correct the problem, the effective Reynolds number within the exhaust diffuser was decreased to 100, by locally increasing Re^t to 55. The resultant physical damping (instead of numerical) gives a more stable solution, as verified in the lower figure of Figure 54.

The simulations were continued from the stable velocity field of Figure 54 with the Reynolds number reduce to 10 (Re^t=550) in the exhaust duct to provide additional damping. Figures 54 through 65 are snapshots at approximately 5 second intervals showing the time evolution of the velocity and streamfunction solutions. The streamfunction contours are provided to distinguish the mass flow pattern enhancing the recirculation regions. At ~5 seconds, Figure 56, oscillations form in the supply jet indicating an unsteady solution is developing, and a main recirculation cell develops below the jet due to the return flow that is unable to exit the exhaust duct. In addition to the main cell, a minor cell forms above the jet. By ~21 seconds, Figure 59, the main cell has reached a stationary position, with the top cell reaching the far wall above the exhaust. In a periodic pattern as the solution progresses, the top cell progresses along the ceiling until dissipating on reaching the far wall and eventually reforms at approximately half the length of the room. The final field presented at 50 seconds (Figure 65) shows the top cell pushing the supply jet to the floor forming a recirculation region in front of the exhaust. The supply jet still contains longitudinal oscillations for an unsteady solution.

The final velocity vector field in Figure 65 from the simulation results agrees partially with the flow field from the smoke releases given in Figure 50. The interpolated flow field from the experimental results shows fluctuating patterns in the flow field supporting an unsteady solution, but the sparsity of the data lacks detail to identify localized recirculation regions if they exist. The combination of the unsteady pattern and the sparse location of the smoke releases make interpretation of a general flow pattern inaccurate.

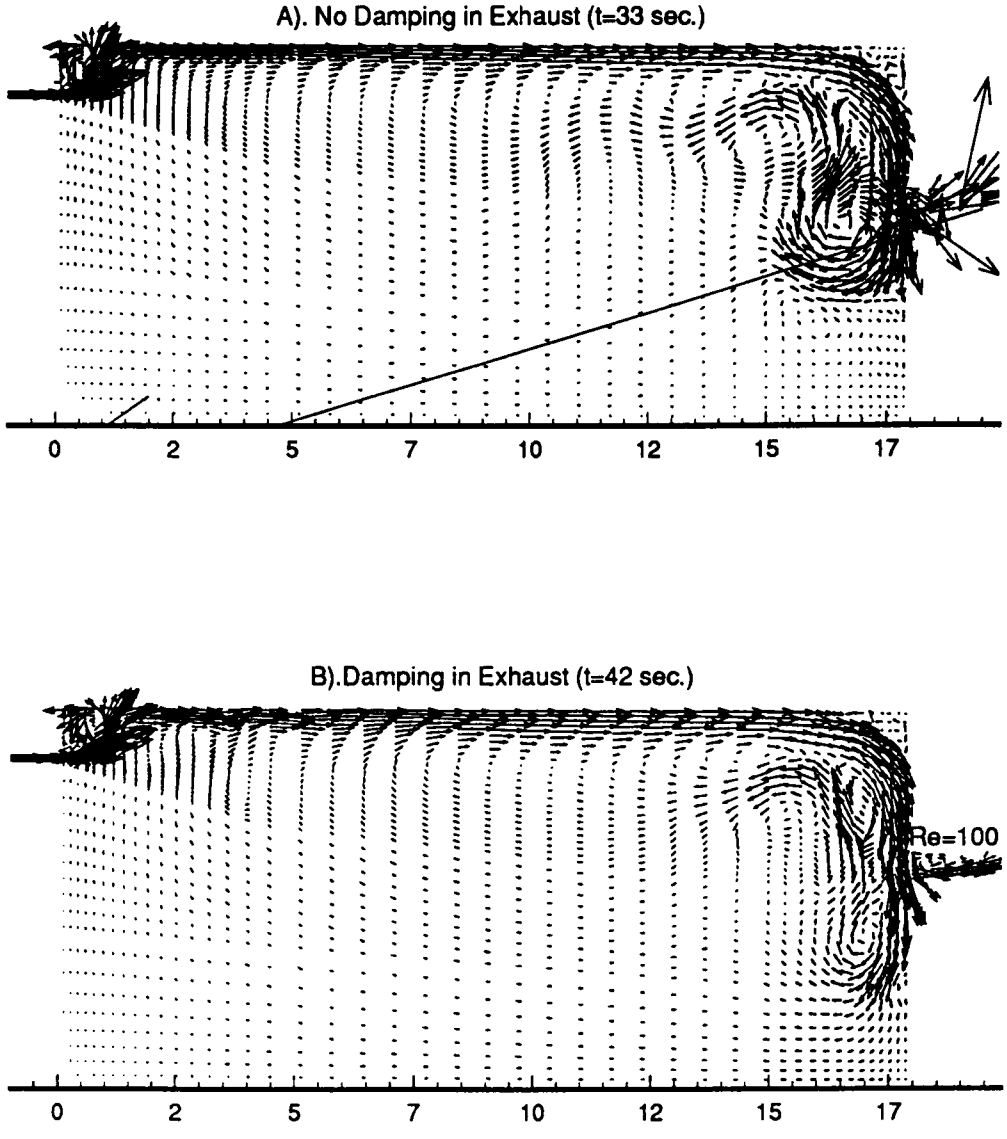


Figure 54
Physical Damping in Exhaust Duct

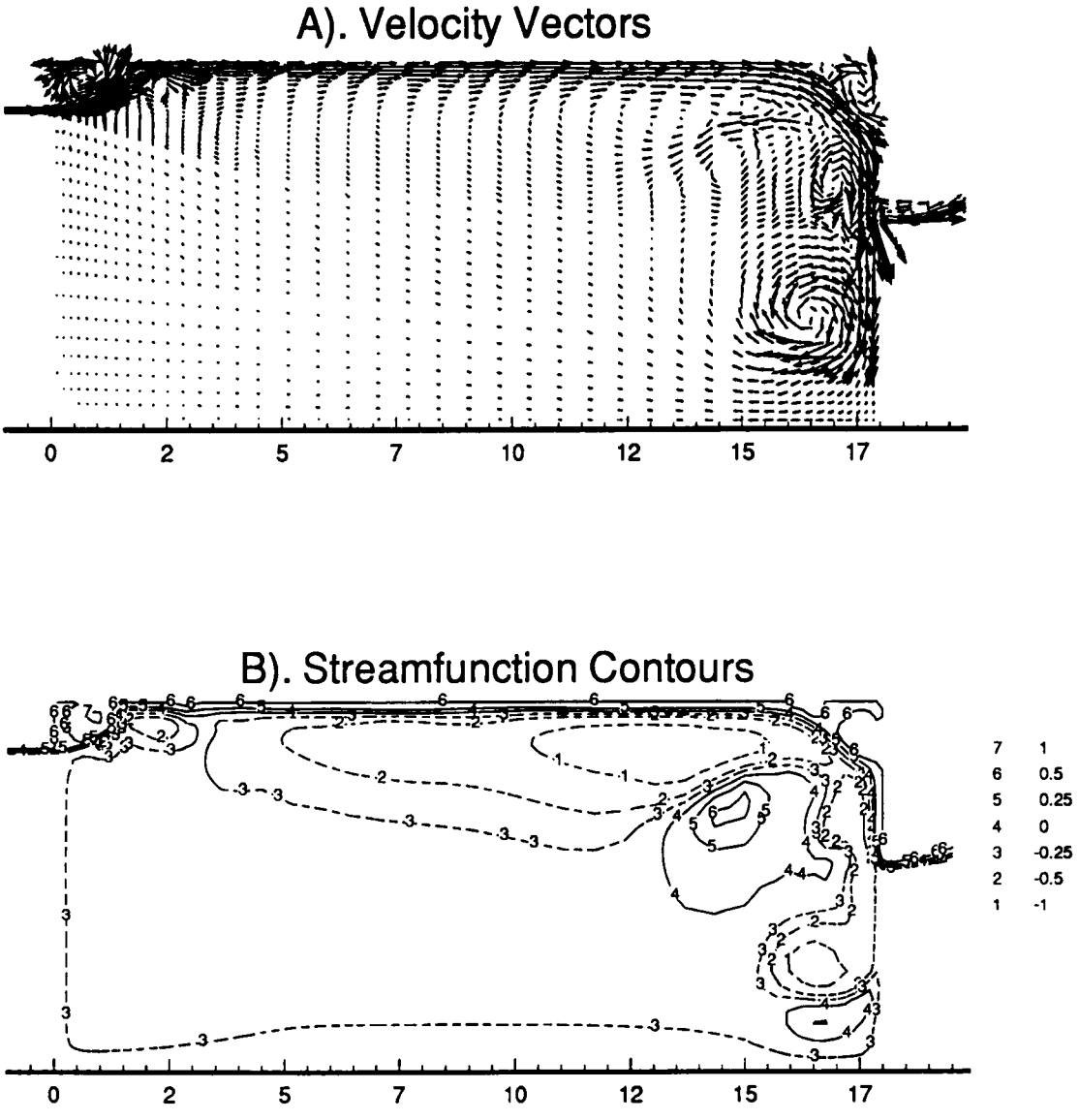


Figure 55
Isothermal Case (time = 1.4 sec.)

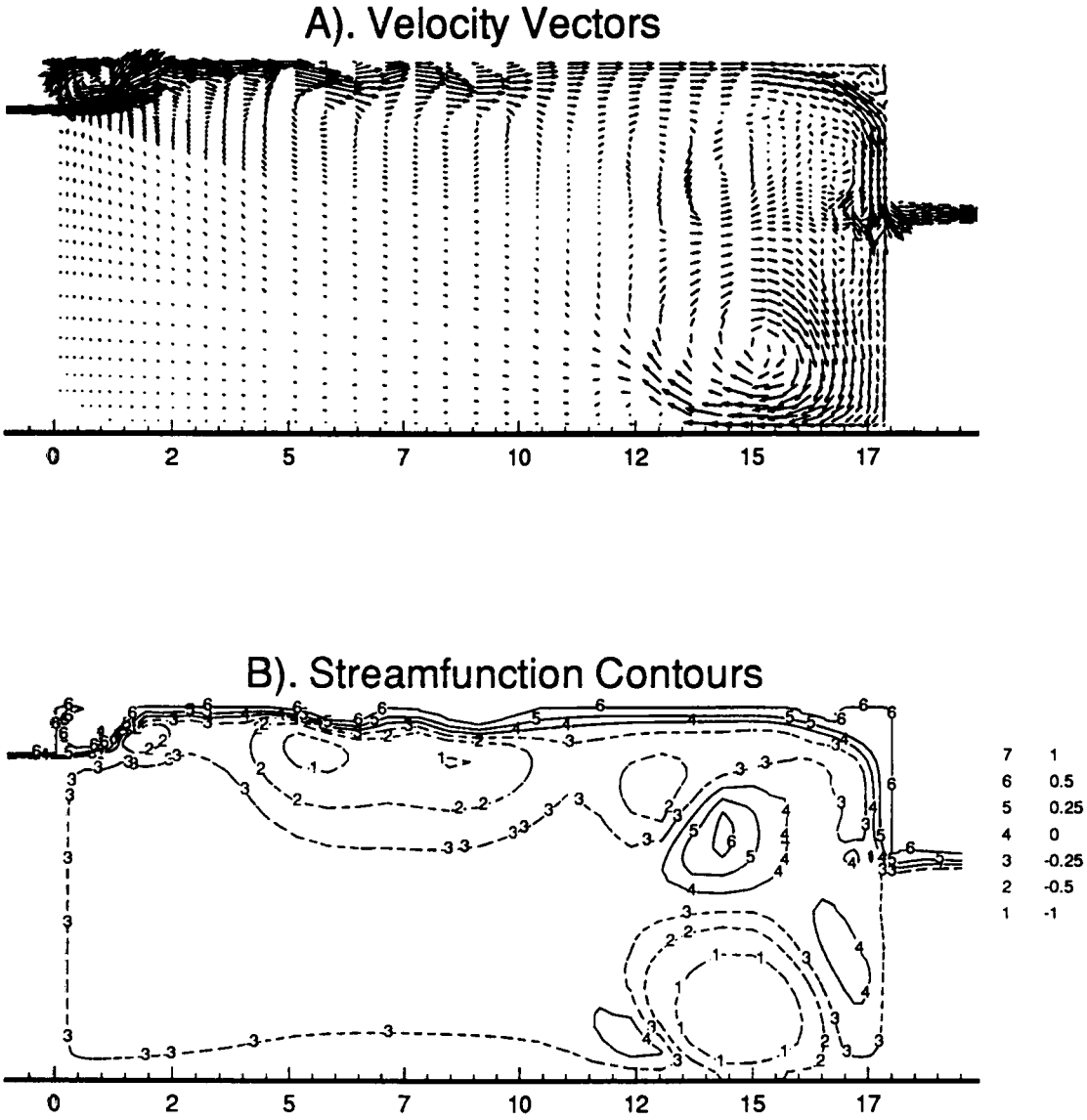


Figure 56
Isothermal Case (time = 5.1 sec.)

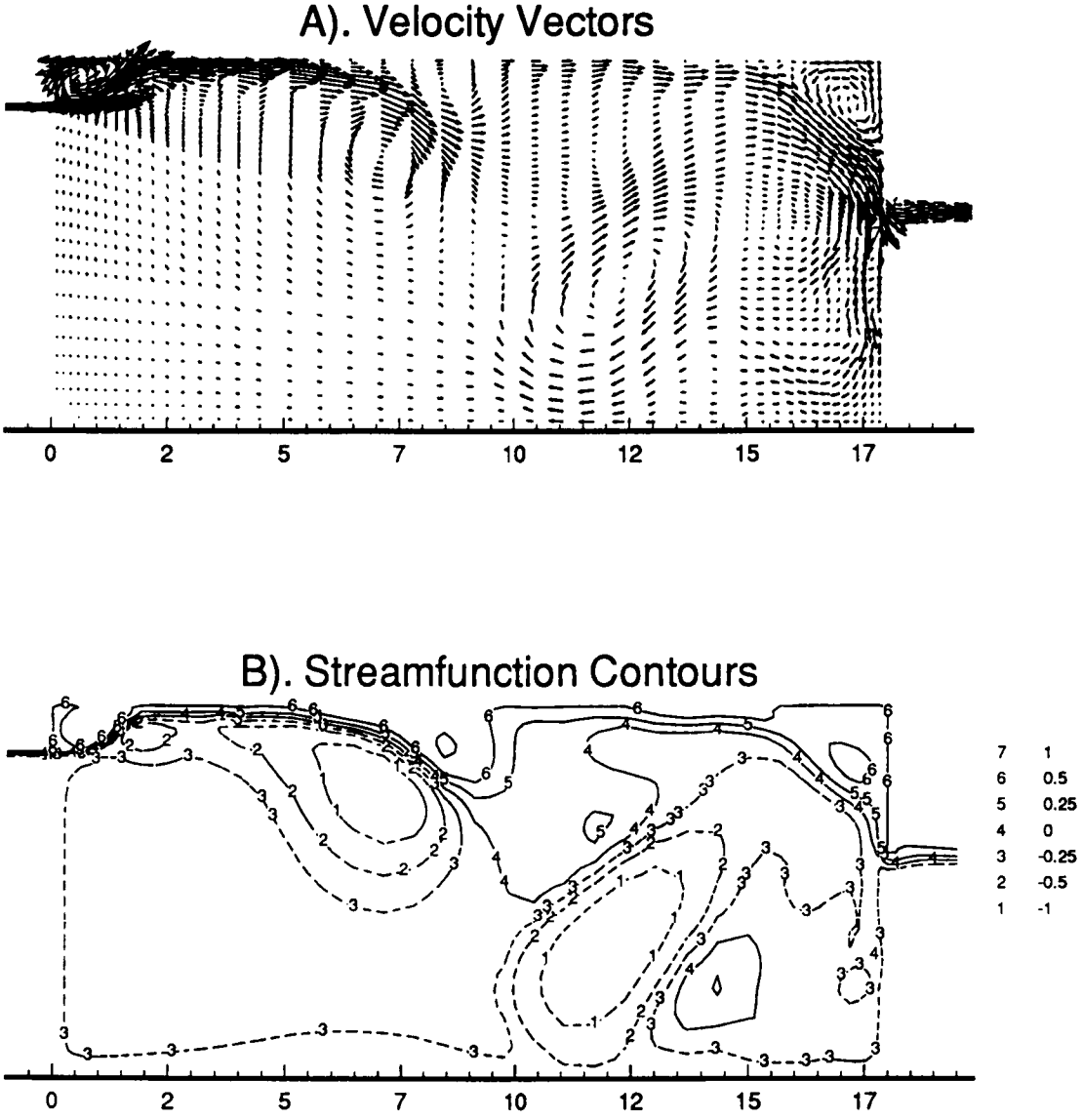


Figure 57
Isothermal Case (time = 10.9 sec.)

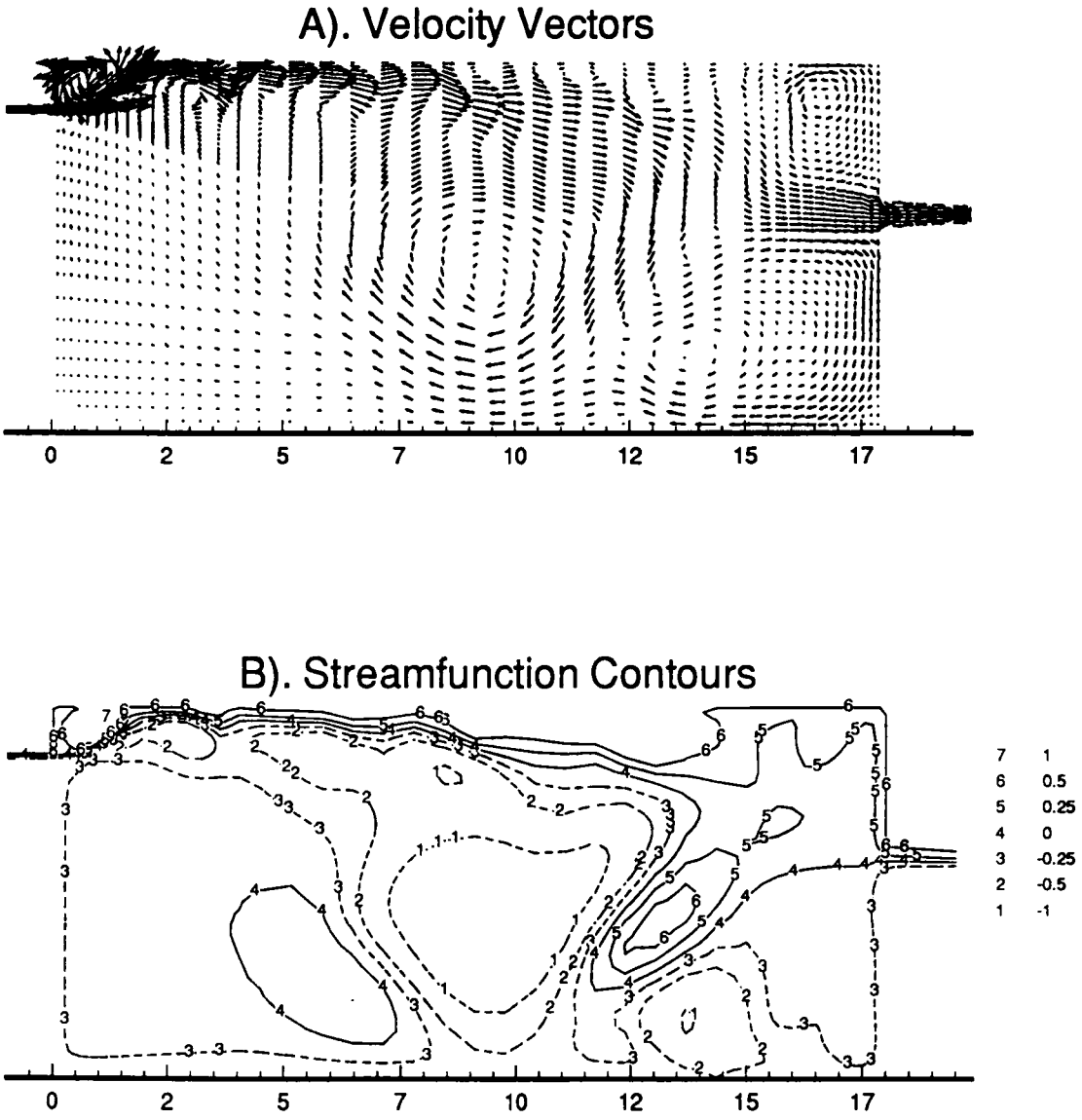


Figure 58
Isothermal Case (time = 16.9 sec.)

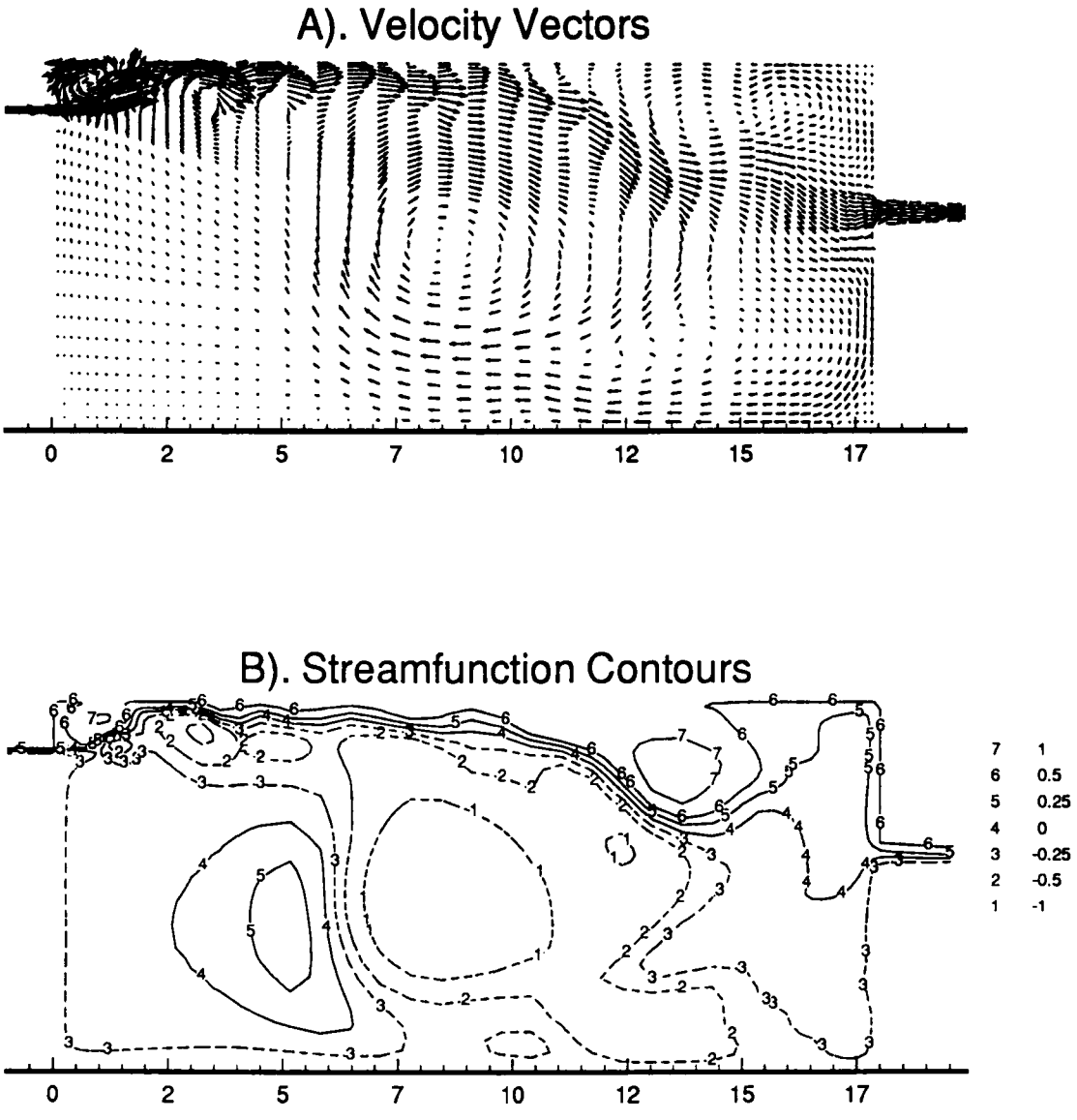


Figure 59
Isothermal Case (time = 20.8 sec.)

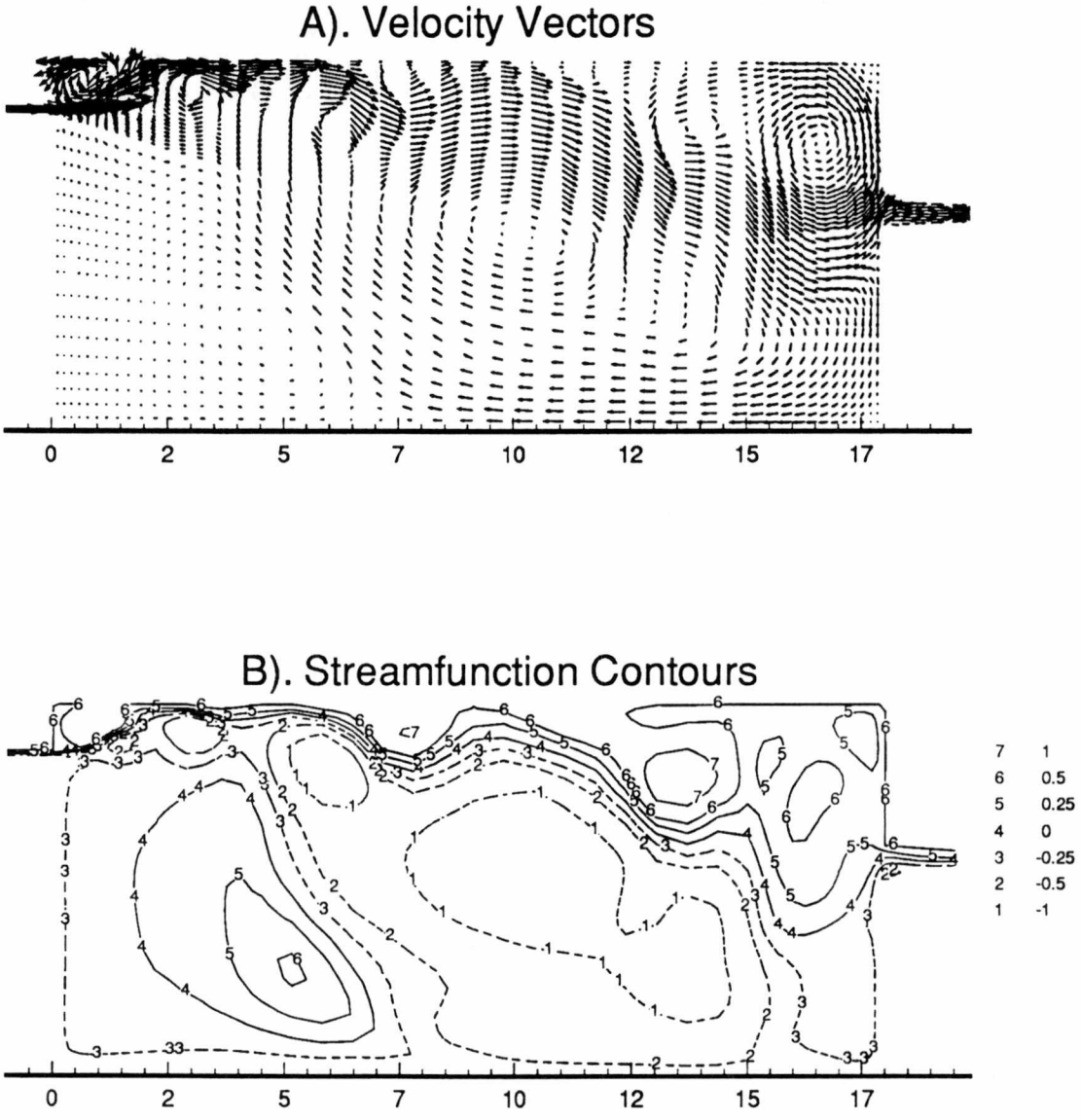


Figure 60
Isothermal Case (time = 26.7 sec.)

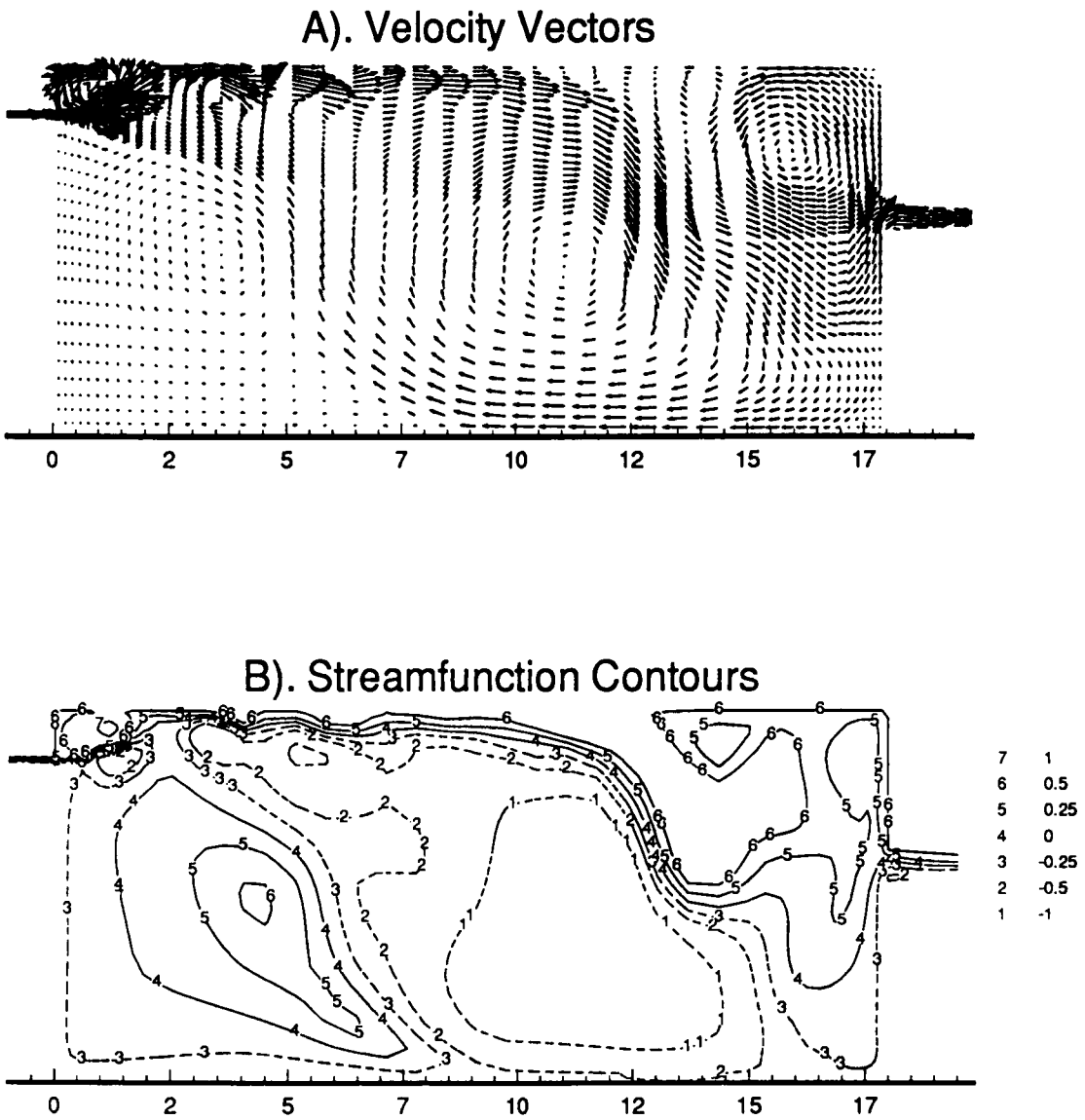


Figure 61
Isothermal Case (time = 30.6 sec.)

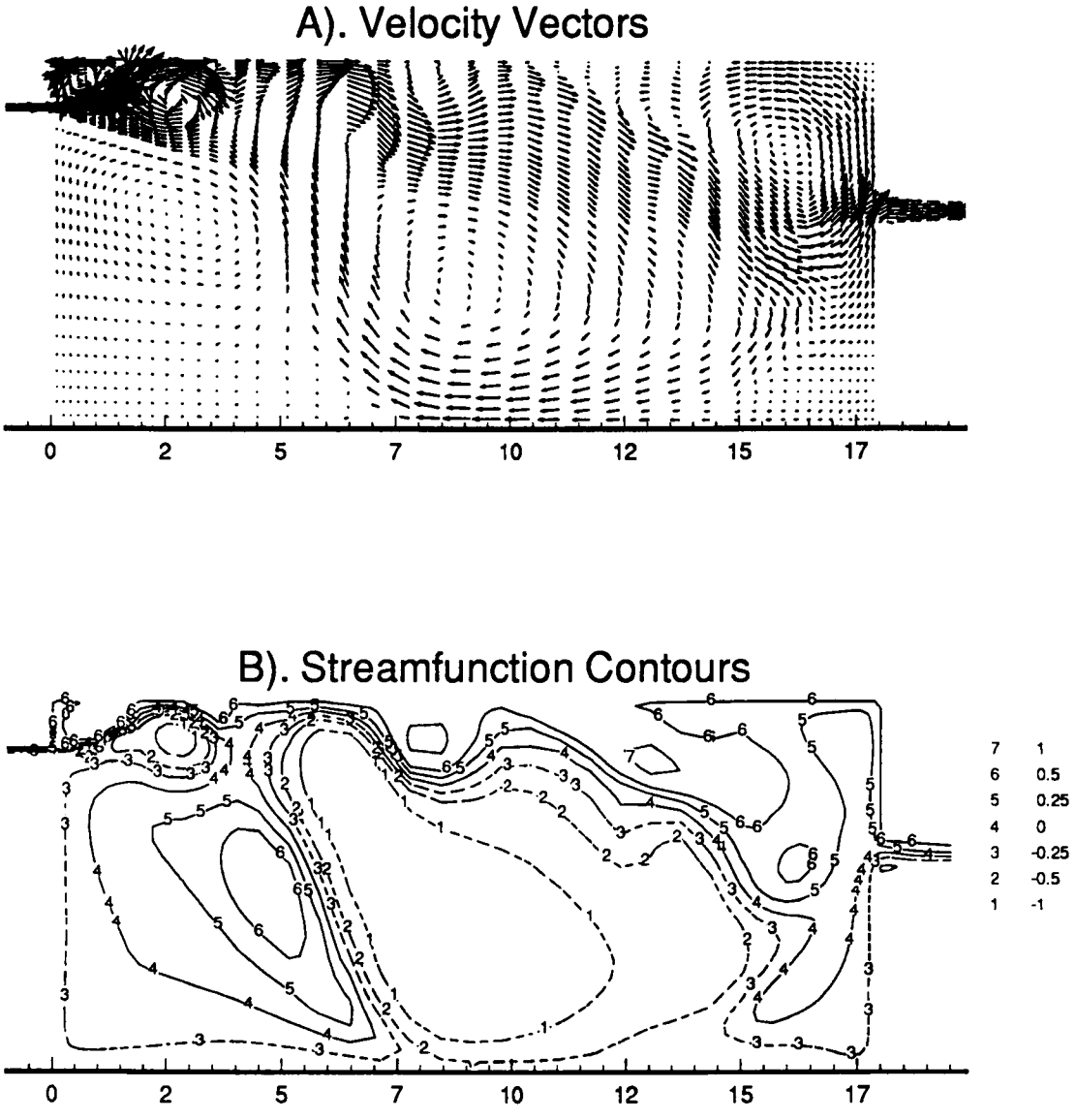


Figure 62
Isothermal Case (time = 35.5 sec.)

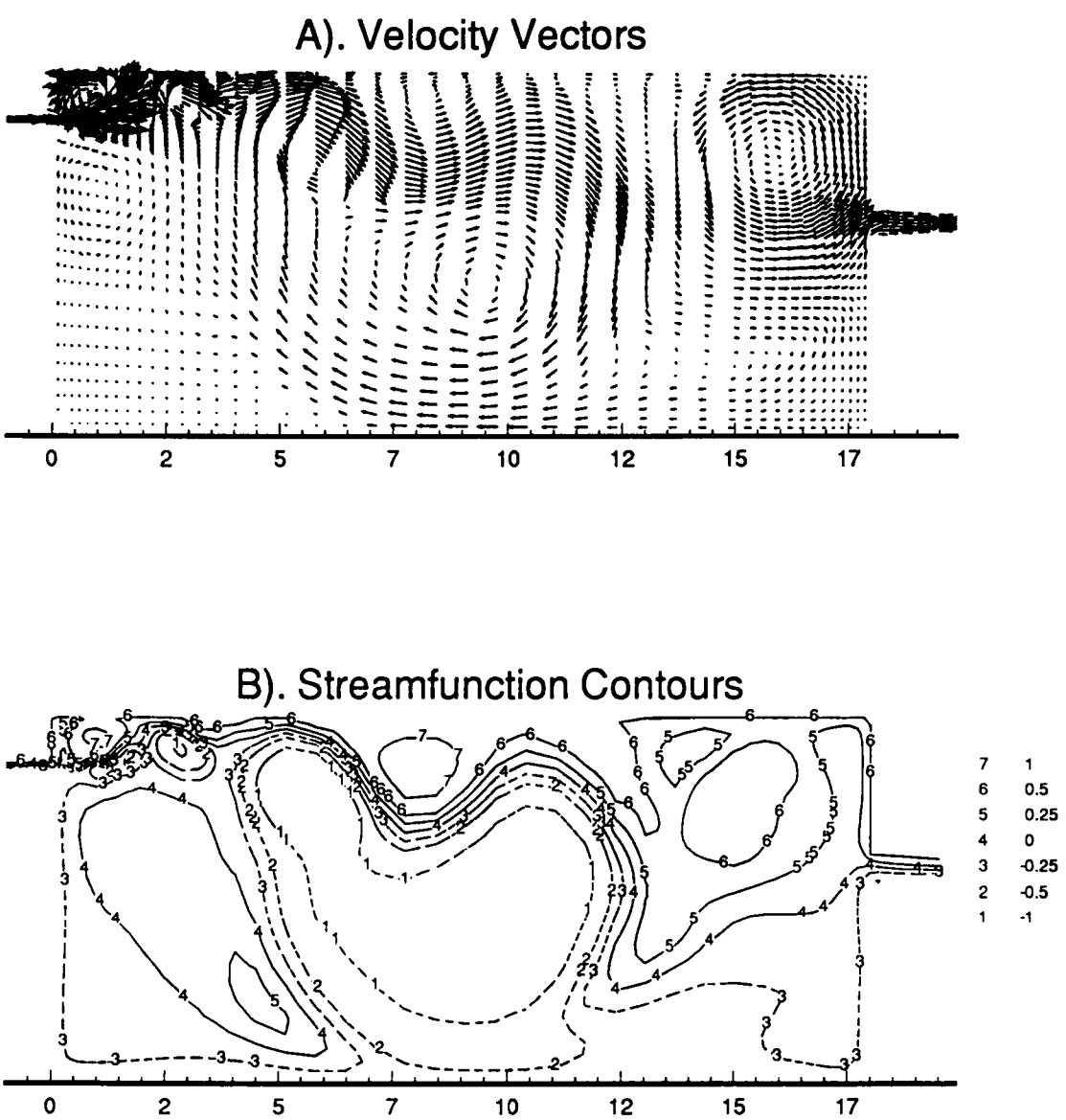


Figure 63
Isothermal Case (time = 40.4 sec.)

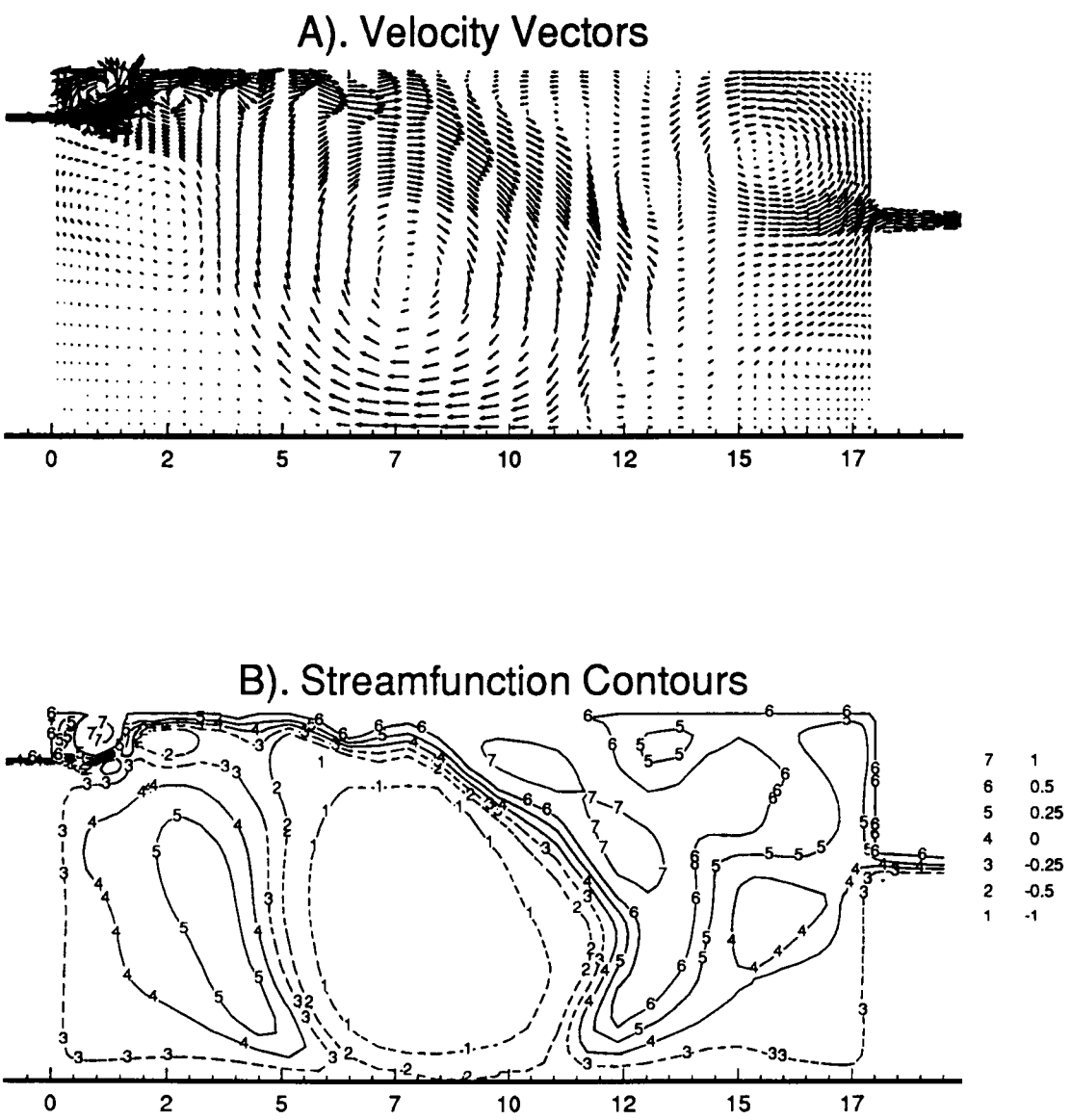


Figure 64
Isothermal Case (time = 46.6 sec.)

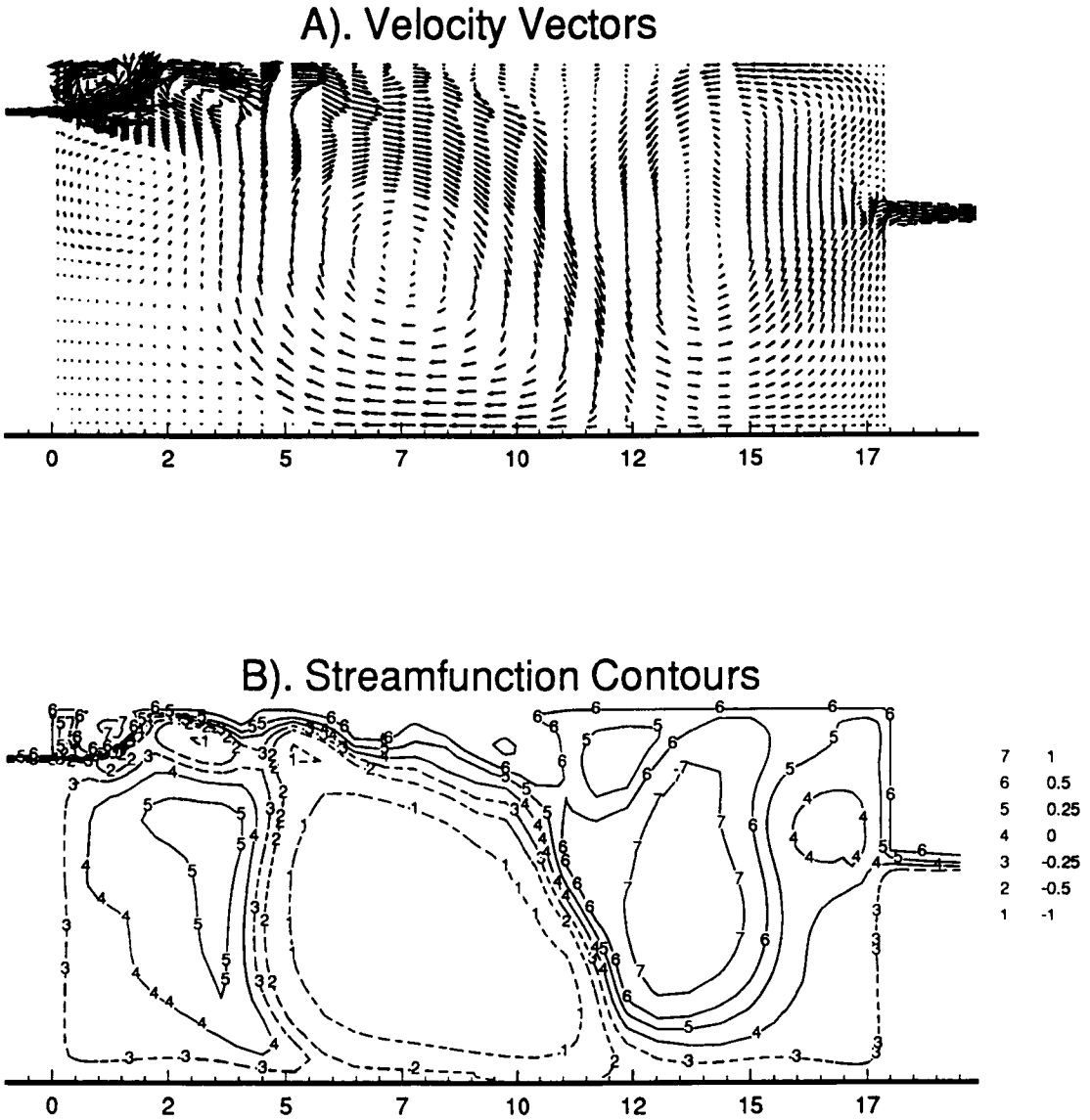


Figure 65
Isothermal Case (time = 50.0 sec.)

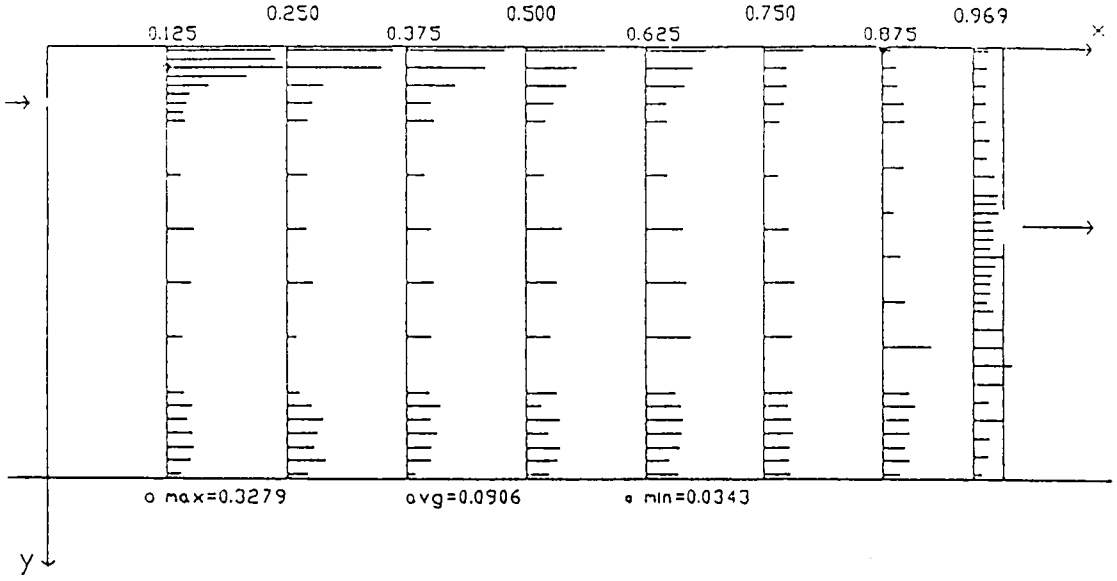
Figure 66 compares the time-averaged velocity magnitudes from the probes of the experimental results and the magnitudes obtained at 50 seconds in the simulations. The comparison in this figure shows a general better agreement, but discrepancies still exist. The top recirculation cell is highlighted in the simulation results by a smaller magnitude which is lacking in the experimental results. In addition, the experimental results show the return flow along the floor extending almost the entire length of the room, whereas the simulations show the return extending approximately two-thirds the length of the room. The discrepancy is partly due to the time-averaging of the velocity magnitudes in the experimental results, instead of providing instantaneous values. The time-averaging will smooth out the fluctuations inherent in the unsteady velocity. The other cause of disagreement is possibly due to the lack of a turbulence closure model in the simulation results. Figure 47 shows that the turbulent kinetic energy, which is a diffusive phenomena, generated at the supply diffuser dissipates at approximately half the length of the room allowing the jet to progress along the ceiling. The simulations contain a constant Re^t which actually dissipates the jet, causing the jet to drop to the floor.

Figure 67 shows the pressure map of the solution at 50 seconds of the entire room with a close-up of the supply diffuser region. The pressure map of the room shows the low pressure region within the center of the room where the main recirculation cell is located, with the pressure recovering then dropping again toward the exhaust. The close-up of the supply diffuser shows the pressure drop associated with the sudden expansion with a pressure differential lifting the supply jet to the ceiling. The close-up does shows what might be minor mesh scale oscillations that are dissipated shortly after entering the room.

Non-isothermal case:

Zhang's non-isothermal case involved a cool jet entering a room with a heated floor. The supply jet was maintained at 75.4^{o}F with the floor temperature maintained at 142.7^{o}F. With a temperature change of 67.3^{o}F and the reference values of unity , the Archimedes number in the simulations is 3.9. The Reynolds number of the exhaust duct was set to 10 as in the isothermal case with an Archimedes number of zero to prevent any buoyancy effects occurring within the duct.

A). Experimental Data (U/U_d)



B). Simulation Results (u/U)

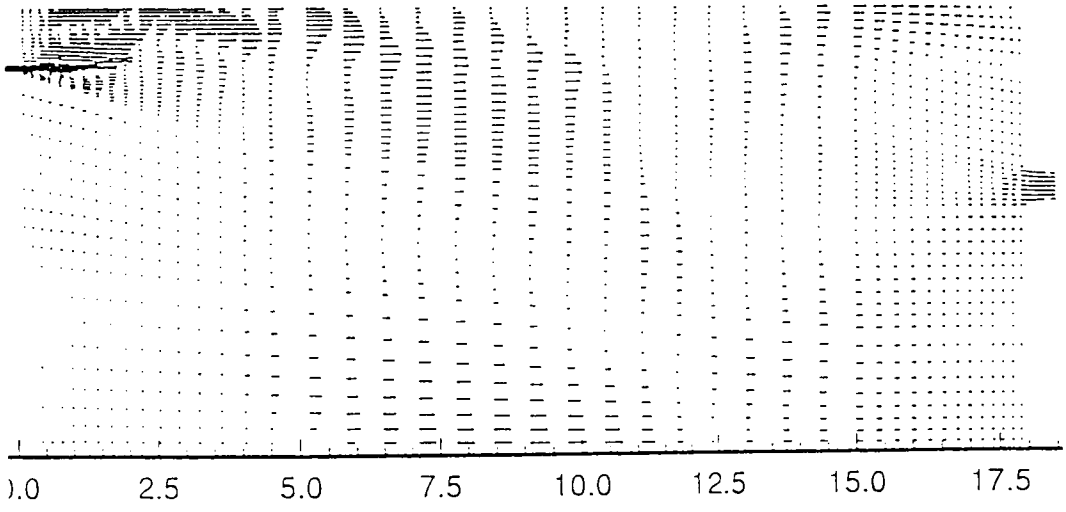


Figure 66
Velocity Magnitude Distribution

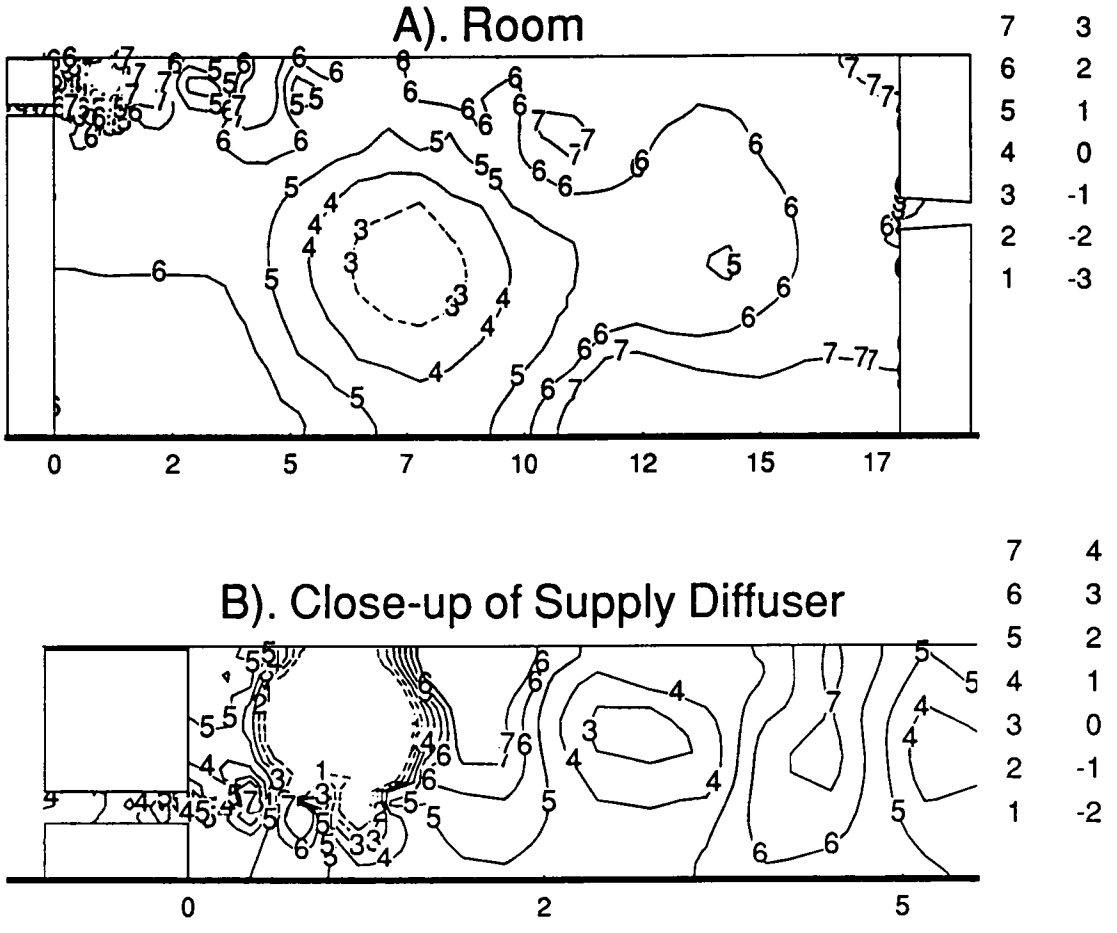


Figure 67
Final Pressure Map

The initial conditions for the velocity and temperature fields are presented in Figure 68. The initial velocity field is the same used for the isothermal case with the streamfunction contours superimposed for reference. The initial temperature field is the solution to the potential equation for temperature (16) with a heated floor and cooled ceiling providing a linear gradient.

Figures 68 through 75 are snapshots of the velocity/streamfunction field and the corresponding temperature field at selected times to show the evolution of the flow pattern. Within ~6 seconds, Figure 69, the cold supply jet entering the warm room drops toward the floor. Buoyancy effects has generated a recirculation cell forming below the exhaust. The region below the supply diffuser is still relatively inactive as shown by the remnants of the linear temperature gradient from the initial condition. By ~8 seconds, Figure 70, buoyancy has caused a "wall jet" to form across the floor producing a large recirculation cell below the supply diffuser. Figure 72 through 75 (11.8 seconds through 31.6 seconds) show a complex flow pattern developing from the cold jet impinging on the warm floor which eventually lifts the jet, with no discernible periodic pattern having yet developed.

Figure 76 compares the observed air flow pattern from the experimental results with the final flow field at 31.6 seconds. The smoke releases show a large random behavior in the flow pattern as produced in the simulation results. The general flow pattern obtained from the smoke releases agrees fairly well with the simulation results, but still lacks the detail to determine the flow pattern accurately. In addition, the random behavior of the flow field makes generating a stable flow pattern unreliable. No comparison is made of the velocity magnitude distributions since the experimental data provides time-averaged values, which eliminate the fluctuating patterns of the flow field.

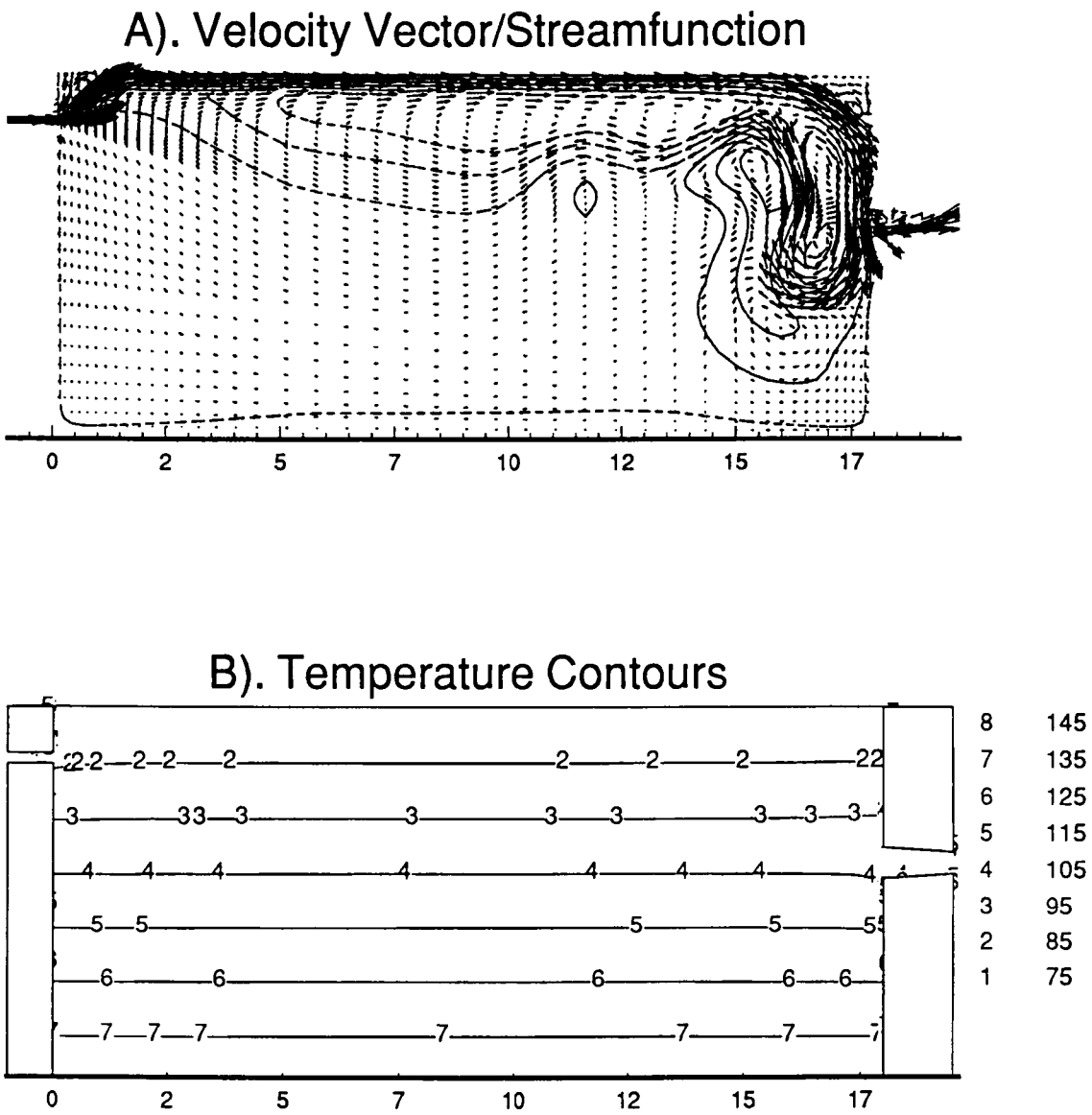
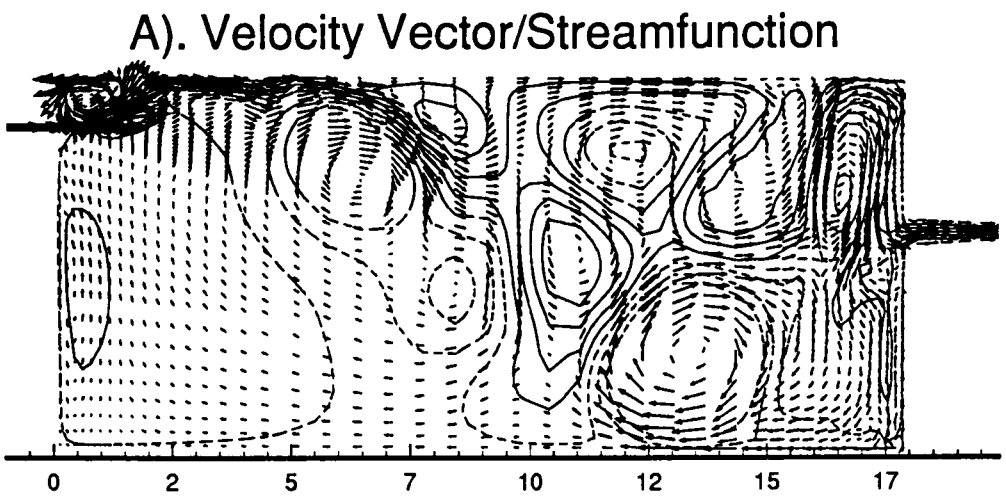


Figure 68
Non-isothermal Case (Initial Conditions)



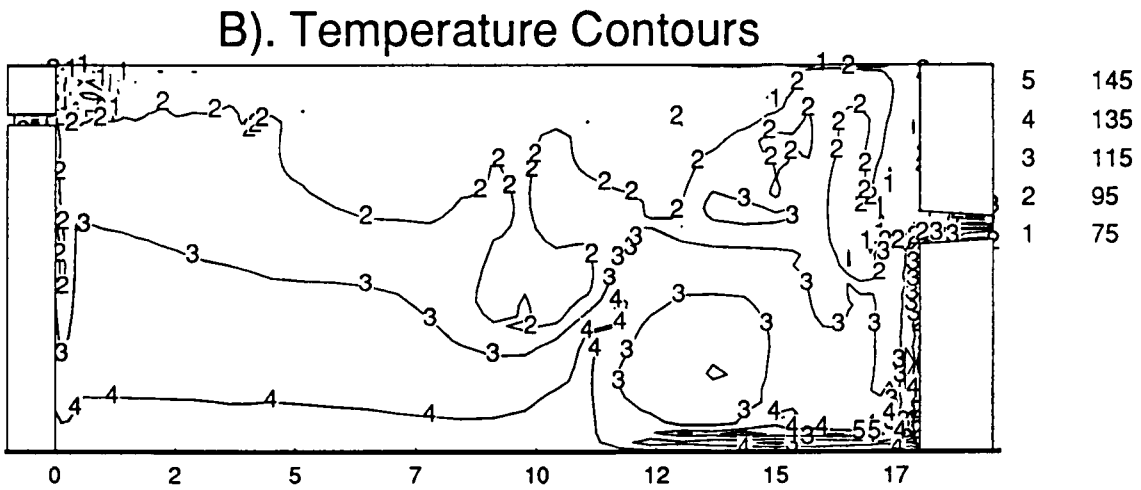


Figure 69
Non-isothermal Case (time = 5.5 sec.)

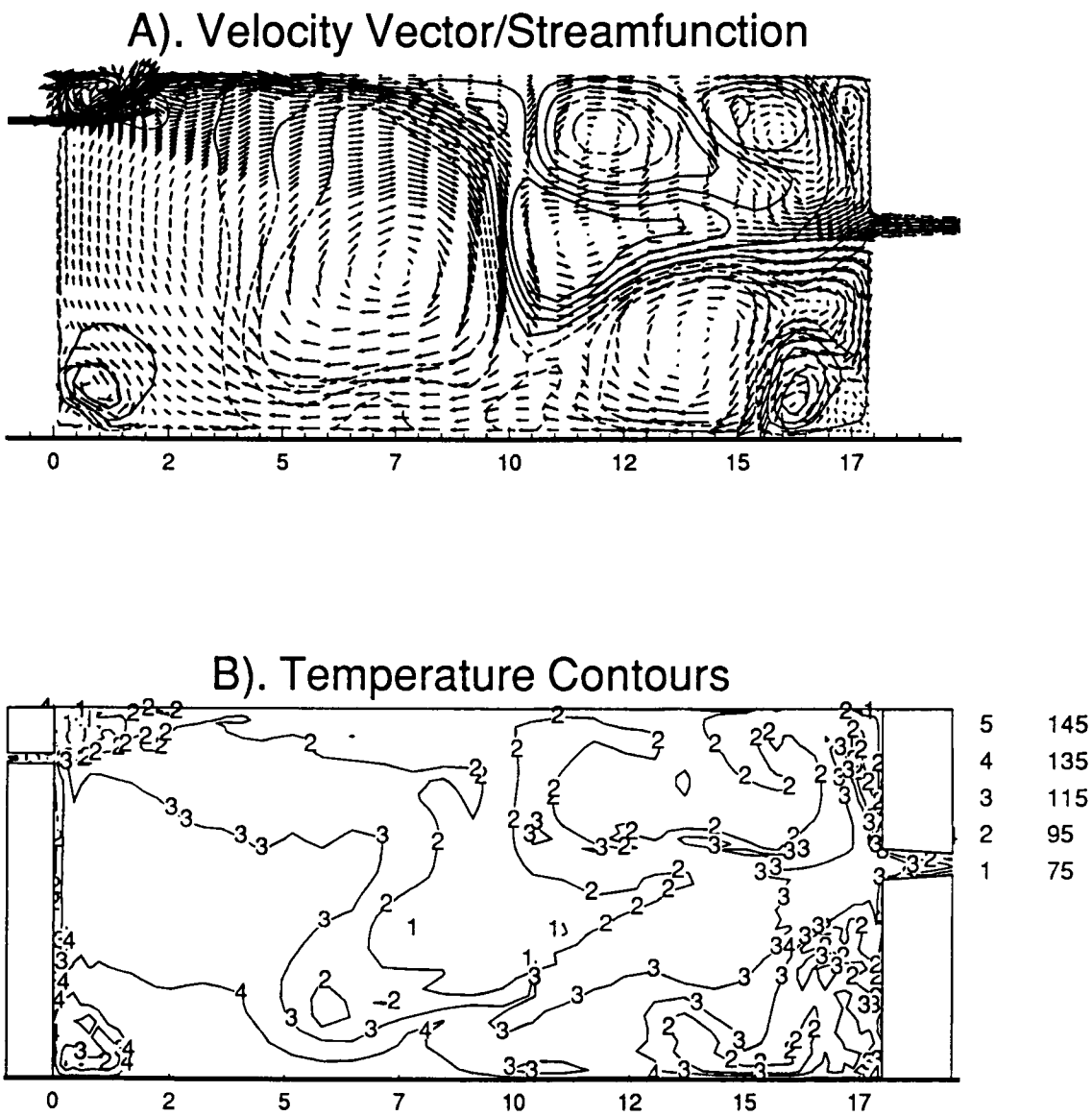


Figure 70
Non-isothermal Case (time = 7.9 sec.)

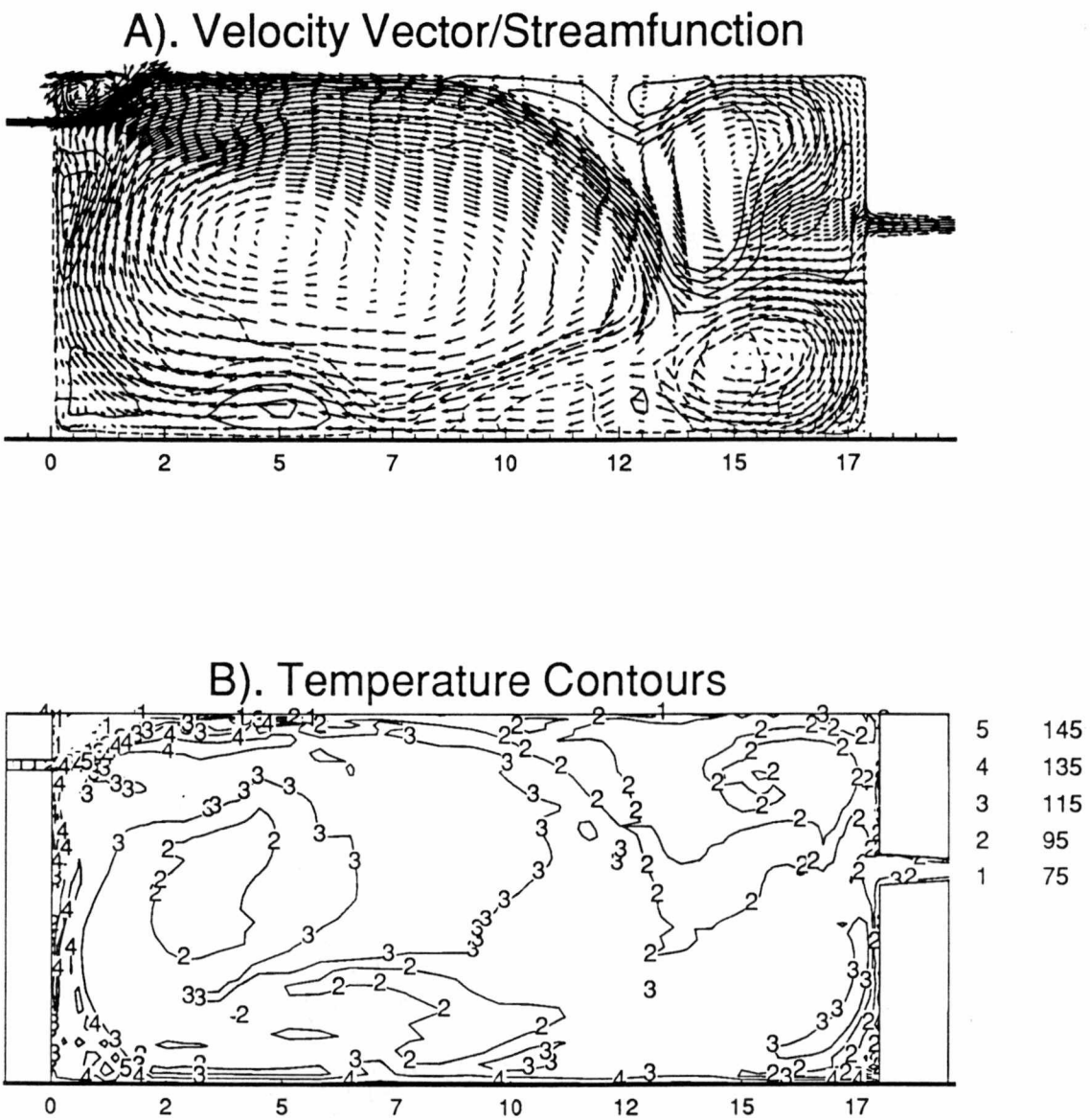
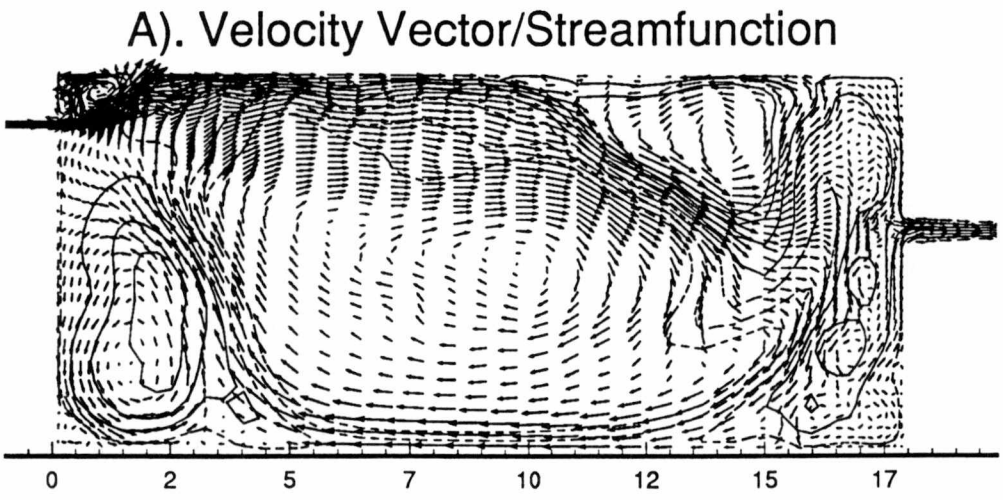


Figure 71
Non-isothermal Case (time = 11.8 sec.)



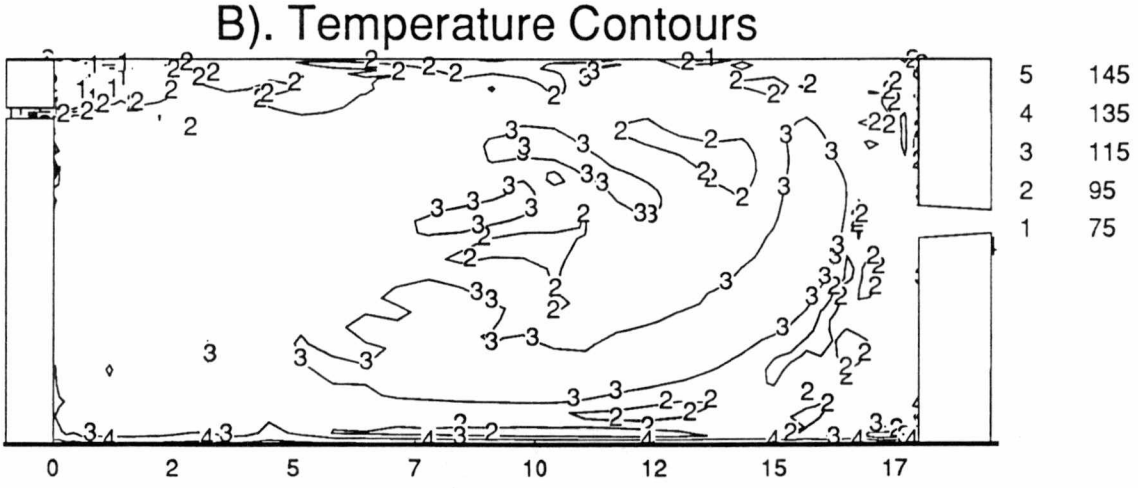


Figure 72
Non-isothermal Case (time = 17.9 sec.)

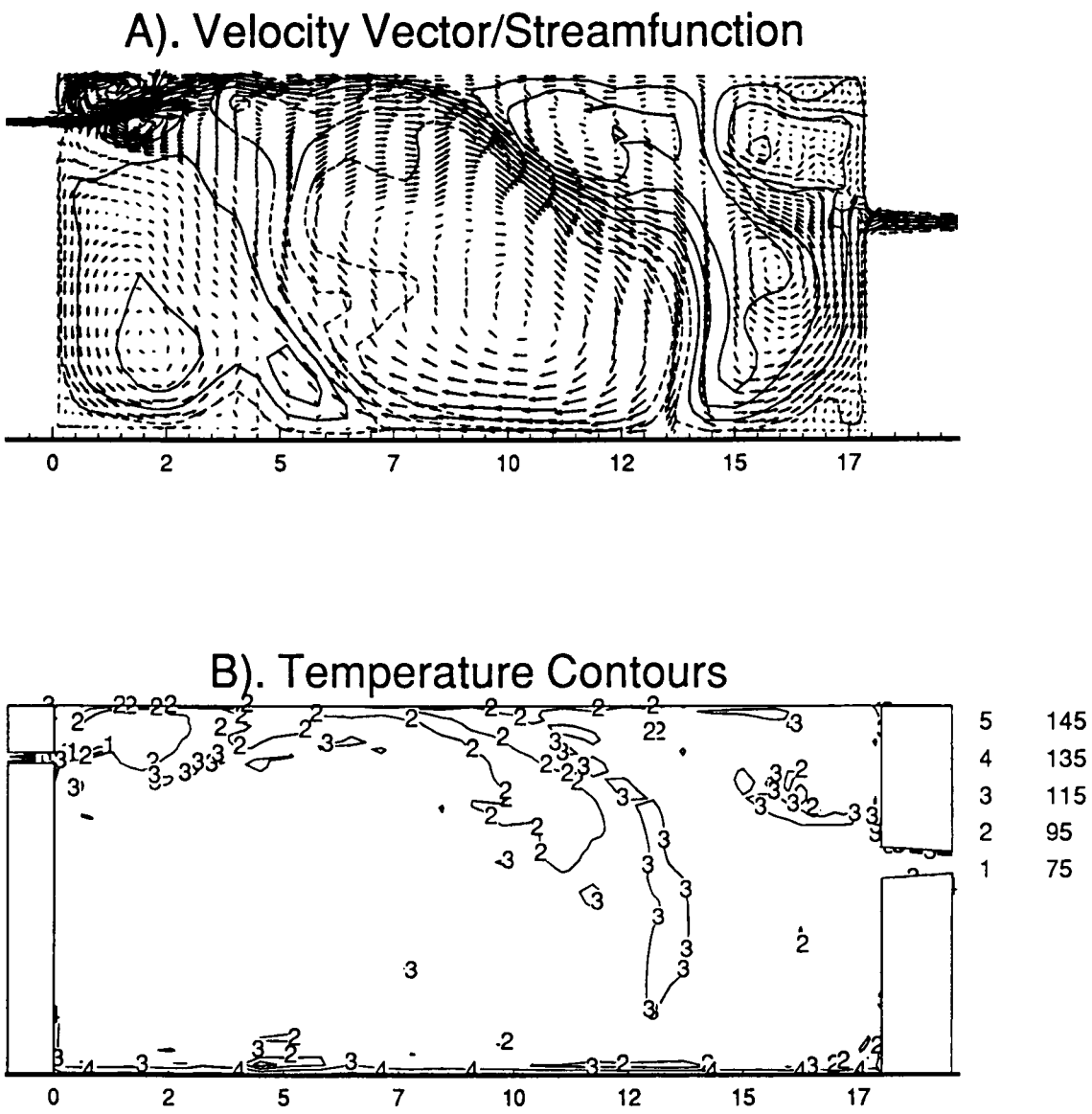
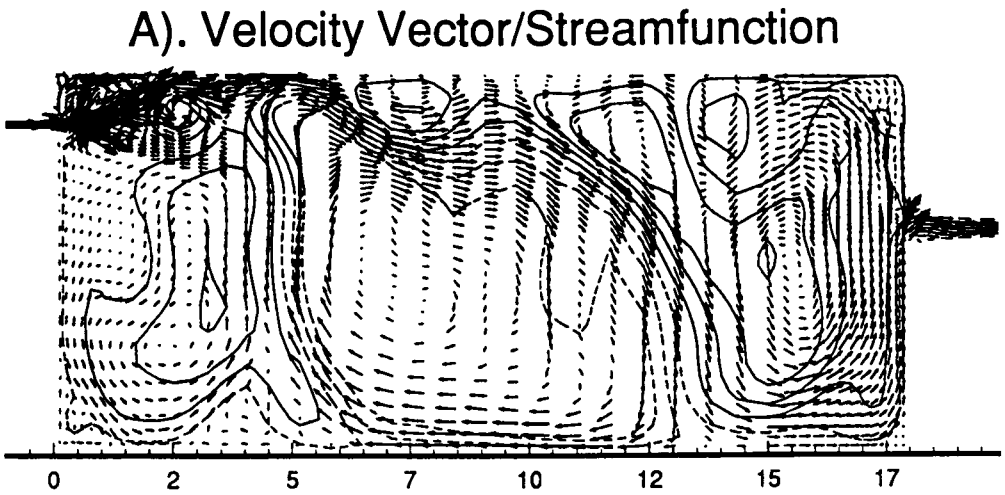


Figure 73
Non-isothermal Case (time = 23.9 sec.)



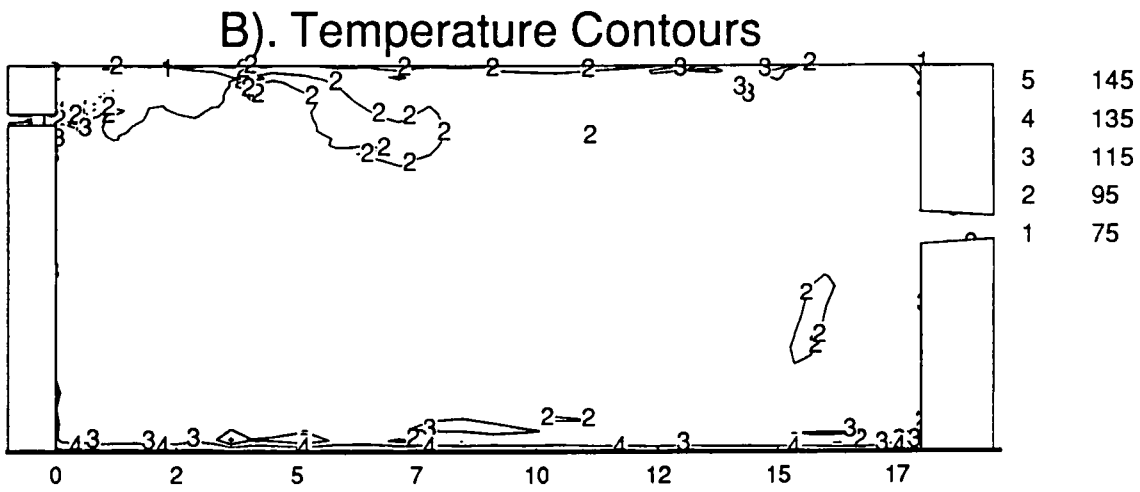
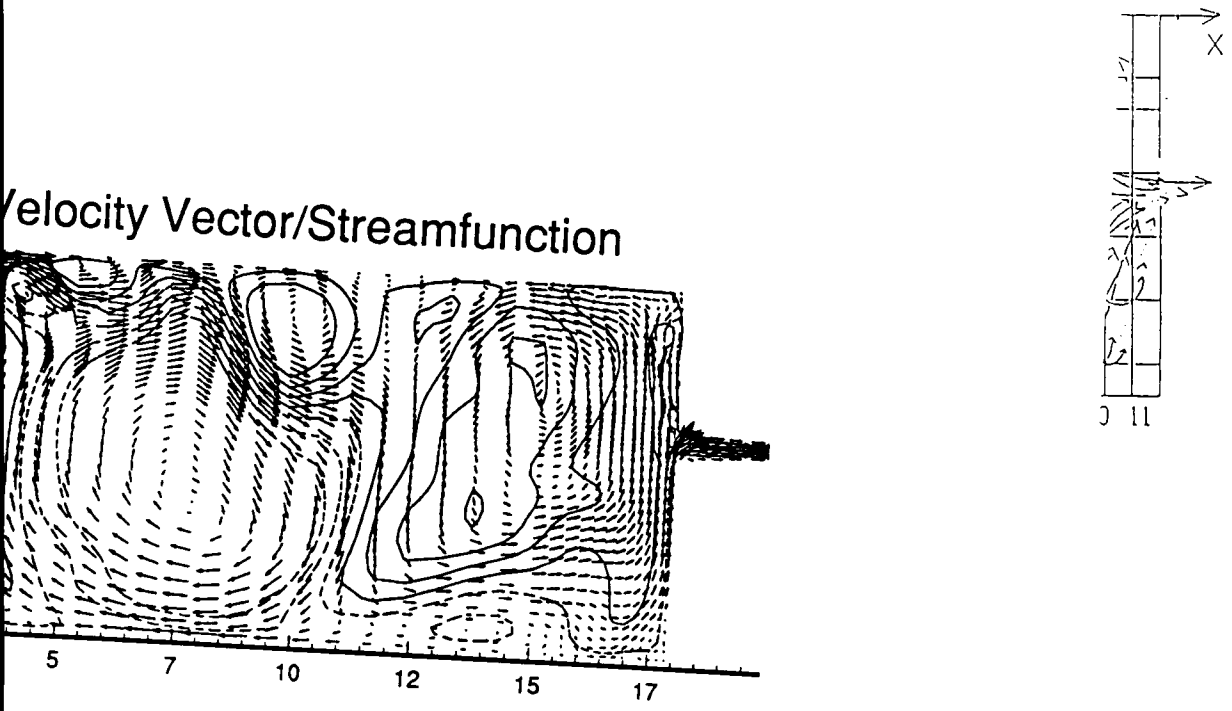
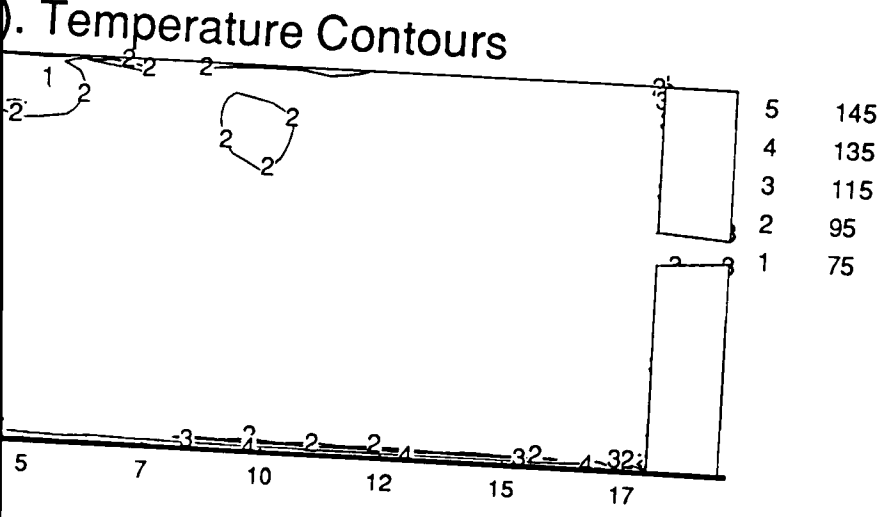


Figure 74
Non-isothermal Case (time = 27.1 sec.)





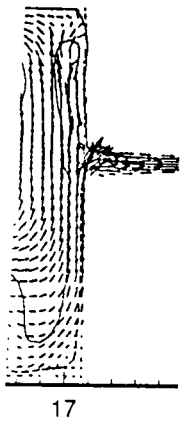


Figure 75
Non-isothermal Case (time = 31.6 sec.)

Chapter VI

Conclusions and Recommendations

The results presented in Chapter V stress the capabilities of the continuity constraint algorithm. The continuity constraint algorithm retains the primitive variable form of momentum in terms of the velocity vector field. The advantages of retaining the primitive variable form is the application of a Reynolds-averaged turbulence closure model which are typically expressed in terms of mean-velocity gradients. In addition, the kinematic flux vector jacobians in the artificial viscosity terms utilize the primitive variable form of the momentum equation.

The thermal cavity results showed reduced mesh scale oscillations for $Ra=10^6$ on the coarse 11x11 mesh when compared with the vorticity-streamfunction results. Local mesh refinement of the 11x11 mesh reduced the oscillations near the corners of the domain, but sacrificed detail toward the center of the cavity. The addition of minor artificial viscosity reduced the mesh-scale oscillations to near negligible without adversely effecting the solution. The uniform mesh refinement from 11x11 to 21x21 showed not only improvement in the solution quality by eliminating mesh-scale oscillations, but provide needed detail for interpreting the results.

The step-wall diffuser problem showed excellent agreement at Re=400 with the experimental results of Armaly for a two-dimensional flow problem. The agreements were not as satisfactory with the results above Re=420, which is three dimensional flow. Two dimensional simulations lack any cross-flow effects which perturb the flow field apparent in three-dimensional flow. Therefore, direct comparison between the results is inconclusive. The cross-flow effects for a three-dimensional step-wall diffuser simulations are addressed by Paul Williams in his dissertation work [13]. In addition, the coarse axial mesh resulted in inaccuracy in locating the points of reattachment and detachment identified by the zero vorticity contour.

The heat transfer benchmark problem demonstrated excellent agreement in the flow field variables with Gartling's results on a more refined mesh, even though simulations are carried out with the vorticity-

streamfunction formulation. The corresponding temperature profile generated Nusselt number calculations that compared remarkably well with the expected solution of Karac [19].

The room air motion simulations display the complex nature of the solution. The continuity constraint solution showed the flow to be unsteady as indicated by the continually evolving flow field and the longitudinal oscillations in the supply jet, with the non-isothermal case producing a more random behavior. Direct comparison with Zhang's visualized flow patterns are inconclusive due to the sparse location of the smoke releases and the transient nature of the flow. Instantaneous values at select times of the measured data would be more suitable for comparison with simulation results.

The use of physical damping in the exhaust duct was successful in eliminating the recirculation bubble forming at the outflow boundary without apparent perturbation of the flow in the room exit region. Zhang's report omits data at the exhaust plane making it difficult to determine an appropriate outflow boundary condition, but the simulation results show that a vanishing derivative for velocity at the room exit plane is inappropriate for these simulations requiring the use of an exhaust duct.

The continuation of the room air motion simulations with the continuity constraint algorithm should first involve continuing the simulations to determine if a periodic pattern in the flow field develops. If a periodic pattern is identified, the damping in the exhaust duct should be reduced to determine the effect on the flow in the room itself. A simple order of magnitude reduction in Re^t in the exhaust would determine the effects on the flow field. If reduction of the physical damping in the exhaust does perturb the flow field within the room, the Re^t should be decreased until the recirculation cell forming at the exhaust plane adversely effects numerical stability.

A mesh refinement study is needed on the simulations to determine if a mesh independent solution can be obtained with the continuity constraint algorithm. The mesh refinement would simply involve increasing the mesh density without any localized refinement in a region of the domain. In addition to the mesh refinement study, the dissipation provided by Re^t should be reduced until numerical instability develops The level of Re^t that numerical instability occurs will depend on the mesh refinement

Finally, identification of a turbulence closure model would be informative to determine the effects on the mean velocity field. The experimental results indicate localized low level turbulence, but the absence of turbulent dissipation in locations of the room missing in the simulations may have an effect on the flow field.

LIST OF REFERENCES

1. Rodi, W.. "Turbulence Models and their Applications in Hydraulics", Monogram for Int. Assn. for Hydraulic Research, Delft, 1980.
2. Gresho, P. M. "Some Interesting Issues in Incompressible Fluid Dynamics, Both in the Continuum and in Numerical Simulation", Preprint for Advances in Applied Mechanics, August, 1990.
3. White, F. M. *Viscous Fluid Flow*, McGraw-Hill Book Co., New York (1974).
4. Gresho, P. M., and Sani, R. L., " On Pressure Boundary Conditions for the Incompressible Navier-Stokes Equations", *Int. J. Numer. Fluids*, Vol. 7, pp 1111-1145 (1987).
5. Baker, A. J. ,*Finite Element Computational Fluid Mechanics*, Hemisphere, Washington D.C. (1983).
6. Noronha, W. P., and Baker, A. J.," A Taylor Weak Statement Finite Element CFD Algorithm for 2D Incompressible Navier-Stokes Equations", AIAA Paper 89-0659 (1989).
7. Baker, A. J., and Pepper, D. W. *Finite Element 1-2-3*, McGraw-Hill Book Co., New York (1991).
8. Raymond, W. H., and Gardner, A. "Selective Damping in a Galerkin Method for Solving Wave Problems with Variable Grids", *Mon. Weather Review*, Vol. 104, pp. 1583-1570 (1976).
9. Gresho, P. M., Sani, R. L., and Taylor, C. "Announcement-Open Boundary Condition (OBC) Minisymposium", *Int. J. Numer. Fluids*, Vol. 11, pp. 951-952 (1990).
10. Armaly, B. F., Durst, F., Pereira, J. C., and Schonung, B. "Experimental and Theoretical Investigation of Backward-facing Step Flow", *J. Fluid Mech.*, Vol. 127, pp. 473-496 (1983).
11. Gartling, D. K. "A Test Problem for Outflow Boundary Conditions - Flow Over a Backward-facing Step", *Int. J. Numer. Fluids*, Vol. 11, pp. 953-967 (1990).
12. Leone, J. M. "Open Boundary Condition Symposium Benchmark Solution: Stratified Flow Over a Backward-facing Step", Preprint for *Int. J. Numer. Fluids*, May 1990.
13. Williams, P.T. "A 3-D Time-Accurate Incompressible Navier-Stokes Finite Element CFD Algorithm", Ph.D. Dissertation, University of Tennessee, Knoxville, May, 1993.
14. Noronha, W.P. "On Taylor Weak Statement Finite Element Algorithm for 2-D Incompressible Navier-Stokes Equations", Ph.D Dissertation, University of Tennessee, Knoxville, Dec., 1993.

15. Zhang, J.S., Christianson, L.L., Wu, G.J., and Riskowski, G.L.. "Detailed Experimental Measurements of Room Air Distribution for Evaluating Numerical Simulation Models", Draft report for ASHRAE Conference, 1990

16. De Vahl Davis, G. "Natural Convection of Air in a Square Cavity: A Benchmark Numerical Solution", *Int. J. Numer. Fluids*, Vol. 3, pp. 249-264, (1990).

17. Bejan, A., "Convection Heat Transfer", John Wiley & Sons., New York (1983)

18. Kakac, S., Shah, R.K., and Aung, W. "Handbook of Single-Phase Convective Heat Transfer", John Wiley & Sons, New York (1987).

19. Li, Yuguo, "Simulation of Flow and Heat Transfer in Ventilated Rooms", Transactions of the Department of Mechanics/Applied Computational Fluid Dynamics, Royal Institute of Technology, ISSN 0281-7721, Stockholm, Sweden (Aug., 1992).

APPENDICES

Appendix I

Finite Element Matrix Form of the Weak Statement

General conservation law statement

The general form of the conservation law weak statement without added artificial dissipation is

$$WS(q^N) = \int_\Omega \Psi_i \left(\frac{\partial q^N}{\partial t} + A_j \frac{\partial q^N}{\partial x_j} \right) d\Omega + \int_\Omega \frac{\partial \Psi_i}{\partial x_j} (f_j^v)^N \, d\Omega - \oint_{\partial\Omega} \Psi_i \, (f_j^v)^N \, n_j \, d\Omega = 0 \tag{1}$$

where the kinematic flux vector has been replaced by the equivalent Jacobian expression for clarity. For a bilinear basis and using element average metric data, the matrix form of the weak statement for the momentum equation is

$$\begin{aligned} WS(\{UI\}_e) = S_e \Big(& DET_e [B200] \{UI\}_e' + ETAJK_e \{UJ\}_e^T [B300K] \{UI\}_e \\ & ETAIK_e [B20K] \{P\}_e + \frac{1}{Re^f} \frac{ETAJK_e ETAJM_e}{DET_e} [B2KM] \{UI\}_e \\ & - ArDET_e [B200] \{\Theta\}_e - \frac{1}{Re^f} [A201L] \{UI\}_e \{NJ\}_e \Big) = \{0\} \end{aligned} \tag{2}$$

where [B300K] is a hyper-matrix (Baker[1;p.486]) resulting from interpolation of the non-linear convective velocity term. The indices "I,J,K,M" range from $1 \le (*) \le 2$.

The matrix statement for the energy equation is

$$\begin{aligned} WS(\{\Theta\}_e) = S_e \Big(& DET_e [B200] \{\Theta\}_e' + ETAJK_e \{UJ\}_e^T [B300K] \{\Theta\}_e \\ & + \frac{1}{Pe^f} \frac{ETAJK_e ETAJM_e}{DET_e} [B2KM] \{\Theta\}_e - DET_e [B200] \{SORC\}_e \\ & - \frac{1}{Pe^f} [A201L] \{\Theta\}_e \{NJ\}_e \Big) = \{0\} \end{aligned} \tag{3}$$

The vorticity weak statement is a modification since the convective transport velocity is replaced with the streamfunction

$$\mathrm{ETAJK_e}\{UJ\}_e{}^T\left\{N_1^+\right\}\left\{N_1^+\right\}\frac{\partial\left\{N_1^+\right\}^T\{\Omega\}_e}{\partial\eta_k}$$

$$=\mathrm{ETANM_e ETAJK_e}\{\Psi\}_e{}^T\frac{\partial\left\{N_1^+\right\}}{\partial\eta_m}\left\{N_1^+\right\}\left\{N_1^+\right\}\frac{\partial\left\{N_1^+\right\}^T\{\Omega\}_e}{\partial\eta_k}\varepsilon_{jn}$$

$$=\frac{\mathrm{ETALNM_e ETAJK_e}}{\mathrm{DET_e^2}}\{\Psi\}_e{}^T[B3M0K]\{\Omega\}_e\varepsilon_{jn} \tag{4}$$

where ε_{jn} is the permutation symbol

j	n	value
1	1	0
1	2	1
2	1	-1
2	2	0

The matrix form of the vorticity transport equation then becomes

$$\mathrm{WS}\left(\{\Omega\}_e\right)=\mathrm{S_e}\Big(\mathrm{DET_e}[B200B]\{\Omega\}_e{}' +\frac{\mathrm{ETANM_e ETAJK_e}}{\mathrm{DET_e}}\{\Psi\}_e{}^T[B3M0KB]\{\Omega\}\varepsilon_{jn_e}$$

$$+\frac{1}{\mathrm{Re^f}}\frac{\mathrm{ETAJK_e ETAJM_e}}{\mathrm{det_e}}[B2KMB]\{\Omega\}_e+\mathrm{ArETA1K}[B20KB]\{\Theta\}_e$$

$$-\frac{1}{\mathrm{Re^f}}[A201L]\{\Omega\}_e\{NJ\}_e\Big)=\{0\} \tag{5}$$

For the thermal transport equation, the same modification to the convective velocity is made.

Poisson equations

The matrix form of the weak statement for the Poisson equation of the harmonic constraint is

$$\mathrm{WS}(\{\Phi\})=\mathrm{S_e}\Big(\frac{\mathrm{ETAIK_e ETAIM_e}}{\mathrm{DET_e}}[B2KM]\{\Phi\}_e-\mathrm{ETAIK_e}[B20K]\{UI\}_e$$

$$-[A201L]\{\Phi\}_e\{NI\}_e\Big)=\{0\} \tag{6}$$

Similarly, for the Poisson compatibility equation for the stream function

$$WS\left(\{\Psi\}_e\right) = S_e\left(\frac{ETAIK_e ETAIM_e}{DET_e}[B2KM]\{\Psi\}_e - det_e[B200]\{\Omega\}_e - [A201L]\{\Psi\}_e\{NI\}_e\right) = \{0\} \tag{7}$$

Artificial dissipation

The $\bar{\beta}$ term provides numerical dissipation for insufficient mesh discretization by increasing accuracy of the Taylor series approximation for the time derivative. The finite element form for the general expression using the element level Courant number is

$$\frac{\bar{\beta}\Delta t}{2}\frac{\partial}{\partial x_j}\left(A_j A_k \frac{\partial q}{\partial x_k}\right)_e \cong$$

$$\frac{\nu_q}{2UNORM_e}\frac{ETAJM_e ETAKL_e}{\sqrt{DET_e}}\int_{\Omega_e}\frac{\partial\left\{N_1^+\right\}}{\partial\eta_m}\left(\left\{N_1^+\right\}^T\{AJ\}_e\left\{N_1^+\right\}^T\{AK\}_e\frac{\partial\left\{N_1^+\right\}^T}{\partial\eta_l}\right)d\eta_1 d\eta_2\{Q\}_e \tag{8}$$

where $UNORM_e$ is the element average velocity magnitude

$$\left|(u_j)_e\right| \cong \sqrt{\{UJ\}_e^T\left\{N_1^+\right\}\left\{N_1^+\right\}^T\{UJ\}_e} = \sqrt{\{UJ\}_e^T[B200B]\{UJ\}_e} = UNORM_e \tag{9}$$

Equation (10) requires the evaluation of the kinematic flux vector Jacobian products. For the state variables, the Jacobian expressions are

$$A_j A_k \frac{\partial q}{\partial x_k} = \begin{Bmatrix} u_j u_k \dfrac{\partial u_i}{\partial x_k} + u_i u_k \dfrac{\partial u_j}{\partial x_k} \\ u_j u_k \dfrac{\partial \Theta}{\partial x_k} \\ u_j u_k \dfrac{\partial \omega}{\partial x_k} \end{Bmatrix} \tag{10}$$

The finite element form of the numerical dissipation term for momentum is

$$\frac{\nu_q}{2UNORM_e}\frac{ETAJM_e ETAKL_e}{\sqrt{DET_e}}\left(\int_{\Omega_e}\frac{\partial\left\{N_I^+\right\}}{\partial\eta_m}\left(\left\{N_I^+\right\}^T\{UJ\}_e\left\{N_I^+\right\}^T\{UK\}_e\frac{\partial\left\{N_I^+\right\}^T}{\partial\eta_l}\right)d\eta_1 d\eta_2\{UI\}_e\right.$$

$$\left.\int_{\Omega_e}\frac{\partial\left\{N_I^+\right\}}{\partial\eta_m}\left(\left\{N_I^+\right\}^T\{UI\}_e\left\{N_I^+\right\}^T\{UK\}_e\frac{\partial\left\{N_I^+\right\}^T}{\partial\eta_l}\right)d\eta_1 d\eta_2\{UJ\}_e\right) \tag{11}$$

Transposing the UK velocity component, the matrix form is

$$\frac{\nu_q}{2UNORM_e}\frac{ETAJM_e ETAKL_e}{\sqrt{DET_e}}\left([B2M0]\{UJ\}_e\{UK\}_e^T[B20L]\{UI\}_e\right.$$

$$\left.+[B2M0]\{UI\}_e\{UK\}_e^T[B20L]\{UJ\}_e\right) \tag{12}$$

A simplification can be made by expressing the Jacobian velocity components as element average values taking them outside the integral. The matrix statement reduces to

$$\frac{\nu_q}{2UNORM_e}\frac{ETAJM_e ETAKL_e}{\sqrt{DET_e}}\left((UJ,UK)_e[B2ML]\{UI\}_e+(UI,UK)_e[B2ML]\{UJ\}_e\right) \tag{13}$$

A similar evaluation is performed for the scalar quantities ω and Θ

$$\frac{\nu_q}{2UNORM_e}\frac{ETAJM_e ETAKL_e}{\sqrt{DET_e}}[B2M0]\{UJ\}_e\{UK\}_e^T[B20L]\{QS\}_e \tag{14}$$

where QS denotes a scalar variable. Defining the Jacobian velocity components as element averaged values, the final matrix form is

$$\frac{\nu_q}{2UNORM_e}\frac{ETAJM_e ETAKL_e}{\sqrt{DET_e}}(UJ,UK)_e[B2ML]\{QS\}_e \tag{15}$$

1. Baker, A. J. ,*Finite Element Computational Fluid Mechanics*, Hemisphere, Washington D.C. (1983).

Appendix II

Evaluation of Newton Jacobian Matrices

Momentum Equation

Beginning the evaluation of the Newton Jacobian expressions $\left([JRQ]=\frac{\partial R^{n+1}}{\partial Q^{n+1}}\right)$ with the matrix form of the residual for the momentum equation

$$\begin{aligned}\left(\{R(UI)\}\right) &= ETAJK_e\{UJ\}_e^T[B300KB]\{UI\}_e + ETAIK_e[B20KB]\{P\}_e \\ &+\frac{1}{Re^f}\frac{ETAJK_e ETAJM_e}{det_e}[B2KMB]\{UI\}_e - Ardet_e[B200B]\{\Theta\}_e\delta_{ig} \\ &-\frac{1}{Re^f}[A201L]\{UI\}_e\{NJ\}_e\end{aligned} \tag{1}$$

the Jacobian expressions are

$$[JUU]=\frac{\partial\{R(U)\}}{\partial\{U\}}=ETAJK_e\{UJ\}_e^T[B300KB]+ETA1K_e\{U\}_e^T[B300KB]$$
$$+\frac{1}{Re^f}\frac{ETAJK_e ETAJM_e}{det_e}[B2KMB]-\frac{1}{Re^f}[A201L]\{NJ\}_e$$

$$[JUV]=\frac{\partial\{R(U)\}}{\partial\{V\}}=ETA2K_e\{U\}_e^T[B300KB]$$

$$[JU\Theta\}=\frac{\partial\{R(U)\}}{\partial\{\Theta\}}=0$$

$$[JVU]=\frac{\partial\{R(V)\}}{\partial\{U\}}=ETA1K_e\{V\}_e^T[B300KB]$$

$$[JVV]=\frac{\partial\{R(V)\}}{\partial\{V\}}=ETAJK_e\{UJ\}_e^T[B300KB]+ETA2K_e\{V\}_e^T[B300KB]$$
$$+\frac{1}{Re^f}\frac{ETAJK_eETAJM_e}{det_e}[B2KMB]-\frac{1}{Re^f}[A201L]\{NJ\}_e$$

$$[JV\Theta]=\frac{\partial\{R(V)\}}{\partial\{\Theta\}}=-Ardet_e[B200B] \tag{2}$$

The residual for the transport of thermal energy

$$\{R(\Theta)\}=ETAJK_e\{UJ\}_e^T[B300KB]\{\Theta\}_e+\frac{1}{Pe^f}\frac{ETAJK_eETAJM_e}{det_e}[B2KMB]\{\Theta\}_e$$
$$-det_e[B200B]\{SORC\}_e-\frac{1}{Pe^f}[A201L]\{\Theta\}_e\{NJ\}_e \tag{3}$$

gives the Jacobian expressions

$$[J\Theta U]=ETA1K_e\{\Theta\}_e^T[B300KB]$$

$$[J\Theta V]=ETA2K_e\{\Theta\}_e^T[B300KB]$$

$$[J\Theta\Theta]=ETAJK_e\{UJ\}_e^T[B300KB]+\frac{1}{Pe^f}\frac{ETAJK_eETAJM_e}{det_e}[B2KMB]$$
$$-det_e[B200B]\frac{\partial\{SORC\}_e}{\partial\{\Theta\}}-\frac{1}{Pe^f}[A201L]\{NJ\}_e \tag{4}$$

The Newton iteration algorithm for the primitive variable form of the Navier-Stokes equation system coupled with temperature is

$$\left[[M]+\theta\Delta t\begin{bmatrix}JUU & JUV & 0\\ JVU & JVV & JV\Theta\\ J\Theta U & J\Theta V & J\Theta\Theta\end{bmatrix}\right]\begin{Bmatrix}\delta U\\ \delta V\\ \delta\Theta\end{Bmatrix}_{p+1}^{n+1}=-\begin{Bmatrix}\{R(U)\}\\ \{R(V)\}\\ \{R(\Theta)\}\end{Bmatrix}_p^{n+1} \tag{5}$$

Vorticity-Stream Function Formulation

From Appendix I, the residual of the vorticity transport equation is

$$\{R(\Omega)\} = \frac{ETALM_e ETAJK_e}{det_e}\{\Psi\}_e^T [B3M0KB]\{\Omega\}\varepsilon_{jl_e}$$
$$+\frac{1}{Re^f}\frac{ETAJK_e ETAJM_e}{det_e}[B2KMB]\{\Omega\}_e + ArETA1K[B20KB]\{\Theta\}_e$$
$$-\frac{1}{Re^f}[A201L]\{\Omega\}_e\{NJ\}_e \qquad (6)$$

From this, the Jacobian expressions are directly determined

$$[J\Omega\Omega] = ETALM_e ETAJK_e\{\Psi\}_e^T [B3M0KB]\varepsilon_{jl_e}$$
$$+\frac{1}{Re^f}\frac{ETAJK_e ETAJM_e}{det_e}[B2KMB] + -\frac{1}{Re^f}[A201L]\{NJ\}_e$$

$$[J\Omega\Psi] = \frac{ETALM_e ETAJK_e}{det_e}\{\Omega\}_e^T [B3K0MB]\varepsilon_{jl_e}$$

$$[J\Omega\Theta] = ArETA1K[B20KB] \qquad (7)$$

The matrix form of the Poisson compatibility equation is

$$\{R(\Psi)\} = \frac{ETAIK_e ETAIM_e}{det_e}[B2KMB]\{\Psi\}_e - det_e[B200B]\{\Omega\}_e - [A201L]\{\Psi\}_e\{NI\}_e = \{0\} \qquad (8)$$

where the Jacobian terms are directly evaluated as

$$[J\Psi\Omega] = -det_e[B200B]\{\Omega\}_e$$

$$[J\Psi\Psi] = \frac{ETAIK_e ETAIM_e}{det_e}[B2KMB]\{\Psi\}_e - [A201L]\{NI\}_e \qquad (9)$$

The residual for the transport of thermal energy is identical to the vorticity transport except for the energy source contribution

$$\{R(\Theta)\} = \frac{ETALM_e ETAJK_e}{det_e}\{\Psi\}_e^T[B3M0KB]\{\Theta\}\varepsilon_{jl_e}$$
$$+\frac{1}{Pe^f}\frac{ETAJK_e ETAJM_e}{det_e}[B2KMB]\{\Theta\}_e - det_e[B200B]\{SORC\}_e$$
$$-\frac{1}{Pe^f}[A201L]\{\Theta\}_e\{NJ\}_e \qquad (10)$$

From the residual, the Jacobian contributions for temperature are

$$[J\Theta\Omega] = 0$$

$$[J\Theta\Psi] = \frac{ETALM_e ETAJK_e}{det_e}\{\Theta\}_e^T[B3M0KB]\varepsilon_{jl_e}$$

$$[J\Theta\Theta] = \frac{ETALM_e ETAJK_e}{det_e}\{\Psi\}_e^T[B3M0KB]\varepsilon_{jl_e} + \frac{1}{Pe^f}\frac{ETAJK_e ETAJM_e}{det_e}[B2KMB]$$
$$- det_e[B200B]\frac{\partial\{SORC\}}{\partial\{\Theta\}} - \frac{1}{Pe^f}[A201L]\{NJ\}_e \qquad (10)$$

The fully coupled Newton iteration algorithm for the vorticity-stream function formulation is

$$\left[[M] + \theta\Delta t\begin{bmatrix} J\Omega\Omega & J\Omega\Psi & J\Omega\Theta \\ J\Psi\Omega & J\Psi\Psi & 0 \\ 0 & J\Theta\Psi & J\Theta\Theta \end{bmatrix}\right]\begin{Bmatrix}\delta\Omega \\ \delta\Psi \\ \delta\Theta\end{Bmatrix}_{p+1}^{n+1} = -\begin{Bmatrix}\{R(\Omega)\} \\ \{R(\Psi)\} \\ \{R(\Theta)\}\end{Bmatrix}_p^{n+1} \qquad (12)$$

Appendix III

Time Integration Procedure

The parameter that determines an efficient time integration procedure is the maximum allowable time step determination. For steady state problems, the rate of convergence determines the number of time steps and iterations per time step the procedure requires to obtain a steady-state solution, where steady-state solution is expressed as the limit $\Delta t \to \infty$. The convergence theory of the Newton iteration procedure for linear system such as the vorticity-stream function is well defined [Baker; p.175], but the efficient utilization requires computational experimentation. The convergence theory for a non-linear system that is present in primitive variable formulations is not well developed, and the most effective method for determining the convergence is developed from experimentation. The procedure for the vorticity-stream function algorithm will be given first for back ground into the procedure to the continuity constraint algorithm. For clarity, the Newton algorithm of equation (60) is presented again

$$\left[M + \theta\Delta t[J]^{n+1}\right]\{\delta Q\}_{p+1}^{n+1} = -\{FQ\}_{p}^{n+1}; [J]^{n+1} = \frac{\partial\{R\}^{n+1}}{\partial\{Q\}^{n+1}} \tag{1}$$

along with the variable update

$$\{Q\}_{p+1}^{n+1} = \{Q\}^{n} + \sum_{i=0}^{p}\{\delta Q\}_{i+1}^{n+1} \tag{2}$$

Vorticity-stream function algorithm

The Newton iteration algorithm will approximate quadratic convergence, hence minimum iterations at each time step, as long as the first interate δQ_1 is not too large at the initial iteration (p=0). In proceeding to a steady-state solution, the initial time step is chosen of the order 10^{-2} seconds, and thereafter incrementally increases as the solution progresses if convergence to a minimum δQ (DQMIN) is obtained within a reasonable number of iterations. DQMIN is typically specified on the order of 10^{-4}. The convergence to DQMIN usually occurs within three iterations as a result of the quadratic convergence. If DQMIN is not obtained within four iterations, the time step size is held constant. If more than four iterations are required, the time step size is decreased. More than three iterations required to obtain

DQMIN indicates initial δQ_1 is excessive and a diverging solution may be evident. Decreasing the time step size reduces the size of the initial δQ allowing the solution to converge. Typically, a limit is placed on the maximum number of iterations at each time step to eliminate unnecessary computations. As the solution progresses and the time step size increases, a limit on the time step size is set to prevent the initial δQ from growing excessively large. The maximum time step size is problem dependent, but a value in the range from 1 to 10 seconds is suitable. Eventually, DQMIN is obtained at the first iterate indicating steady state. Time integration is halted when δQ is a magnitude lower than DQMIN at the first iterate for Δt large enough.

Time accurate transient computations also require a flexible time step size, throughout the solution process, and DQMIN varies depending on the problem. Typically, DQMIN is several orders of magnitude higher than steady state computations allowing a larger δQ of the initial iterate. The same time step size control for steady state solutions is used for transient solutions. Eventually, a cycle should emerge between the time step size and iteration count indicating the pattern of the transient solution.

Continuity constraint algorithm

Since the continuity constraint algorithm retains the primitive variable form of the momentum equation, the convective term causes a non-linearity of the Newton statement requiring modifications to the iteration procedure. In addition, the pressure is replaced with the harmonic approximation

$$P^{n+1} \cong (P_A)_p^{n+1} + \frac{1}{\theta \Delta t} \phi_{p+1}^{n+1} \tag{3}$$

which perturbs the solution.

In practice, P_A is determined from the steady state solution of the pressure Poisson equation at a converged momentum solution from a preceding time step. At subsequent time steps, the ϕ solution is added to the pressure solution once within the time step. The perturbation in the solution process can arise from two sources; (1) inaccurate evaluation of the pressure Poisson equation, and (2) magnitude of the divergence error, which is a source term for the ϕ solution. The magnitude of the ϕ is measured in the energy semi-norm

$$\left\|\phi^N\right\|_E = \frac{1}{2}\mathrm{ETAIK}_e\mathrm{ETAIM}_e\sum_{e=1}^{M}\{\Phi\}_e^T[\mathrm{B2KMB}]\{\Phi\}_e \tag{3}$$

where M is the number of elements in the domain.

VITA

Edward (Ed) Gordon Schaub was born in Cheyenne, Wyoming on May 5, 1963. His parents are Edward Charles Schaub and Mary Margarent Schaub. Edward Gordon is an only child.

Ed received his bachelors degree in Chemical Engineer in December of 1987. He has worked as a co-op student for Pennzoil in Shreveport, Louisiana and the Savannah River Site under DuPont in Aiken, South Carolina. He worked on the Reactor Restart Project at the Savannah River Site before enrolling at the University of Tennessee in the Fall of 1989. He is currently seeking a Master's degree in Engineering Science with Computational Fluid Dynamics his area of study.

Ed is a member of Tau Beta Pi.